

**The effect of forest structure on yellow pine/mixed-conifer  
resilience to wildfire and bark beetle disturbance in the Sierra  
Nevada, California**

By

MICHAEL J. KOONTZ

DISSERTATION

Submitted in partial satisfaction of the requirements for the degree of

DOCTOR OF PHILOSOPHY

in

ECOLOGY

in the

OFFICE OF GRADUATE STUDIES

of the

UNIVERSITY OF CALIFORNIA

DAVIS

Approved:

---

(Andrew M. Latimer), Chair

---

(Malcolm P. North)

---

(Constance I. Millar)

Committee in Charge

2019

The effect of forest structure on yellow pine/mixed-conifer resilience to wildfire and  
bark beetle disturbance in the Sierra Nevada, California

Copyright © 2019

by

Michael J. Koontz

To my mom and dad.

## Acknowledgements

I want to start by acknowledging that all of this work took place on unceded territory of a number of Native American peoples including the Patwin, Ute, Nisenan, Washoe, Mono, Miwok, and Paiute. Their ongoing history is intimately tied to forest disturbances in the Sierra Nevada yellow pine/mixed-conifer and greatly contributes to what is considered the ‘natural range of variation’ for this system. Changes in disturbance regimes since Euroamerican invasion must therefore be considered within the context of settler colonialism, which dramatically shifted the Native American influence on these disturbance-prone landscapes. I am grateful for the opportunity to live and do science in these areas.

I am very grateful for the many people that supported me during my Ph.D. There’s a lot of overlap in the various ways that people have contributed to my experience in the Graduate Group in Ecology (GGE), which speaks to the diversity of talent represented by my colleagues.

The best thing I did during my PhD was to join a pair of exceptional labs. The collegiality and immense talent of the Latimer and North labs kept me excited to pursue awesome science. I’m grateful to the Latimer Lab members with whom I overlapped: Jens Stevens, Derek Young, Brian Smithers, Allie Weill, Marina LaForgia, and Paige Kouba. I’m also grateful to the North Lab members with whom I overlapped: Mason Earles, Brian Smithers, Gabina Bohlmann, Jens Stevens, Jan Ng, Max Odland, and Paige Kouba. Thanks also to the allied labs of the Latimer and North labs: the Safford Lab, the Jin Lab, the Gremer Lab, and the Young Lab.

Thank you to the administrative staff that helped me keep track of all the logistics associated with completing a PhD: Holly Hatfield Rogai, Elizabeth Sturdy, Matt Malepeai,

and Lisa Brown. I don't know how I would have kept up with the various deadlines, paperwork, funding sources, etc. without your help.

I acknowledge salary funding from the NSF GRFP, the Graduate Group in Ecology, and the Department of Plant Sciences. I also acknowledge the US Forest Service Western Wildlands Environmental Threat Assessment Center, who funded the drone research.

Thanks to Leif Mortenson for taking me on my first tour of western pine beetle attacked forests as well as Chris Fettig for guiding my thinking on how this disturbance affects Sierra Nevada forests. Thanks to Brandon Collins for early conversations about yellow pine/mixed-conifer fire regimes and measuring forest structural heterogeneity.

Thanks to the GLORIA Great Basin nonprofit for an amazing time in the mountains collecting important baseline data about alpine plant distributions. This is a long-term monitoring project and I hope to be volunteering with you all for the next 100 years.

Thanks to Dan Kroccheck, Alex Mandel, and Taylor Nelson for letting me bounce ideas off of you while I was building the drone project.

Thanks to all the people that are coauthors on manuscripts I led during my PhD: Chhaya Werner, Steve Fick, Zack Steel, Leif Mortenson, Chris Fettig, Ruth Hufbauer, Brett Melbourne, Meagan Oldfather, Malcolm North, and Andrew Latimer.

I learned a ton about teaching during my time at UC Davis in large part due to my participation with The Carpentries and the R-DAVIS class. I want to thank a series of folks that helped guide my learning about modern pedagogical approaches to teaching scientific computing skills including Noam Ross, Michael Levy, Myfanwy Johnston, Greg Wilson, Tracy Teal, Titus Brown, Emilio Laca, Ryan Peek, Taylor Reiter, Martha Wohlfeil, Michael Culshaw-Maurer, and Andrew Latimer. A special shoutout to Titus Brown for letting me co-run an R bootcamp during the Data Intensive Biology Summer

Institute and Ryan Peek for inviting me to go all-in with him on building a scientific computing course in the GGE based on a shared motivation to lower the barrier to entry for using computers to help folks do ecology.

Working with the Diversity Committee has been one of the greatest honors of my time in the GGE. Thank you to all of the amazing people on this committee that work hard to enact meaningful change that makes our ecology community more welcoming, inclusive, and equitable.

Thank you to my Guidance Committee and Qualifying Exam Committee members Rick Karban, Mark Schwartz, Connie Millar, Jenny Gremer, Robert Hijmans, and Sebastian Schreiber for helping to steer me on a good path from the get go.

I am incredibly grateful to my advisors Andrew Latimer, Malcolm North, and Connie Millar for granting me the confidence, safety net, and flexibility to try new ideas with very uncertain outcomes to see where they may lead. I think my dissertation benefitted greatly from my feeling that I could take a “high risk/high reward” approach to pursuing science; I felt comfortable operating on steep learning curves because I knew I had good spotters.

I thank my dog, Ouzel, for being a Very Good Pupper during my fieldwork and sometimes, but not always, alerting me when bears arrived in camp while we slept.

Finally, I want to thank my favorite ecologist, Meagan Oldfather, for inspiring me to be a better ecologist and person every day.

Michael J. Koontz  
June 2019  
ECOLOGY

## Abstract

Past and future disturbances are linked by their feedbacks with forest structure— the size, species, and spatial distribution of vegetation in a forest. Disturbances like wildfire and bark beetle activity can alter forest structure, which then influences the outcomes of future disturbances. The long-term persistence of forest ecosystems hinges on these feedbacks, which promotes resilience— the ability of a system to absorb disturbances and still retain its essential identity and functions. I explore these feedbacks by measuring disturbance severity as well as local-scale forest structure at broad spatial extents in the yellow pine/mixed-conifer forest system of the Sierra Nevada, California. I bring new tools, such as massively parallel cloud-based GIS and drone remote sensing, to bear on questions about how forest structure affects wildfire and bark beetle disturbance in this region. I introduce a new framework to describe how wildfire suppression biases burning conditions and thus observed fire effects in large fire events to be more extreme than would be expected if all ignitions were allowed to burn. With this selection bias of large fires in mind, I generate a new dataset of fire effects in the Sierra yellow pine/mixed-conifer system that captures outcomes from smaller fire events. I use this new fire effects dataset and also measure variability in horizontal forest structure using the computer vision approach of texture analysis for nearly 1000 fires that burned in the system between 1984 and 2017. I find that greater variability in forest structure reduces the probability of high severity wildfire, which increases forest resilience in this system ill-adapted to recover from large high-severity events. Finally, I use drone-captured imagery and structure from motion (SfM) techniques to recreate complex forest structure of over 9 km<sup>2</sup> of western

pine beetle-attacked forest along a 350 km latitudinal gradient and a 1000 m elevation gradient. I found that availability of the host tree for the western pine beetle, ponderosa pine, increases the probability of ponderosa pine mortality and average host size plays a different role depending on the climatic water deficit (a proxy for tree moisture stress) at each site: at cool wet sites, more small hosts drive mortality; at hot dry sites, more large hosts drive mortality. Overall, this work demonstrates how an understanding the complexities of local forest structure, including the size, species, and spatial distribution of trees, can generate new insights into how broader-scale patterns of tree mortality arise during wildfire and bark beetle disturbance.

# Contents

<b>Abstract</b>	vii
<b>List of Tables</b>	x
<b>List of Figures</b>	xi
<b>1 Local variability of vegetation structure increases forest resilience to wildfire</b>	1
Abstract . . . . .	2
Significance . . . . .	3
Introduction . . . . .	3
Results . . . . .	7
Discussion . . . . .	12
Material and Methods . . . . .	20
Acknowledgements . . . . .	31
<b>2 Differential response of a tree-killing bark beetle to host tree size across a gradient of climatic water deficit</b>	32
Abstract . . . . .	32
Introduction . . . . .	34
Methods . . . . .	38
Results . . . . .	62
Discussion . . . . .	67
Acknowledgements . . . . .	75

<b>Appendix: Supplemental Information for ‘Chapter 1: Remote sensing resistance’</b>	<b>76</b>
Supplemental methods . . . . .	76
Supplemental figures and tables . . . . .	78
<b>References</b>	<b>84</b>

# List of Tables

1.1	Comparison of four models described in Eq. 2 using different neighborhood sizes for calculating forest structural variability (standard deviation of NDVI within the neighborhood), neighborhood mean NDVI, and topographic roughness. LOO is a measure of a model's predictive accuracy (with lower values corresponding to more accurate prediction) and is calculated as -2 times the expected log pointwise predictive density (elpd) for a new dataset (Vehtari et al. 2017). $\Delta\text{LOO}$ is the difference between a model's LOO and the lowest LOO in a set of models (i.e., the model with the best predictive accuracy). The Bayesian $R^2$ is a 'data-based estimate of the proportion of variance explained for new data' (Gelman et al. 2018). Note that Bayesian $R^2$ values are conditional on the model so shouldn't be compared across models, though they can be informative about a single model at a time. . . . .	9
2.1	Reflectance sensitivity of the Micasense Rededge3 camera. The calibration panel value represents the reflectance of the calibration panel for the given wavelength. . . . .	41
2.2	Algorithm name, number of parameter sets tested for each algorithm, and references. . . . .	49
2.3	Site characteristics for each of the 32 sites. The site name consists of the forest name, elevation band, and rep separated by an underscore. The Eldorado National Forest is 'eldo', the Stanislaus National Forest is 'stan', the Sierra National Forest is 'sier', and the Sequoia National Forest is 'sequ'. The elevation band represents the lower bounds of the 305 meter (1000 foot) elevation bands in feet. Thus '3k' implies that site was located between 3,000 and 4,000 feet (914-1219 meters). Aerially detected mortality and density of the whole site is presented along with the mortality and density calculated from the ground data (aerial / ground). The density is measured in trees per hectare (tpha). . . . .	62

2.4	Correlation and differences between the best performing tree detection algorithm (lmaf with dist2d = 1 and ws = 2.5) and the ground data. An asterisk next to the correlation or RMSE indicates that this value was within 5% of the value of the best-performing algorithm/parameter set. Ground mean represents the mean value of the forest metric across the 110 ground plots that were visible from the sUAS-derived imagery. The median error is calculated as the median of the differences between the air and ground values for the 110 visible plots. Thus, a positive number indicates an overestimate by the sUAS workflow and a negative number indicates an underestimate. . . . .	65
2.5	Comparison of models used to validate and calibrate remotely sensed wildfire severity with ground-based composite burn index (CBI) severity sorted in descending order by the $R^2$ value from a 5-fold cross validation. A total of 56 models were tested representing all possible combinations of 7 different measures of wildfire severity (RBR, dNBR, dNBR2, RdNBR, RdNBR2, dNDVI, and RdNDVI), 4 different time windows in which Landsat imagery was acquired and summarized with a median reducer on a pixel-by-pixel basis (16 days, 32 days, 48 days, and 64 days), and two different interpolation methods (bilinear and bicubic). The three parameters ( $\beta_0$ , $\beta_1$ , and $\beta_2$ ) from the nonlinear model fit described in Eq. 1 are reported. For each model, the value of the remotely sensed wildfire severity measurement corresponding to the lower bounds of 3 commonly used categories of severity are reported ('low' corresponds to a CBI value of 0.1, 'mod' corresponds to a CBI value of 1.25, and 'high' corresponds to a CBI value of 2.25) . . . . .	79

# List of Figures

1.1	Three top performing remotely-sensed severity metrics based on 5-fold cross validation (relative burn ratio, 48-day window, bicubic interpolation; relative delta normalized burn ratio, 32-day window, bilinear interpolation; and relative delta normalized difference vegetation index, 48-day window, bilinear interpolation) calculated using new automated image collation algorithms, calibrated to 208 field measures of fire severity (composite burn index). See Supplemental Table 1 for performance of all tested models. . . . .	8
1.2	The main effects and 95% credible intervals of the covariates having the strongest relationships with the probability of high-severity fire. All depicted relationships derive from the model using the 90m x 90m neighborhood size window for neighborhood standard deviation of NDVI, neighborhood mean of NDVI, and topographic roughness, as this was the best performing model of the four neighborhood sizes tested. The effect sizes of these covariates were similar for each neighborhood size tested. . . . .	11

1.3	Geographic setting of the study. A) Location of yellow pine/mixed-conifer forests as designated by the Fire Return Interval Departure (FRID) product which, among other things, describes the potential vegetation in an area based on the pre-Euroamerican settlement fire regime. B) Locations of all fires covering greater than 4 hectares that burned in yellow pine/mixed-conifer forest between 1984 and 2017 in the Sierra Nevada mountain range of California according to the State of California Fire Resource and Assessment Program database, the most comprehensive database of fire perimeters of its kind. Colors indicate how many fire perimeters overlapped a given pixel within the study time period. C) (red) Locations of 208 composite burn index (CBI) ground plots used to calibrate the remotely sensed measures of severity. (black) Locations of random samples drawn from 972 unique fires depicted in panel B that were in yellow pine/mixed-conifer forest as depicted in panel A, and which were designated as “burned” by exceeding a threshold relative burn ratio (RBR) determined by calibrating the algorithm presented in this study with ground-based CBI measurements. . . . .	19
1.4	Example algorithm outputs for the Hamm Fire of 1987 (top half) and the American Fire of 2013 (bottom half) showing: prefire true color image (left third), postfire true color image (center third), relative burn ratio (RBR) calculation using a 48-day image collation window before the fire and one year later (right third). For visualization purposes, these algorithm outputs have been resampled to a resolution of 100m x 100m from their original resolution of 30m x 30m. Data used for analyses were sampled from the outputs at the original resolution. . . . .	24
1.5	Example of homogenous forest (top row) and heterogenous forest (bottom row) with the same mean NDVI values (~0.6). Each column represents forest structural variability measured using a different neighborhood size. . . . .	26
2.1	The network of field plots spanned a 350 km latitudinal gradient from the Eldorado National Forest in the north to the Sequoia National Forest in the south. Plots were stratified by three elevation bands in each forest, with the plots in the Sequoia National Forest (the southern-most National Forest) occupying elevation bands 305m above the three bands in the other National Forests in order to capture a similar community composition. . . . .	39
2.2	A dense point cloud representing ~40 hectares of forest is generated using Structure from Motion (SfM) processing of ~1900 images. The dense point cloud z- position represents the ground elevation plus the vegetation height. . . . .	44
2.3	The digital surface model (DSM) is a 2-dimensional representation of the dense point cloud generated using structure from motion (SfM) processing. The DSM represents the ground elevation plus the vegetation height. . . . .	45

2.4	The orthomosaic for each of the 32 sites is generated with the Structure from Motion (SfM) processing, showing a top-down view of the whole survey area such that distances between objects in the scene are preserved and can be measured. Depicted is an example orthomosaic for one of the 32 sites cropped to the extent of a single ground plot (5 ground plots per site) showing the orange X placed at exactly the plot center prior to flight. The original orthomosaic for the whole site represents an area approximately 1000 times as large as the area depicted here. . . . .	46
2.5	The digital terrain model (DTM) is generated by processing the dense point cloud using the cloth simulation filter algorithm (Zhang et al. 2016), which classifies points as ‘ground’ or ‘not-ground’ and then interpolates the ‘ground’ elevation using Delaunay triangulation for the rest of the dense point cloud footprint. The DTM represents the ground elevation without any vegetation. . . . .	47
2.6	The canopy height model (CHM) is generated by subtracting the digital terrain model from the digital surface model. The CHM represents the height of all of the elevation above ground level. . . . .	48
2.7	Tree locations are detected using the <code>1mfx</code> (Roussel et al. 2019) treetop detection algorithm on the dense point cloud. . . . .	52
2.8	Individual crowns are delineated using a marker controlled watershed segmentation algorithm (Meyer and Beucher 1990, Plowright 2018) on the canopy height model (CHM) using the detected tree locations as a priority map. If the algorithm failed to delineate a crown for a tree that was identified in the tree detection step, a circular crown with a 0.5m buffer centered on point location of the detected tree was added as a crown. . .	53
2.9	Each tree is classified as live or dead by extracting the pixel values from the 5 narrow bands of the Rededge3 camera (and 5 derived bands– see methods) in the orthomosaic within each segmented tree crown of the detected trees, taking their mean value, and using those means to predict live/dead status with a boosted logistic regression previously trained on a hand-classified set of segmented crowns from across the study area. . . .	55
2.10	For each live tree, we classified its species using the same means of extracted pixel values across the 5 Rededge3 narrow bands (and 5 derived bands) as predictors in a regularized discriminant analysis previously trained on a hand-classified set of segmented crowns from across the study area. . . . .	56
2.11	We rasterized the individual tree data by aggregating values to 20m x 20m cells. This example shows the proportion of dead trees per cell for the same example site as in the previous figures. . . . .	58

2.12 Posterior distributions of effect size from zero-inflated binomial model predicting the probability of ponderosa pine mortality in a 20m x 20m cell given forest structure characteristics of host trees and all trees within the cell, as well as a site-level climatic water deficit. The gray density distribution for each model covariate represents the density of the posterior distribution, the point underneath each density curve represents the median of the estimate, the bold interval surrounding the point estimate represents the 66% credible interval, and the thin interval surrounding the point estimate represents the 95% credible interval. . . . .	66
2.13 Line version of model results with 95% credible intervals showing primary influence of ponderosa pine structure on the probability of ponderosa pine mortality, and the interaction across climatic water deficit. The ‘larger trees’ line represents the quadratic mean diameter of ponderosa pine 0.7 standard deviations above the mean, and the ‘smaller trees’ line represents the quadratic mean diameter of ponderosa pine 0.7 standard deviations below the mean. . . . .	68
2.14 Schematic for how Landsat imagery was assembled in order to make comparisons between pre- and post-fire conditions. This schematic depicts a 64-day window of image collation prior to the fire which comprise the pre-fire image collection. A similar, 64-day window collection of imagery is assembled one year after the pre-fire image collection. . . . .	82
2.15 Conceptual diagram of ‘decoupling’ that sometimes occurs between the central pixel NDVI and the neighborhood mean NDVI. In each of these scenarios, our model results suggest that the probability that the central pixel burns at high severity is higher than expected given the additive effect of the covariates. The left panel depicts the “hole in the forest” decoupling, which occurs more frequently, and the right panel depicts the “isolated patch” decoupling. . . . .	83

# Chapter 1

## Local variability of vegetation structure increases forest resilience to wildfire

Michael J. Koontz<sup>1,2,\*</sup>, Malcolm P. North<sup>2,3</sup>, Chhaya M. Werner<sup>2,4</sup>, Stephen E. Fick<sup>5,6</sup>,  
Andrew M. Latimer<sup>2</sup>

<sup>1</sup>Graduate Group in Ecology, University of California; Davis, CA

<sup>2</sup>Department of Plant Sciences, University of California; Davis, CA

<sup>3</sup>Pacific Southwest Research Station, U.S.D.A. Forest Service; Mammoth Lakes, CA

<sup>4</sup>Center for Population Biology, University of California; Davis, CA

<sup>5</sup>U.S. Geological Survey, Southwest Biological Science Center

<sup>6</sup>Department of Ecology and Evolutionary Biology, University of Colorado; Boulder, CO

## **Abstract**

The long-term persistence of forest ecosystems hinges on their resilience to ongoing disturbance. Quantification of resilience in these valuable ecosystems remains difficult due to their vast extent and the longevity of forest species. Resilience to wildfire may arise from feedback between fire behavior and vegetation structure, which dictates fuel loading and continuity. Regular fire generates structural variability which may then enable forests to withstand future fires and retain their fundamental properties and functions—a hallmark of a resilient system. A century of fire suppression in the western United States has homogenized the structure of many forests, potentially upsetting these feedbacks and compromising forest resilience. We investigate the generality and scale of the effect of structural variability on wildfire behavior in yellow pine/mixed-conifer forest of California’s Sierra Nevada using cloud computing and texture analysis of a 33-year time series of satellite imagery. We measure wildfire response to forest structure for an unprecedented number and size range of wildfires, ensuring representation of both typical and extreme fire behavior, and find that greater structural variability is strongly associated with a lower probability of fire-induced overstory tree mortality. This resistance to wildfire was most apparent at the smallest spatial extent of forest structure tested (90m x 90m). Local-scale structural variability thus links past and future fire behavior, and makes forests more resilient to wildfire disturbance. Management strategies that increase vegetation structural variability, such as allowing fires to burn under moderate fuel and weather conditions, may therefore increase the probability of long-term forest persistence.

## *SIGNIFICANCE*

# Significance

A “resilient” forest endures disturbance and is likely to persist. Resilience to wildfire may derive from variability in vegetation structure, which interrupts fuel continuity and prevents fire from killing overstory trees. Testing the generality and scale of this phenomenon is challenging because forests are vast, long-lived ecosystems. We develop a novel cloud computing approach to consistently quantify forest structural variability and fire severity across >30 years and nearly 1,000 wildfires in California’s Sierra Nevada. We find that greater small-scale structural variability increases resilience by reducing rates of fire-induced tree mortality. Resilience of these forests is likely compromised by structural homogenization from a century of fire suppression, but may be restored with management that increases structural variability of vegetation.

# Introduction

Biological systems comprising heterogeneous elements can retain their fundamental properties in the face of regular disturbance. This ability of a heterogeneous system to absorb disturbances, reorganize, and to persist within a domain of stability with respect to its identity, structure, function, and feedbacks is termed resilience (Holling 1973, Walker et al. 2004). Resilience has been demonstrated in complex biological systems characterized by a variety of different types of “heterogeneity” including genetic diversity (Reusch et al. 2005, Baskett et al. 2009, Agashe 2009), species diversity (Tilman 1994, Chesson 2000, Cadotte et al. 2013), functional diversity (Gazol and Camarero 2016), topoclimatic complexity (Ackerly et al. 2010, Lenoir et al. 2013), and temporal environmental variation (Questad and Foster 2008). An emerging paradigm in forest ecology is that resilience to

## CHAPTER 1. REMOTE SENSING RESISTANCE

disturbances such as wildfire and insect outbreaks may arise from spatial variability in the structure of vegetation (Stephens et al. 2008, North et al. 2009, Virah-Sawmy et al. 2009).

In much of the western United States, forests are experiencing “unhealthy” conditions which compromise their resilience and leaves them prone to catastrophic shifts in ecosystem type (Millar and Stephenson 2015). Warmer temperatures coupled with recurrent drought (i.e., “hotter droughts”) exacerbate water stress on trees (Williams et al. 2013, Millar and Stephenson 2015, Clark et al. 2016) and a century of fire suppression has drastically increased forest density and structural homogeneity (Safford and Stevens 2017, Stevens et al. 2017). Combined, these changes are liable to upset the feedbacks between forest structure and pattern-forming ecological disturbances that historically stabilized the system and made it resilient. In the yellow pine/mixed-conifer forests of California’s Sierra Nevada mountain range, wildfires kill much larger contiguous patches of trees than in the several centuries prior to Euroamerican settlement making natural forest regeneration after these megafires uncertain (Miller and Thode 2007, Safford and Stevens 2017, Stevens et al. 2017, Steel et al. 2018). Forests are essential components of the biosphere with high management priority given their large carbon stores and other valued ecosystem services (Hansen et al. 2013, Millar and Stephenson 2015, Trumbore et al. 2015, Crowther et al. 2015), making it critical to understand how and at what scale spatial structural variability affects forest resilience to disturbance.

Resilience of forest ecosystems is fundamentally challenging to quantify because forests comprise long-lived species, span large geographic extents, and are affected by disturbances at a broad range of spatial scales. The ease or difficulty with which a disturbance changes a system’s state is termed resistance, and it is a key component of resilience (Walker et al. 2004) (though some treatments in forest ecology define “resistance” as a

## INTRODUCTION

distinct process from “resilience”; see Millar et al. (2007)). To assess a forest’s resistance, the relevant state change to measure is the loss of its characteristic native biota—overstory trees (Keith et al. 2013). Using this framework, a forest system that is resistant to wildfire should generally experience less overstory tree mortality when a fire occurs.

Wildfire behavior is inherently complex and is influenced by local weather, topography, and fuel conditions created by a legacy of disturbances at any particular place (Sugihara et al. 2006). For instance, high surface fuel loads and presence of “ladder fuels” in the understory increase the probability of “crowning” fire behavior, which kills a high proportion of trees (Agee and Skinner 2005, Stephens et al. 2008). A structurally variable forest can largely avoid overstory tree mortality because discontinuous fuel loads interrupt crown fire spread, reduced amounts of accumulated ladder fuel decreases the probability of crowning, and because small tree clumps with fewer trees don’t facilitate self-propagating fire behavior (Graham et al. 2004, Scholl and Taylor 2010). In fire-prone forests with relatively intact fire regimes and high structural variability such as in the Jeffrey pine/mixed-conifer forests of the Sierra San Pedro Martir in Baja, California, there tends to be reduced vegetation mortality after wildfires compared to fire-suppressed forests (Stephens et al. 2008). Thus, more structurally variable forests are predicted to persist due to their resistance to inevitable wildfire disturbance (Graham et al. 2004, Moritz et al. 2005, Stephens et al. 2008). However, it has been difficult to test this foundational concept at broad spatial extents, or resolve at what scale variability in forest structure is meaningful for resilience (Kotliar and Wiens 1990).

Wildfire severity typically describes the proportion of vegetation mortality resulting from fire, and can be measured by comparing pre- and postfire satellite imagery for a specific area. This usually requires considerable manual effort for image collation and processing, followed by calibration with field data (Miller and Thode 2007, Miller et al. 2009, De

## CHAPTER 1. REMOTE SENSING RESISTANCE

Santis et al. 2010, Cansler and McKenzie 2012, Veraverbeke and Hook 2013, Parks et al. 2014, Prichard and Kennedy 2014, Edwards et al. 2018, Fernández-García et al. 2018). Efforts to measure severity across broad spatial extents, such as the Monitoring Trends in Burn Severity project (Eidenshink et al. 2007), are motivated by and fulfill management needs in response to individual fires but are unsuitably subjective for characterizing patterns and trends across large numbers of wildfires (Kolden et al. 2015). Automated efforts to remotely assess wildfire have arisen, but they tend to focus on more aggregate measures of wildfire such as whether an area burned or the probability that it burned rather than the severity of the burn (Bastarrika et al. 2011, Goodwin and Collett 2014, Boschetti et al. 2015, Hawbaker et al. 2017), but see (Reilly et al. 2017, Parks et al. 2018). Here, we present a method to automate the measurement of wildfire severity using minimal user inputs: a geometry of interest (a wildfire perimeter or a field plot location) and an alarm date (the date the fire was discovered). This information is readily available in many fire-prone areas (such as California, via the Fire and Resource Assessment Program; [http://frap.fire.ca.gov/projects/fire\\_data/fire\\_perimeters\\_index](http://frap.fire.ca.gov/projects/fire_data/fire_perimeters_index)) or could be derived using existing products (such as the Landsat Burned Area Essential Climate Variable product described in Hawbaker et al. (2017)).

Vegetation characteristics can be measured using remotely-sensed imagery (Rouse et al. 1973, Asner et al. 2016, Young et al. 2017). Texture analysis of these vegetation characteristics can quantify ecologically relevant local environmental heterogeneity across broad spatial extents (Wood et al. 2012, Stein et al. 2014, Huang et al. 2014, Tuanmu and Jetz 2015), which may be used as a direct measure of ecosystem resilience (Kéfi et al. 2014). Developed for image classification and computer vision, texture analysis characterizes each pixel in an image by a summary statistic of its neighboring pixels, and represents a measure of local heterogeneity which itself varies across the landscape (Haralick et al.

## RESULTS

1973). Texture analysis of forested areas detects heterogeneity of overstory vegetation, which corresponds to fuel loading and continuity, capturing the primary influence of vegetation structure on fire behavior.

We use freely-available Landsat satellite data and a new image processing approach to calculate wildfire severity for nearly 1,000 wildfires encompassing a wide size range (down to 4 hectares) and long time series (1984 to 2017) of Sierra Nevada wildfires that burned in yellow pine/mixed-conifer forest. The larger fires that comprise most severity databases are often able to grow large only after escaping initial suppression efforts and burning under extreme fuel and weather conditions (Calkin et al. 2005). We better represent non-extreme fire behavior by measuring severity across a wider range of fire sizes, allowing us to characterize general features of wildfire behavior in this system without bias. We calibrate 56 configurations of our algorithmic approach to ground-based wildfire severity measurements, and select the best performing severity metric to generate a comprehensive, system-wide severity dataset. We pair the resulting extensive database of wildfire severity measures with image texture analysis of vegetation to ask: (1) Does spatial variability in forest structure increase the resilience of California yellow pine/mixed-conifer forests by reducing the severity of wildfires? (2) At what scale does structural variability have the strongest association with wildfire severity? and (3) Does the influence of structural variability on fire severity depend on topography, regional climate, or other conditions?

## Results

We found that the remotely sensed relative burn ratio (RBR) metric of wildfire severity measured across a 48-day interval prior to the wildfire discovery date correlated best

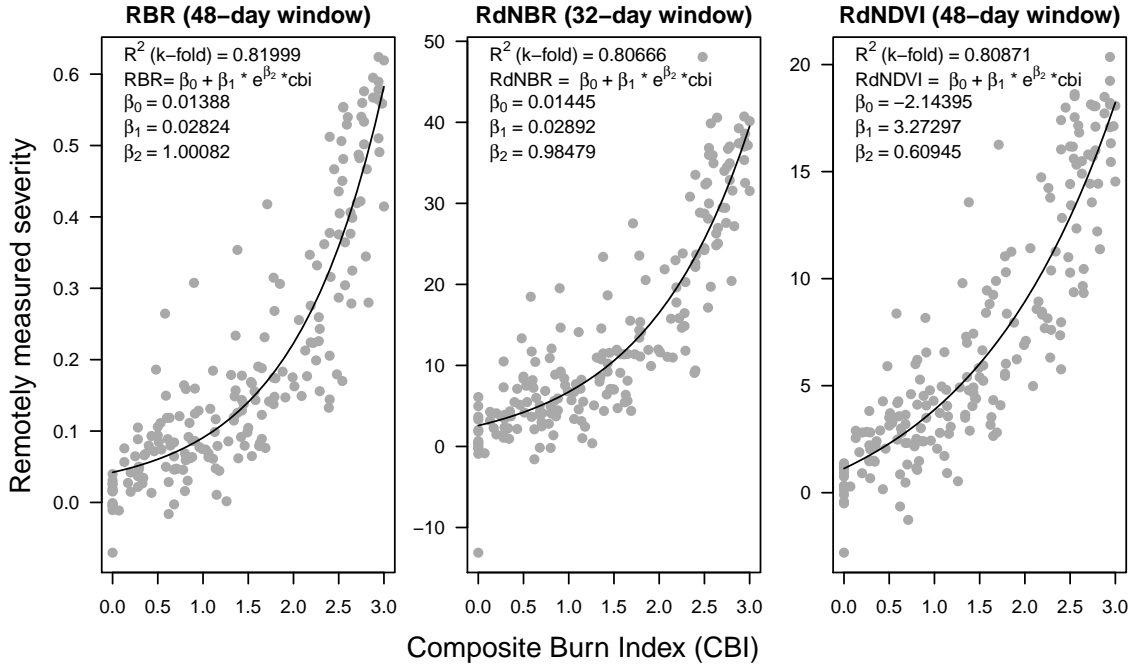


Figure 1.1: Three top performing remotely-sensed severity metrics based on 5-fold cross validation (relative burn ratio, 48-day window, bicubic interpolation; relative delta normalized burn ratio, 32-day window, bilinear interpolation; and relative delta normalized difference vegetation index, 48-day window, bilinear interpolation) calculated using new automated image collation algorithms, calibrated to 208 field measures of fire severity (composite burn index). See Supplemental Table 1 for performance of all tested models.

with ground-based composite burn index (CBI) measurements of severity (5-fold cross validation  $R^2 = 0.82$ ; Figure 1.1; Supp. Table 1). Our method to calculate remotely sensed severity using automated Landsat image fetching performs as well or better than most other reported methods that use hand-curation of Landsat imagery (see review in Edwards et al. (2018)). Further, several combinations of remotely sensed severity metrics, time windows, and interpolation methods validate well with the ground-based severity metrics, including those based on NDVI which is calculated using reflectance in shorter wavelengths than those typically used for measuring severity (Figure 1.1). The top three configurations of our remotely sensed severity metric are depicted in Figure 1.1. Based

## RESULTS

on these model comparisons, we used the relative burn ratio (RBR) calculated using a 48-day time window before the fire and bicubic interpolation as our metric of severity. We created the boolean response variable representing whether the sampled point burned at high-severity or not by determining whether the RBR exceeded 0.282, the threshold for high-severity derived using the non-linear relationship in Equation 1.1 (Figure 1.1).

### Neighborhood size effect

Table 1.1: Comparison of four models described in Eq. 2 using different neighborhood sizes for calculating forest structural variability (standard deviation of NDVI within the neighborhood), neighborhood mean NDVI, and topographic roughness. LOO is a measure of a model’s predictive accuracy (with lower values corresponding to more accurate prediction) and is calculated as -2 times the expected log pointwise predictive density (elpd) for a new dataset (Vehtari et al. 2017).  $\Delta$ LOO is the difference between a model’s LOO and the lowest LOO in a set of models (i.e., the model with the best predictive accuracy). The Bayesian  $R^2$  is a ‘data-based estimate of the proportion of variance explained for new data’ (Gelman et al. 2018). Note that Bayesian  $R^2$  values are conditional on the model so shouldn’t be compared across models, though they can be informative about a single model at a time.

Model	Neighborhood		$\Delta$ LOO			
	measure	size for variability				
			LOO (- 2*elpd)	to best model	SE of $\Delta$ LOO	LOO model weight (%)
1	90m x 90m	40786	0	NA	100	0.299
2	150m x 150m	40842	56.03	14.69	0	0.298
3	210m x 210m	40883	96.87	20.94	0	0.297
4	270m x 270m	40912	125.9	24.73	0	0.297

## CHAPTER 1. REMOTE SENSING RESISTANCE

The model with the best out-of-sample prediction accuracy assessed by leave-one-out cross validation was the model fit using the smallest neighborhood size for the variability of forest structure (standard deviation of neighborhood NDVI), the mean of neighborhood NDVI, and the terrain roughness (standard deviation of elevation) (Table 1.1). Model weighting based on the LOO score suggests 100% of the model weight belongs to the model using the smallest neighborhood size window.

### **Effects of prefire vegetation density, 100-hour fuel moisture, potential annual heat load, and topographic roughness on wildfire severity**

We report the results from fitting the model described in Equation 1.2 using the smallest neighborhood size (90m x 90m) because this was the best performing model (see above) and because the size and magnitude of estimated coefficients were similar across neighborhood sizes (Supp. Table 2).

We found that the strongest influence on the probability of a forested area burning at high-severity was the density of the vegetation, as measured by the prefire NDVI at that central pixel. A greater prefire NDVI led to a greater probability of high-severity fire ( $\beta_{\text{prefire\_ndvi}} = 1.044$ ; 95% CI: [0.911, 1.174]); Figure 1.2). There was a strong negative relationship between 100-hour fuel moisture and wildfire severity such that increasing 100-hour fuel moisture was associated with a reduction in the probability of a high-severity wildfire ( $\beta_{\text{fm100}} = -0.569$ ; 95% CI: [-0.71, -0.423]) (Figure 1.2). Potential annual heat load, which integrates aspect, slope, and latitude, also had a strong positive relationship with the probability of a high-severity fire. Areas that were located on southwest facing sloped terrain at lower latitudes had the highest potential annual heat load, and they were more

## RESULTS

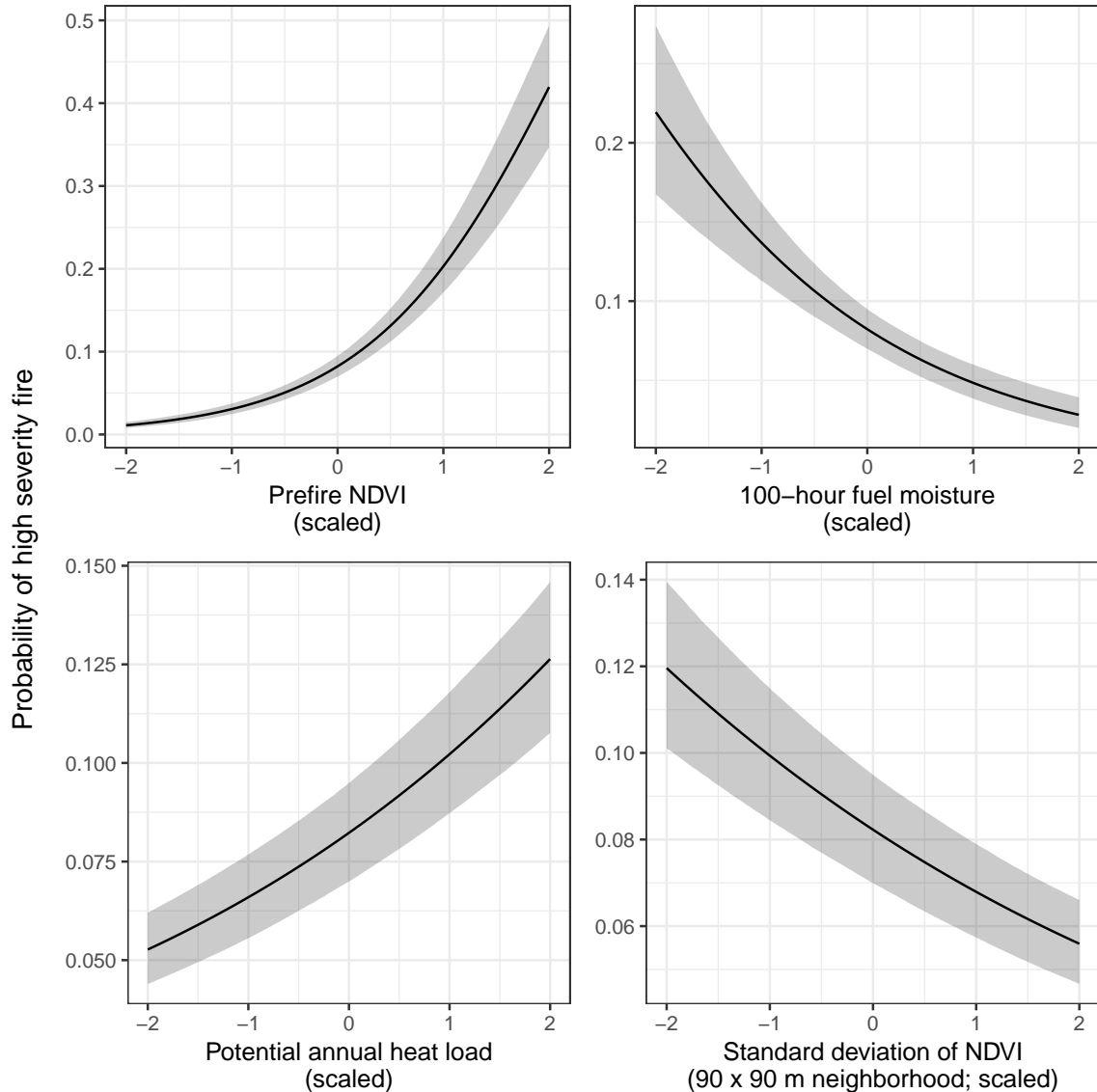


Figure 1.2: The main effects and 95% credible intervals of the covariates having the strongest relationships with the probability of high-severity fire. All depicted relationships derive from the model using the 90m x 90m neighborhood size window for neighborhood standard deviation of NDVI, neighborhood mean of NDVI, and topographic roughness, as this was the best performing model of the four neighborhood sizes tested. The effect sizes of these covariates were similar for each neighborhood size tested.

## CHAPTER 1. REMOTE SENSING RESISTANCE

likely to burn at high-severity ( $\beta_{\text{pahl}} = 0.239$ ; 95% CI: [0.208, 0.271]) Figure 1.2). We found no effect of local topographic roughness on wildfire severity ( $\beta_{\text{topographic\_roughness}} = -0.01$ ; 95% CI: [-0.042, 0.022]). We found a negative effect of the prefire neighborhood mean NDVI on the probability of a pixel burning at high-severity ( $\beta_{\text{nbhd\_mean\_NDVI}} = -0.14$ ; 95% CI: [-0.278, 0.002]). This is in contrast to the positive effect of the prefire NDVI of the pixel itself.

There was also a strong negative interaction between the neighborhood mean NDVI and the prefire NDVI of the central pixel ( $\beta_{\text{nbhd\_mean\_NDVI} * \text{prefire\_NDVI}} = -0.573$ ; 95% CI: [-0.62, -0.526]).

### Effect of variability of vegetation structure on wildfire severity

We found strong evidence for a negative effect of variability of vegetation structure on the probability of a high-severity wildfire ( $\beta_{\text{nbhd\_stdev\_NDVI}} = -0.208$ ; 95% CI: [-0.247, -0.17]); Figure 1.2). We also found significant interactions between variability of vegetation structure and prefire NDVI ( $\beta_{\text{nbhd\_stdev\_NDVI} * \text{prefire\_NDVI}} = 0.125$ ; 95% CI: [0.029, 0.218]) as well as between variability of vegetation structure and neighborhood mean NDVI ( $\beta_{\text{nbhd\_stdev\_NDVI} * \text{nbhd\_mean\_NDVI}} = -0.129$ ; 95% CI: [-0.223, -0.034]).

## Discussion

Broad-extent, fine-grain, spatially-explicit analyses of whole ecosystems are key to illuminating macroecological phenomena (Heffernan et al. 2014). We used a powerful, cloud-based geographic information system and data repository, Google Earth Engine, as a ‘macroscope’ (Beck et al. 2012) to study feedbacks between vegetation structure and wildfire disturbance in yellow pine/mixed-conifer forests of California’s Sierra Nevada

## DISCUSSION

mountain range. With this approach, we reveal and quantify general features of this forest system, and gain deeper insights into the mechanisms underlying its function.

### Factors influencing the probability of high-severity wildfire

We found that the strongest influence on the probability of high-severity wildfire was prefire NDVI. Greater NDVI corresponds to high canopy cover and vegetation density (Rouse et al. 1973) which translate directly to live fuel loads in the forest canopy and can increase high severity fire (Parks et al. 2018). Critically, overstory canopy cover and density also correlate with surface fuel loads (Lydersen et al. 2015, Collins et al. 2016), which play a larger role in driving high severity fire compared to canopy fuel loads in these forests (Stephens et al. 2012). Thus NDVI is likely a strong predictor of fire severity because it is correlated with both surface fuel loads and canopy live fuel density.

We found a strong positive effect of potential annual heat load as well as a strong negative effect of 100-hour fuel moisture, results which corroborates similar studies (Parks et al. 2018). Some work has shown that terrain ruggedness (Holden et al. 2009), and particularly coarser-scale terrain ruggedness (Dillon et al. 2011), is an important predictor of wildfire severity, but we found no effect using our measure of terrain ruggedness.

Critically, we found a strong negative effect of forest structural variability on wildfire severity that was opposite in direction but similar in magnitude to the effect of potential annual heat load. Just as the positive effect of NDVI is likely driven by surface fuel loads, the negative effect of variability in NDVI (our measure of structural variability), is likely driven by discontinuity in surface fuel loads, which can reduce the probability of initiation and spread of tree-killing crown fires (Wagner 1977, Agee and ForestResourcesU 1996, Graham et al. 2004, Agee and Skinner 2005).

## Feedback between forest structural variability and wildfire severity

This system-wide inverse relationship between structural variability and wildfire severity closes a feedback that links past and future fire behavior via forest structure. Frequent, mixed-severity wildfire generates variable forest structure (North et al. 2009, Larson and Churchill 2012, Malone et al. 2018), which in turn, as we demonstrate, dampens the severity of future fire. In contrast, exclusion of wildfire homogenizes forest structure and increases the probability that a fire, when it occurs, will produce large, contiguous patches of overstory mortality (Stevens et al. 2017, Steel et al. 2018). The proportion and spatial configuration of fire severity in fire-prone forests are key determinants of their long-term persistence (Stevens et al. 2017, Steel et al. 2018). Lower-severity fire or scattered patches of higher-severity fire reduce the risk of conversion to a non-forest vegetation type (Stevens et al. 2017, Walker et al. 2018), while prospects for forest regeneration are bleak when high-severity patch sizes are much larger than the natural range of variation for the system (Wagtendonk 2006, Stephens et al. 2009, Millar and Stephenson 2015, Coppoletta et al. 2016, Safford and Stevens 2017, Miller and Safford 2017, Stevens et al. 2017). Thus, the forest-structure-mediated feedback between past and future fire severity underlies the resilience of the Sierra Nevada yellow pine/mixed-conifer system.

## Neighborhood size

We found that the effect of a forest patch's neighborhood characteristics on the probability of high-severity fire was strongest at the smallest neighborhood size that we tested, 90m x 90m. This suggests that the moderating effect of variability in vegetation structure on fire severity is a very local phenomenon. This corroborates work by Safford et al.

## DISCUSSION

(2012), who found that crown fires (with high tree killing potential) were almost always reduced to surface fires (with low tree killing potential) within 70m of entering an fuel reduction treatment area.

At a landscape level, forest treatments that reduce fuel loads and increase structural variability can be effective at reducing fire severity across broader spatial scales (Stephens et al. 2009). This may reflect that severity patterns for a whole fire are an emergent property of very local interactions between forest structure and fire behavior. Some work suggests that the scale of these interactions may depend on even broader-scale effects of fire weather, with small-scale variability failing to influence fire behavior under extreme conditions (Peters et al. 2004, Lydersen et al. 2014), though we did not detect such an interaction. The notion of emergent patterns of severity arising from local effects of vegetation structure is supported by work on fuel reduction treatments, which suggests that fire behavior can be readily modified with forest structural changes to only 20% (when strategically located) to 60% (when randomly located) of the landscape (Graham et al. 2004).

## Correlation between covariates and interactions

Unexpectedly, we found a strong interaction between the prefire NDVI at a pixel and its neighborhood mean NDVI. These two variables are strongly correlated (Spearman's  $\rho = 0.97$ ), so the general effect of this interaction is to dampen the dominating effect of prefire NDVI. Thus, though the marginal effect of prefire NDVI on the probability of high-severity fire is still positive and large, its real-world effect might be more comparable to other modeled covariates when including the negative main effect of neighborhood mean NDVI, the negative interaction effect of prefire NDVI and neighborhood mean NDVI, and their tendency to covary (compare the real-world effect of vegetation density:

## CHAPTER 1. REMOTE SENSING RESISTANCE

$\beta_{\text{prefire\_ndvi}} + \beta_{\text{nbhd\_mean\_NDVI}} + \beta_{\text{nbhd\_mean\_NDVI} * \text{prefire\_NDVI}} = 0.331$ , to the effect of 100-hour fuel moisture, which becomes the effect with the greatest magnitude:  $\beta_{\text{fm100}} = -0.569$ .

In the few cases when prefire NDVI and the neighborhood mean NDVI contrast, there is an overall effect of increasing the probability of high-severity fire. When prefire NDVI at the central pixel is high and the neighborhood NDVI is low (e.g., an isolated vegetation patch; Supplemental Fig. 2), the probability of high-severity fire is expected to dramatically increase. When prefire NDVI at the central pixel is low and the neighborhood NDVI is high (e.g., a hole in the center of an otherwise dense forest; Supplemental Fig. 2), the probability of high-severity fire at that central pixel is still expected to be fairly high even though there is limited vegetation density (see Supplemental Fig. 2). In these forest NDVI datasets, when these variables do decouple, they tend to do so in the “hole in the forest” case and lead to a greater probability of high-severity fire at the central pixel despite the lower vegetation density there. This can perhaps be explained if the consistently high vegetation density in a local neighborhood— itself more likely to burn at high-severity— exerts a contagious effect on the central pixel, raising its probability of burning at high-severity regardless of how much fuel might be there to burn.

## A new approach to remotely sensing wildfire severity

We developed a new approach to calculating wildfire severity leveraging the cloud-based data catalog, the large parallel processing system, and the distribution of computation tasks in Google Earth Engine to enable rapid high-throughput analyses of earth observation data (Gorelick et al. 2017). Our programmatic assessment of wildfire severity across the 972 Sierra Nevada yellow pine/mixed-conifer fires in the FRAP perimeter database, which required fetching thousands of Landsat images and performing dozens of calcula-

## DISCUSSION

tions across them, was automated and took less than an hour to complete. We found that the relative burn ratio (RBR) calculated using prefire Landsat images collected over a 48-day period prior to the fire and postfire Landsat images collected over a 48-day period one year after the prefire images validated the best with ground-based severity measurements (composite burn index; CBI). Further, we found that this method was robust to a wide range of severity metrics, time windows, and interpolation techniques.

Most efforts to calculate severity from satellite data rely on hand curation of a single prefire and a single postfire image (Miller and Thode 2007, Miller et al. 2009, De Santis et al. 2010, Cansler and McKenzie 2012, Veraverbeke and Hook 2013, Parks et al. 2014, Prichard and Kennedy 2014, Edwards et al. 2018, Fernández-García et al. 2018). Recently, Parks et al. (2018) found that using a composite of several prefire images and several postfire images to detect fire impacts performed at least as well as using a single pre- and postfire image. Using composite images also facilitated automated image fetching. Parks et al. (2018) used 3- to 4-month windows during pre-specified times of the year (depending on the fire's region) to collate pre- and postfire imagery one year before the fire and one year after. In contrast, we tested multiple time window lengths based on the fire start date regardless of when it burned during the year. Basing our pre- and postfire image fetching on fixed lengths of time since the fire start date standardized the amount of time elapsed in each severity assessment. Our best remotely sensed severity configuration used a much shorter time window compared to Parks et al. (2018) (48 days versus 3 to 4 months), which likely balanced an incorporation of enough imagery to be representative of the pre- and postfire vegetation conditions but not so many images that different phenological conditions across the time window added noise to each composite.

Many algorithms have been developed to measure fire effects on vegetation in an attempt to better correspond to field data (Key and Benson 2006, Miller and Thode 2007, Parks

## CHAPTER 1. REMOTE SENSING RESISTANCE

et al. 2014). We found that several other remotely sensed measures of severity, including one based on NDVI that is rarely deployed, validated nearly as well with ground-based data as the best configuration (RBR calculated using a 48-day time window). We echo the conclusion of Zhu et al. (2006) that the validation of differences between pre- and postfire NDVI to field measured severity data, which uses near infrared reflectance, is comparable to validation using more commonly used severity metrics (e.g., RdNBR and RBR) that rely on short wave infrared reflectance. One immediately operational implication of this is that the increasing availability of low-cost small unhumanned aerial systems (sUAS a.k.a. drones) and near-infrared-detecting imagers (e.g., those used for agriculture monitoring) may be used to reliably measure wildfire severity at very high spatial resolutions.

## Conclusions

While the severity of a wildfire in any given place is controlled by many variables, we have presented strong evidence that, across large areas of forest, variable forest structure generally makes yellow pine/mixed-conifer forest in the Sierra Nevada more resistant to this inevitable disturbance. It has been well-documented that frequent, low-severity wildfire maintains forest structural variability. Here, we demonstrate a system-wide reciprocal effect suggesting that greater local-scale variability of vegetation structure makes fire-prone, dry forests more resilient to wildfire and may increase the probability of their long-term persistence.

## MATERIAL AND METHODS

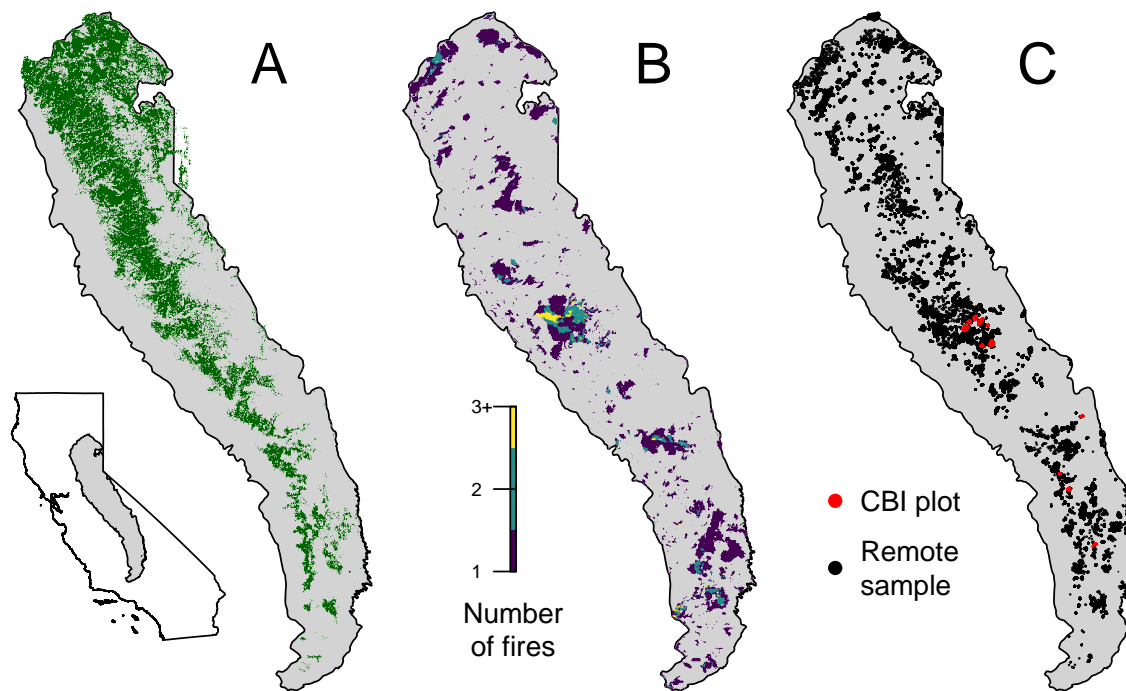


Figure 1.3: Geographic setting of the study. A) Location of yellow pine/mixed-conifer forests as designated by the Fire Return Interval Departure (FRID) product which, among other things, describes the potential vegetation in an area based on the pre-Euroamerican settlement fire regime. B) Locations of all fires covering greater than 4 hectares that burned in yellow pine/mixed-conifer forest between 1984 and 2017 in the Sierra Nevada mountain range of California according to the State of California Fire Resource and Assessment Program database, the most comprehensive database of fire perimeters of its kind. Colors indicate how many fire perimeters overlapped a given pixel within the study time period. C) (red) Locations of 208 composite burn index (CBI) ground plots used to calibrate the remotely sensed measures of severity. (black) Locations of random samples drawn from 972 unique fires depicted in panel B that were in yellow pine/mixed-conifer forest as depicted in panel A, and which were designated as “burned” by exceeding a threshold relative burn ratio (RBR) determined by calibrating the algorithm presented in this study with ground-based CBI measurements.

## Material and Methods

### Study system

Our study assesses the effect of vegetation structure on wildfire severity in the Sierra Nevada mountain range of California in yellow pine/mixed-conifer forests (Figure 1.3). This system is dominated by a mixture of conifer species including ponderosa pine (*Pinus ponderosa*), sugar pine (*Pinus lambertiana*), incense-cedar (*Calocedrus decurrens*), Douglas-fir (*Pseudotsuga menziesii*), white fir (*Abies concolor*), and red fir (*Abies magnifica*), angiosperm trees primarily including black oak (*Quercus kelloggii*), as well as shrubs (Safford and Stevens 2017). We considered “yellow pine/mixed-conifer forest” to be all areas designated as a yellow pine, dry mixed-conifer, or moist mixed-conifer pre-settlement fire regime (PFR) in the USFS Fire Return Interval Departure database (<https://www.fs.usda.gov/detail/r5/landmanagement/gis/?cid=STELPRDB5327836>), which reflects potential vegetation and is less sensitive to recent land cover change (Steel et al. 2018). We considered the Sierra Nevada region to be the area within the Sierra Nevada Foothills, the High Sierra Nevada, and the Tehachapi Mountain Area Jepson ecoregions (JepsonFloraProject 2016).

### A new approach to remotely sensing wildfire severity

We measured forest vegetation characteristics and wildfire severity using imagery from the Landsat series of satellites (Miller and Thode 2007, Eidenshink et al. 2007) with radiometric correction post-processing (Masek et al. 2006, Vermote et al. 2016, USGS 2017a, 2017b). Landsat satellites image the entire Earth approximately every 16 days

## MATERIAL AND METHODS

with a 30m pixel resolution. We used Google Earth Engine, a massively parallel cloud-based geographic information system and image hosting platform, for all image collation and processing (Gorelick et al. 2017).

We calculated wildfire severity for the most comprehensive digital record of fire perimeters in California: The California Department of Forestry and Fire Protection, Fire and Resource Assessment Program (FRAP) fire perimeter database ([http://frap.fire.ca.gov/projects/fire\\_data/fire\\_perimeters\\_index](http://frap.fire.ca.gov/projects/fire_data/fire_perimeters_index)). The FRAP database includes all known fires that covered more than 4 hectares, compared to the current standard severity database in this region which only includes fires covering greater than 80 hectares (Miller and Thode 2007, Miller et al. 2012, Miller and Safford 2012, Steel et al. 2018). Using the FRAP database of fire perimeters, we quantified fire severity within each perimeter of 972 wildfires in the Sierra Nevada yellow pine/mixed-conifer forest that burned between 1984 and 2017. Our approach more than doubles the number of fire events represented from 430 to 972, though only increases the total burned area represented from 7.44e+05 to 7.69e+05 hectares because most of the additional fires are small. We use a consistent algorithmic approach to calculate fire severity across all fires, avoiding subjective judgments that some previous approaches have used to characterize severity separately for each fire.

### Fetching and processing pre- and postfire imagery

For each fire perimeter, we fetched a time series of prefire Landsat images starting the day before the fire alarm date and extending backward in time by a user-defined time window. An analogous postfire time series of Landsat imagery was fetched exactly one year after the date range used to filter the prefire collection. We tested 4 time windows: 16, 32, 48, or 64 days which were chosen to ensure that at least 1, 2, 3, or 4 Landsat

## CHAPTER 1. REMOTE SENSING RESISTANCE

images were captured by the date ranges (Supplemental Fig. 1). The Landsat archive we filtered included imagery from Landsat 4, 5, 7, and 8, so each pre- and postfire image collection may contain a mix of scenes from different satellite sources to enhance coverage. For each image in the pre- and postfire image collections, we masked pixels that were not clear (i.e., clouds, cloud shadows, snow, and water) using the CFMask algorithm (Foga et al. 2017).

For each Landsat image in the prefire and postfire collections, we calculated standard indices that capture vegetation cover and fire effects such as charring. Normalized difference vegetation index (NDVI) correlates with vegetation density, canopy cover, and leaf area index (Rouse et al. 1973). Normalized burn ratio (NBR) and normalized burn ratio version 2 (NBR2) respond strongly to fire effects on vegetation (García and Caselles 1991, Key and Benson 2006, USGS 2017b, 2017a, Hawbaker et al. 2017) (Equations in Supplemental Methods).

We composited each prefire image collection (including the pixel values representing NDVI, NBR, and NBR2) into a single prefire image and each postfire image collection into a single postfire image, by calculating the median of the unmasked values on a per-pixel basis across the stack of images in each pre- and postfire collection. Composite pre- and postfire images can be successfully used to measure wildfire severity instead of using raw, individual images (Parks et al. 2018).

We composited each pre- and postfire image collection (including the pixel values representing NDVI, NBR, and NBR2) into a single pre- and postfire image using a median reducer, which calculated the median of the unmasked values on a per-pixel basis across the stack of images in each collection. Composite pre- and postfire images can be successfully used to measure wildfire severity instead of using raw, individual images (Parks et al. 2018).

## MATERIAL AND METHODS

### Calculating wildfire severity

Using the compositing approach, we calculated the most commonly used metrics of remotely-sensed wildfire severity to validate against ground-based data: the relative burn ratio (RBR) (Parks et al. 2014), the delta normalized burn ratio (dNBR) (Miller and Thode 2007, Eidenshink et al. 2007), the relative delta normalized burn ratio (RdNBR) (Miller and Thode 2007, Miller and Safford 2012), the delta normalized burn ratio 2 (dNBR2) (Hawbaker et al. 2017), the relative delta normalized burn ratio 2 (RdNBR2), and the delta normalized difference vegetation index (dNDVI) (Eidenshink et al. 2007). We also calculate a new, analogous metric to the RdNBR using NDVI– the relative delta normalized difference vegetation index (RdNDVI). We calculated the delta severity indices (dNBR, dNBR2, dNDVI) without multiplying by a rescaling constant (e.g., we did not multiply the result by 1000 as in Miller and Thode (2007)). Following Reilly et al. (2017), we did not correct the delta indices using a phenological offset value, as our approach implicitly accounts for phenology by incorporating multiple cloud-free images across the same time window both before the fire and one year later. (Full equations can be found in the Supplemental Methods)

Example algorithm outputs are shown in Figure 1.4.

### Calibrating remotely-sensed wildfire severity with field-measured wildfire severity

We calibrated our remotely-sensed measure of wildfire severity with 208 field measures of overstory tree mortality from two previously published studies (Zhu et al. 2006, Sikkink et al. 2013) (Figure 1.3). The Composite Burn Index (CBI) is a metric of vegetation mortality across several vertical vegetation strata within a 30m diameter field plot (Key

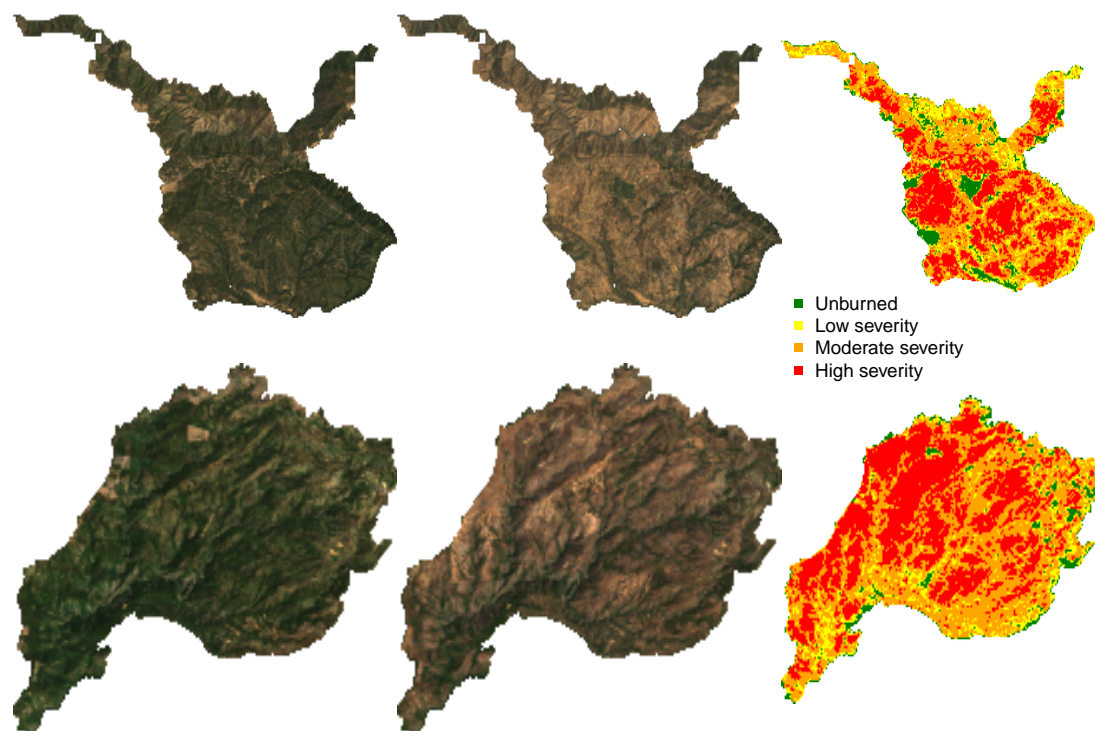


Figure 1.4: Example algorithm outputs for the Hamm Fire of 1987 (top half) and the American Fire of 2013 (bottom half) showing: prefire true color image (left third), postfire true color image (center third), relative burn ratio (RBR) calculation using a 48-day image collation window before the fire and one year later (right third). For visualization purposes, these algorithm outputs have been resampled to a resolution of 100m x 100m from their original resolution of 30m x 30m. Data used for analyses were sampled from the outputs at the original resolution.

## MATERIAL AND METHODS

and Benson 2006). The CBI ranges from 0 (no fire impacts) to 3 (very high fire impacts), and has a long history of use as a standard for calibrating remotely-sensed severity data (Key and Benson 2006, Miller and Thode 2007, Miller et al. 2009, Cansler and McKenzie 2012, Parks et al. 2014, 2018, Prichard and Kennedy 2014). Following Miller and Thode (2007), Miller et al. (2009), Parks et al. (2014), and Parks et al. (2018), we fit a non-linear model to each remotely-sensed severity metric of the following form:

$$(1) \text{ remote\_severity} = \beta_0 + \beta_1 e^{\beta_2 \text{cbi\_overstory}}$$

We fit the model in Equation 1.1 for all 7 of our remotely-sensed severity metrics (RBR, dNBR, RdNBR, dNBR2, RdNBR2, dNDVI, RdNDVI) using 4 different time windows from which to collate satellite imagery (16, 32, 48, and 64 days). Following Cansler and McKenzie (2012), Parks et al. (2014), and Parks et al. (2018), we used bilinear interpolation to extract remotely-sensed severity at the locations of the CBI field plots to better align remote and field measurements. We also extracted remotely-sensed severity values using bicubic interpolation. In total, we fit 56 models (7 severity measures, 4 time windows, 2 interpolation methods) and performed five-fold cross validation using the `modelr` and `purrr` packages in R (R Core Team 2018, Henry and Wickham 2019, Wickham 2019). To compare goodness of model fits with Miller and Thode (2007), Miller et al. (2009), and Parks et al. (2014), we report the average  $R^2$  value from the five folds for each of the 56 models.

## Remote sensing other conditions

### Vegetation structural variability

We used texture analysis to calculate a remotely-sensed measure of local forest variability (Haralick et al. 1973, Tuanmu and Jetz 2015). Within a moving square neighborhood

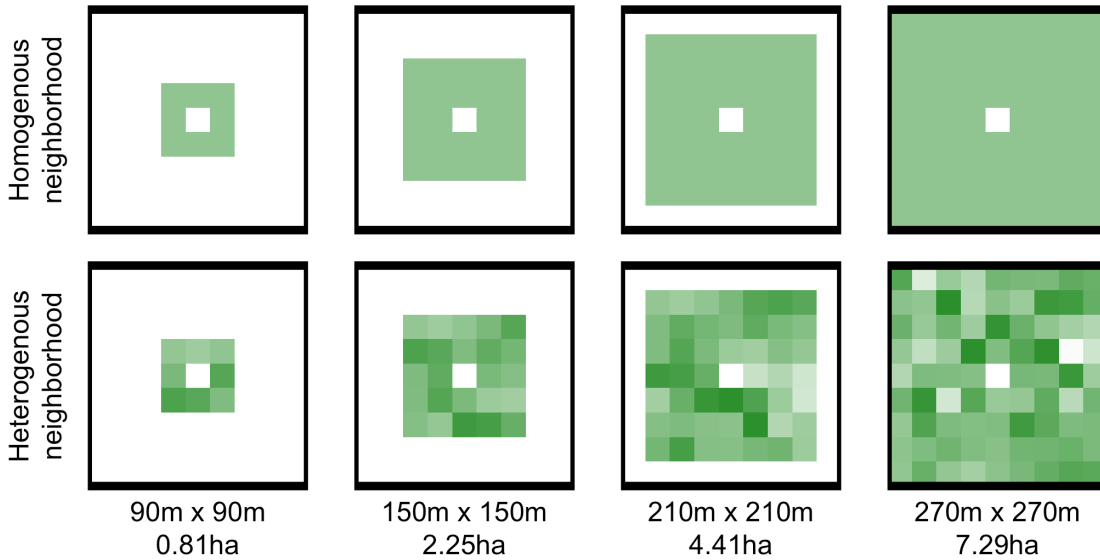


Figure 1.5: Example of homogenous forest (top row) and heterogenous forest (bottom row) with the same mean NDVI values ( $\sim 0.6$ ). Each column represents forest structural variability measured using a different neighborhood size.

window with sides of 90m, 150m, 210m, and 270m, we calculated forest variability for each pixel as the standard deviation of the NDVI values of its neighbors (not including itself). NDVI correlates well with foliar biomass, leaf area index, and vegetation cover (Rouse et al. 1973), so a higher standard deviation of NDVI within a given local neighborhood corresponds to discontinuous canopy cover and abrupt vegetation edges (see Figure 1.5) (Franklin et al. 1986). Canopy cover is positively correlated with surface fuel loads including dead and down wood, grasses, and short shrubs (Lydersen et al. 2015, Collins et al. 2016), which are primarily responsible for initiation and spread of “crowning” fire behavior which kills overstory trees (Stephens et al. 2012).

## MATERIAL AND METHODS

### Topographic conditions

Elevation data were sourced from the Shuttle Radar Topography Mission (Farr et al. 2007), a 1-arc second digital elevation model. Slope and aspect were extracted from the digital elevation model. Per-pixel topographic roughness was calculated as the standard deviation of elevation values within the same-sized kernels as those used for variability in forest structure (90m, 150m, 210m, and 270m on a side and not including the central pixel).

We used the digital elevation model to calculate the potential annual heat load at each pixel, which is an integrated measure of latitude, slope, and a folding transformation of aspect about the northeast-southwest line (McCune and Keon (2002) with correction in McCune (2007); See Supplemental Methods for equations)

### Moisture conditions

The modeled 100-hour fuel moisture data were sourced from the gridMET product, a gridded meteorological product with a daily temporal resolution and a 4km x 4km spatial resolution (Abatzoglou 2013). We calculated 100-hour fuel moisture as the median 100-hour fuel moisture for the 3 days prior to the fire. The 100-hour fuel moisture is a correlate of the regional temperature and moisture which integrates the relative humidity, the length of day, and the amount of precipitation in the previous 24 hours. Thus, this measure is sensitive to multiple hot dry days across the 4km x 4km spatial extent of each grid cell, but not to diurnal variation in relative humidity nor to extreme weather events during a fire.

### Remote samples

Approximately 100 random points were selected within each FRAP fire perimeter in areas designated as yellow pine/mixed-conifer forest and the values of wildfire severity as well as the values of each covariate were extracted at those points using nearest neighbor interpolation. Using the calibration equation described in Equation 1.1 for the best configuration of the remote severity metric, we removed sampled points corresponding to “unburned” area prior to analysis (i.e., below an RBR threshold of 0.045). The random sampling amounted to 54109 total samples across 972 fires.

### Modeling the effect of forest variability on severity

We used the Relative Burn Ratio (RBR) calculated using bicubic interpolation within a 48-day window to derive our response variable for analyses of forest structural variability, as it showed the best correspondence to field severity data measured as average  $R^2$  in the 5-fold cross validation. Using the non-linear relationship between RBR and CBI from the best performing calibration model, we calculated the threshold RBR corresponding to “high-severity” signifying complete or near-complete overstory mortality (RBR value of 0.282 corresponding to a CBI value of 2.25). If the severity at a remote sample point was greater than this threshold, the point was scored as a 1. We used a hierarchical logistic regression model (Equation 1.2) to assess the probability of high-severity wildfire as a linear combination of the remote metrics described above: prefire NDVI of each pixel, standard deviation of NDVI within a neighborhood (i.e., forest structural variability), the mean NDVI within a neighborhood, 100-hour fuel moisture, potential annual heat load, and topographic roughness. We included two-way interactions between the structural variability measure and prefire NDVI, neighborhood mean NDVI, and 100-hour

## MATERIAL AND METHODS

fuel moisture. We include the two-way interaction between a pixel's prefire NDVI and its neighborhood mean NDVI to account for structural variability that may arise from differences between these variables (see Supplemental Fig. 2). We scaled all predictor variables, used weakly-regularizing priors, and estimated an intercept for each individual fire with pooled variance.

$$\begin{aligned}
 (2) \quad logit(\phi_{i,j}) = & \beta_0 + \\
 & \beta_{\text{nbhd\_sd\_NDVI}} * \text{nbhd\_sd\_NDVI}_i + \\
 & \beta_{\text{NDVI}} * \text{NDVI}_i + \\
 & \beta_{\text{nbhd\_mn\_NDVI}} * \text{nbhd\_mn\_NDVI}_i + \\
 & \beta_{\text{fm100}} * \text{fm100}_i + \\
 & \beta_{\text{pahl}} * \text{pahl}_i + \\
 & \beta_{\text{topographic\_roughness}} * \text{topographic\_roughness}_i + \\
 & \beta_{\text{nbhd\_sd\_NDVI*fm100}} * \text{nbhd\_sd\_NDVI}_i * \text{fm100}_i + \\
 & \beta_{\text{nbhd\_sd\_NDVI*NDVI}} * \text{nbhd\_sd\_NDVI}_i * \text{NDVI}_i + \\
 & \beta_{\text{nbhd\_sd\_NDVI*nbhd\_mn\_NDVI}} * \text{nbhd\_sd\_NDVI}_i * \text{nbhd\_mn\_NDVI}_i + \\
 & \beta_{\text{nbhd\_mn\_NDVI*NDVI}} * \text{nbhd\_mn\_NDVI}_i * \text{NDVI}_i + \\
 & \gamma_j \\
 \gamma_j \sim & \mathcal{N}(0, \sigma_{\text{fire}})
 \end{aligned}$$

## Assessing the relevant scale of forest variability

Each neighborhood size (90m, 150m, 210m, 270m on a side) was substituted in turn for the neighborhood standard deviation of NDVI, neighborhood mean NDVI, and terrain

## CHAPTER 1. REMOTE SENSING RESISTANCE

ruggedness covariates to generate a candidate set of 4 models. To assess the scale at which the forest structure variability effect manifests, we compared the 4 candidate models based on different neighborhood sizes using leave-one-out cross validation (LOO cross validation) (Vehtari et al. 2017). We inferred that the neighborhood size window used in the best-performing model reflected the scale at which the forest structure variability effect had the most support.

### Statistical software

We used R for all statistical analyses (R Core Team 2018). We used the `brms` package to fit mixed effects models in a Bayesian framework which implements the No U-Turn Sampler (NUTS) extension to the Hamiltonian Monte Carlo algorithm (Hoffman and Gelman 2014, Bürkner 2017). We used 4 chains with 3000 samples per chain (1500 warmup samples and 1500 posterior samples) and chain convergence was assessed for each estimated parameter by ensuring Rhat values were less than or equal to 1.01 (Bürkner 2017).

### Data availability

All data and analysis code are available via the Open Science Framework (<https://osf.io/27nsr/>) including a new dataset representing wildfire severity, vegetation characteristics, and regional climate conditions within the perimeters of 1,090 fires from the FRAP database that burned in yellow pine/mixed-conifer forest in the Sierra Nevada, California between 1984 and 2017.

## *ACKNOWLEDGEMENTS*

### **Acknowledgements**

We thank Connie Millar and Derek Young for valuable comments about this work and we also thank the community of Google Earth Engine developers for prompt and helpful insights about the platform. Funding was provided by NSF Graduate Research Fellowship Grant #DGE- 1321845 Amend. 3 (to MJK).

# **Chapter 2**

## **Differential response of a tree-killing bark beetle to host tree size across a gradient of climatic water deficit**

Michael J. Koontz<sup>1,2,\*</sup>, Andrew M. Latimer<sup>1,2</sup>, Leif A. Mortenson<sup>3</sup>, Christopher J. Fettig<sup>3</sup>,  
Malcolm P. North<sup>1,2,4</sup>

<sup>1</sup>Graduate Group in Ecology, University of California, Davis, CA, USA

<sup>2</sup>Department of Plant Sciences, University of California, Davis, CA, USA

<sup>3</sup>USDA Forest Service, Pacific Southwest Research Station, Placerville, CA, USA

<sup>4</sup>USDA Forest Service, Pacific Southwest Research Station, Mammoth Lakes, CA, USA

### **Abstract**

The recent Californian hot drought of 2012 to 2015 created favorable conditions for unprecedented ponderosa pine mortality in the driest, densest portions of the Sierra Nevada

## ABSTRACT

mountain range, largely caused by the western pine beetle (*Dendroctonus brevicomis*). Climate conditions related to tree water stress as well as forest structure can influence the severity of forest insect disturbance, but it remains challenging to consider how these variables may interact to produce patterns of tree mortality. Previous studies have shown an interaction between climate conditions and forest density in their effect on tree mortality, but density is a coarse gauge of forest structure that can affect western pine beetle behavior in a number of ways. Measuring broad-scale climate conditions simultaneously with complex forest structure— including tree species, tree size, and local density— will refine our understanding of how these variables interact, but is generally expensive and/or labor-intensive. We overcame these hurdles by using a small, unhumanned aerial system (hereafter ‘drone’) to conduct aerial surveys over an established network of 32 forest plots along a 350km and 1000m elevation gradient in western slope Sierra yellow pine/mixed-conifer forests. Using Structure from Motion (SfM) processing on over 450,000 images and field measurements from the coincident ground plots, we determined tree size, location, and species for individual trees over 9 square kilometers of forest that experienced ponderosa pine mortality as a result of western pine beetle activity. We modeled the probability of ponderosa pine mortality as a linear combination of forest structure variables and site-level climatic water deficit, and used a Gaussian process to estimate the spatial covariance in the response.

We found that greater host density strongly increased the probability of host mortality, and greater host size generally decreased the probability of host mortality. There was also a strong three-way interaction between host density, host size, and climatic water deficit such that host density and host size tended to synergistically increase the probability of host mortality at hot/dry sites, but denser, smaller trees tended to drive mortality in cool/wet sites.

## CHAPTER 2. LOCAL STRUCTURE; WESTERN PINE BEETLE SEVERITY

Our results demonstrate a variable response of the western pine beetle to complex forest structure across an environmental gradient during the same hot drought, which may indicate forest sites were in different stages of disturbance (from “endemic” to “outbreak”) depending on their regional climate. Management interventions that reduce stem density may decrease the severity of western pine beetle disturbance in the future, and our results suggest that focusing these treatments on areas that are most likely to exceed feedback thresholds (i.e., hot/dry sites with many available hosts) will have the best chance of increasing the survivorship probability of larger trees.

## Introduction

Aggressive bark beetles dealt the final blow to many of the nearly 150 million trees killed in the California hot drought of 2012 to 2015 and its aftermath (USDAFS [2019](#)). A harbinger of climate change effects to come, record high temperatures exacerbated the drought (Griffin and Anchukaitis [2014](#)), which increased water stress on trees (Asner et al. [2016](#)), making them more susceptible to attacking bark beetles (Fettig [2012](#), Kolb et al. [2016](#)). A century of fire suppression policy has enabled forests to grow into dense stands, which also makes them more vulnerable to bark beetle attack (Fettig [2012](#)). This combination of environmental conditions and forest structural characteristics led to tree mortality events of unprecedented size in the driest, densest forests across the state (Young et al. [2017](#)). The mechanisms underlying the link between tree susceptibility to insect attack and hot, dry conditions are often directly attributed to tree physiology (Bentz et al. [2010](#)), while the link to forest density is multifaceted (Fettig [2012](#)). Because forest density is a coarse metric of the complex forest structure to which bark beetles respond (Raffa et al. [2008](#)), our understanding of the connection between forest density

## INTRODUCTION

and insect disturbance severity could be enhanced with more finely-resolved measures of forest structure, such as tree size, tree species, and local density within a forest stand (Stephenson et al. 2019, Fettig et al. 2019). Further, the interaction between local-scale complex forest structure and broad-scale environmental conditions as they affect forest insect disturbance remains underexplored (Seidl et al. 2016, Stephenson et al. 2019, Fettig et al. 2019).

The yellow pine/mixed-conifer forests in California’s Sierra Nevada region are characterized by regular bark beetle disturbances, primarily by the western pine beetle (*Dendroctonus brevicomis*) and its main host in the system, ponderosa pine (*Pinus ponderosa*) (Fettig et al. 2019). The western pine beetle is a “primary” or “aggressive” bark beetle, with reproductive success contingent upon enough beetles “mass attacking” the host tree, overwhelming its defenses, and causing mortality (Raffa and Berryman 1983, Fettig et al. 2019). This Allee effect creates a strong coupling between beetle host selection behavior and host tree susceptibility to attack (Raffa and Berryman 1983, Logan et al. 1998). Under normal conditions, weakened trees are the most susceptible to attack and will be the main targets of aggressive bark beetles like the western pine beetle (Bentz et al. 2010, Raffa et al. 2015). A key defense mechanism of trees to bark beetle attack is to flood beetle bore holes with resin, which physically expels beetles and may interrupt beetle communication (Raffa et al. 2015). Under severe water stress, trees no longer have the resources available to mount this defense (Kolb et al. 2016) and thus prolonged drought can often trigger increased bark beetle-induced tree mortality as average tree vigor declines (Bentz et al. 2010). As local beetle density increases due to successful reproduction on spatially-aggregated weakened trees, as might occur in a prolonged drought, mass attacks become capable of overwhelming any tree’s defenses and even healthy trees become susceptible (Bentz et al. 2010, Raffa et al. 2015). Thus, water

## CHAPTER 2. LOCAL STRUCTURE; WESTERN PINE BEETLE SEVERITY

stress can be a key determinant of whether individual trees are susceptible to bark beetle attack under many conditions, and this environmental condition may interact with other forest features, such as tree size, to drive susceptibility under extreme conditions (Bentz et al. 2010, Stephenson et al. 2019).

Forest structure— often characterized as the spatial distribution, size, and species composition of trees— also strongly influences western pine beetle activity. For instance, high-density forests are more prone to bark beetle attacks, and several mechanism likely underlie this phenomenon (Fettig 2012). A high-density forest may experience greater bark beetle-induced tree mortality for several reasons including: a) host availability is high and shorter dispersal distances facilitate successful colonization of those hosts (Miller and Keen 1960, Berryman 1982, Fettig et al. 2007); b) high host availability reduces the chance of individual beetles wasting their limited resources flying to and landing on a non-host tree (Moeck et al. 1981, Evenden et al. 2014); c) crowded trees experience greater competition for water resources and thus average tree resistance is lower (Hayes et al. 2009); or d) smaller gaps between trees protect pheromone plumes from dissipation by the wind and thus enhance intraspecific beetle communication (Thistle et al. 2004). Additionally, tree size affects bark beetle host selection behavior as smaller trees tend to have less capacity for resisting attack, but larger trees represent a more desirable target because their thicker phloem provides greater nutritional value (Chubaty et al. 2009, Graf et al. 2012). Tree density thus paints a fundamentally limited picture of the mechanism by which forest structure affects bark beetle disturbance, but *complex* forest structure— with explicit recognition of tree size, species composition (e.g., host versus non-host composition), and local tree density— should more appropriately capture the ecological processes underlying insect-induced tree mortality. Additionally, considering the effects of complex forest structure simultaneously to the effects of environmental

## INTRODUCTION

conditions may help refine our understanding of observed patterns of tree mortality in the recent California hot drought.

The vast spatial extent of tree mortality in the 2012 to 2015 California hot drought (US-DAFS 2019) challenges our ability to simultaneously consider how broad-scale environmental conditions may interact with local, complex forest structure to affect the dynamic between bark beetle host selection and host tree susceptibility to attack (Anderegg et al. 2015, Stephenson et al. 2019). Measuring complex forest structure generally requires expensive instrumentation (Kane et al. 2014, Asner et al. 2016) or labor-intensive field surveys (Larson and Churchill 2012, Stephenson et al. 2019), which constrains survey extent and frequency. Small, unhumanned aerial systems (sUAS) enable relatively fast and cheap remote imaging over dozens of hectares of forest, which can be used to measure complex forest structure at the individual tree scale (Morris et al. 2017, Shiklomanov et al. 2019). Distributing such surveys across an environmental gradient is a viable approach to overcoming the data acquisition challenge inherent in investigating phenomena with both a strong local- and a strong broad-scale component.

We used ultra-high resolution, drone-derived remote sensing data over a network of 32 sites in Sierra Nevada yellow pine/mixed-conifer forests spanning 1000m of elevation and 350km of latitude and covering a total of 9 square kilometers to ask how broad-scale environmental conditions interacted with local, complex forest structure to affect the probability of tree mortality during the cumulative tree mortality event of 2012 to 2018.

We asked:

1. How does host tree density and average host tree size affect the severity of western pine beetle disturbance?
2. How does tree density of all species (hereafter “overall density”) and average tree

## CHAPTER 2. LOCAL STRUCTURE; WESTERN PINE BEETLE SEVERITY

size of all species (hereafter “overall size”) affect the severity of western pine beetle disturbance?

3. How does environmentally-driven tree moisture stress affect the severity of western pine beetle disturbance?
4. Do the effects of forest structure and environmental condition on western pine beetle disturbance interact?

## Methods

### Study system

The study sites were chosen to reflect typical west-side Sierra Nevada yellow pine/mixed-conifer forests and were dominated by ponderosa pine trees, *Pinus ponderosa* (Fettig et al. 2019), whose primary bark beetle predator in California is the western pine beetle (WPB), *Dendroctonus brevicomis*. The typical life cycle of WPBs consists of pioneer beetles dispersing to a new host tree, determining the host’s susceptibility to attack, and using pheromone signals to attract other WPBs. The attracted WPBs mass attack the tree by boring into its inner bark, laying eggs, and dying, leaving their offspring to develop inside the doomed tree before themselves dispersing to a new potential host (Raffa et al. 2008). In California, the WPB can have 2-3 generations in a single year and can often out-compete its congener, the mountain pine beetle, *Dendroctonus ponderosa* (MPB), for the ponderosa pine host (Fettig et al. 2019).

We built our study on 180 vegetation/forest insect monitoring plots at 36 sites established between 2016 and 2017 by Fettig et al. (2019) (Figure 2.1). These established plots were located in WPB-attacked, yellow pine/mixed-conifer forests across the Eldorado,

## METHODS

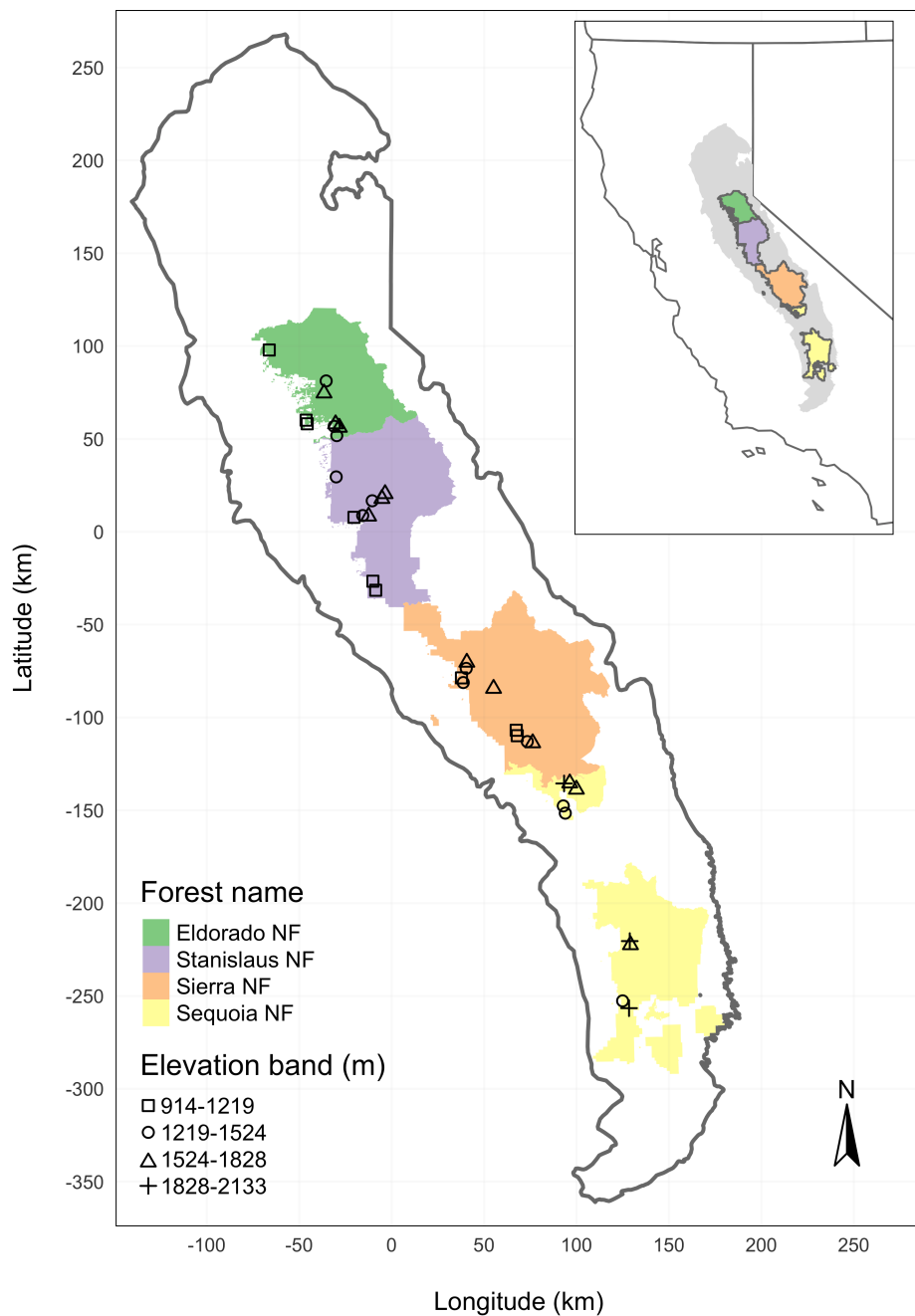


Figure 2.1: The network of field plots spanned a 350 km latitudinal gradient from the Eldorado National Forest in the north to the Sequoia National Forest in the south. Plots were stratified by three elevation bands in each forest, with the plots in the Sequoia National Forest (the southern-most National Forest) occupying elevation bands 305m above the three bands in the other National Forests in order to capture a similar community composition.

## CHAPTER 2. LOCAL STRUCTURE; WESTERN PINE BEETLE SEVERITY

Stanislaus, Sierra and Sequoia National Forests and were stratified by elevation (914-1219 meters [3000-4000 feet], 1219-1524 meters [4000-5000 feet], 1524-1828 meters [5000-6000 feet] above sea level). In the Sequoia National Forest, the southernmost National Forest in our study, plots were stratified with the lowest elevation band between 1219 and 1524 meters (4000-5000 feet) and extended to an upper elevation band of 1828-2133 meters (6000-7000 feet) to capture a more similar forest community composition as at the more northern National Forests. The sites have variable forest structure and plot locations were selected in areas with >40% ponderosa pine basal area and >10% ponderosa pine mortality. At each site, five 0.04 ha circular plots were installed along transects with between 80 and 200m between each plot. In the field, Fettig et al. (2019) mapped all stem locations relative to the center of each plot using azimuth/distance measurements. Tree identity to species, tree height, and diameter at breast height (DBH) were recorded if DBH was greater than 6.35cm. Year of mortality was estimated based on needle color and retention, if it wasn't directly observed between site visits. A small section of bark was removed from dead trees to confirm insect activity. During the spring and early summer of 2018, all field plots were revisited to assess whether dead trees had fallen (Fettig et al. 2019).

## Instrumentation

Imagery was captured using a DJI Zenmuse X3 RGB camera (DJI 2015a) and a Micasense RedEdge3 5-band multispectral camera (Micasense 2015). We mounted both of these instruments simultaneously on a DJI Matrice 100 aircraft (DJI 2015b) using the DJI 3-axis stabilized gimbal for the Zenmuse X3 camera and a Micasense angled fixed mount for the RedEdge3 camera. The gimbal and the angled fixed mount ensured both instruments were nadir-facing during image capture. Just prior to or after image capture at each site,

## METHODS

we calibrated the RedEdge3 camera by taking an image of a calibration panel on the ground in full sun with known reflectance values for each of the 5 narrow bands (Table 2.1).

Table 2.1: Reflectance sensitivity of the Micasense Rededge3 camera. The calibration panel value represents the reflectance of the calibration panel for the given wavelength.

Band number	Band name	Center wavelength	Band width	Wavelength range	Panel reflectance
1	blue (b)	475	20	465-485	0.64
2	green (g)	560	20	550-570	0.64
3	red (r)	668	10	663-673	0.64
4	near infrared (nir)	840	40	820-860	0.6
5	red edge (re)	717	10	712-722	0.63

## Flight protocol

Image capture was conducted as close to solar noon as possible to minimize shadow effects (varying primarily due to site accessibility; always within 4 hours, usually within 2 hours). Prior to the aerial survey, two strips of bright orange drop cloth (~100cm x 15cm) were positioned as an “X” over the permanent monuments marking the center of the 5 field plots from Fettig et al. (2019).

For each of the 36 sites (containing 5 plots each), we captured imagery over the surrounding ~40 hectares of forested area using north-south aerial transects. For three sites, we surveyed less surrounding area in order to maintain visual and radio communication with the aircraft during flight which can be obstructed by rolling terrain or non-centrally

## CHAPTER 2. LOCAL STRUCTURE; WESTERN PINE BEETLE SEVERITY

available takeoff locations.

We preprogrammed aerial transects using Map Pilot for DJI on iOS flight software (hereafter Map Pilot) (DronesMadeEasy 2018). Using the Map Pilot software, we included an altitude adjustment along each aerial transect using a 1-arc-second digital elevation model (Farr et al. 2007) such that the aircraft’s altitude remained approximately constant at 120 meters above ground level in order to maintain consistent ground sampling distance (centimeters on the ground per pixel) in the imagery. Ground sampling distance was approximately 5 cm/px for the Zenmuse X3 RGB camera and approximately 8 cm/px for the RedEdge3 multispectral camera. For this analysis, we dropped 4 sites whose imagery was of insufficient quality to process.

Structure from motion (SfM) processing requires highly overlapping images, especially in densely vegetated areas (Frey et al. 2018). We planned transects with 90% forward overlap and 90% side overlap at 100 meters below the lens. Thus, with flights being at 120 meters above ground level, we achieved slightly higher than 90/90% overlap for objects under 20 meters tall (91.6/91.6% overlap at the ground). Overlap values were based on focal length (3.6mm), sensor width (6.2mm), and image dimension (4000x3000 pixels) parameters of the Zenmuse X3 camera. Images were captured at a constant rate of 1 image every 2 seconds for both cameras. A forward overlap of 90% at 100 meters translates to a flight speed of approximately 6.45 m/s and a side overlap of 90% at 100 meters translates to transects approximately 17.2 meters apart. The RedEdge3 camera has a different focal length (5.4mm), sensor width (4.8mm), and image dimension (1280x960 pixels), which translates to image overlap of 80.7/80.7 % at 100m below the lens and 83.9/83.9 % at ground level. Approximately 1900 photos were captured over each 40 hectare survey area for each camera.

## METHODS

### Structure from Motion (SfM) processing

We used structure from motion (SfM) to generate dense point clouds (Figure 2.2), digital surface models (Figure 2.3), and orthorectified reflectance maps (Figure 2.4) for each field site (Frey et al. 2018). We used Pix4Dmapper Cloud to process imagery using parameters ideal for images of a densely vegetated area taken by a multispectral camera. For 29 sites, we processed the RedEdge3 multispectral imagery alone. For three sites, we processed the RGB and the multispectral imagery in the same project to enhance the point density of the resulting point cloud. All SfM projects resulted in a single processing “block,” indicating that all images in the project were optimized and processed together.

### Creating canopy height models

We classified each survey area’s dense point cloud into “ground” and “non-ground” points using a cloth simulation filter algorithm (Zhang et al. 2016) implemented in the `lidR` (Roussel et al. 2019) package. We rasterized the ground points using the `raster` package (Hijmans et al. 2019) to create a digital terrain model (Figure 2.5) representing the ground underneath the vegetation at 1 meter resolution. We created a canopy height model (Figure 2.6) by subtracting the digital terrain model from the digital surface model created in Pix4Dmapper.

### Tree detection

We tested a total of 7 automatic tree detection algorithms and a total of 177 parameter sets on the canopy height model or the dense point cloud to locate trees within each

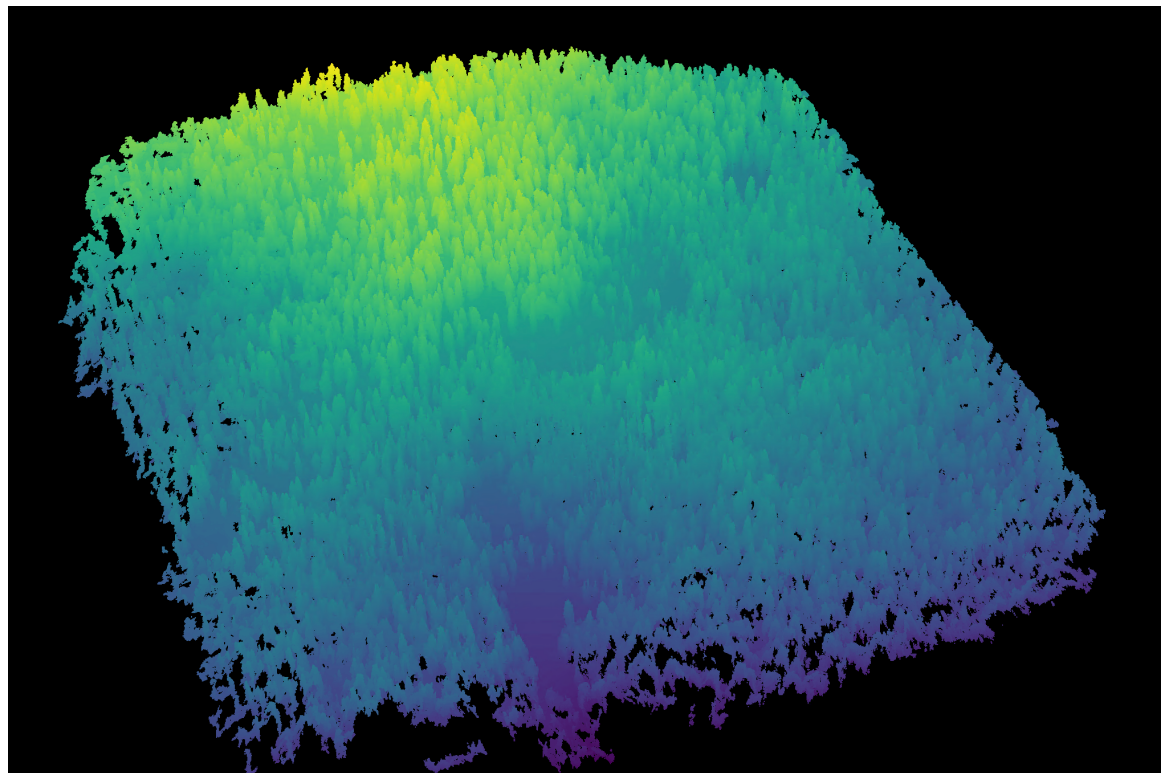


Figure 2.2: A dense point cloud representing ~40 hectares of forest is generated using Structure from Motion (SfM) processing of ~1900 images. The dense point cloud z- position represents the ground elevation plus the vegetation height.

## METHODS

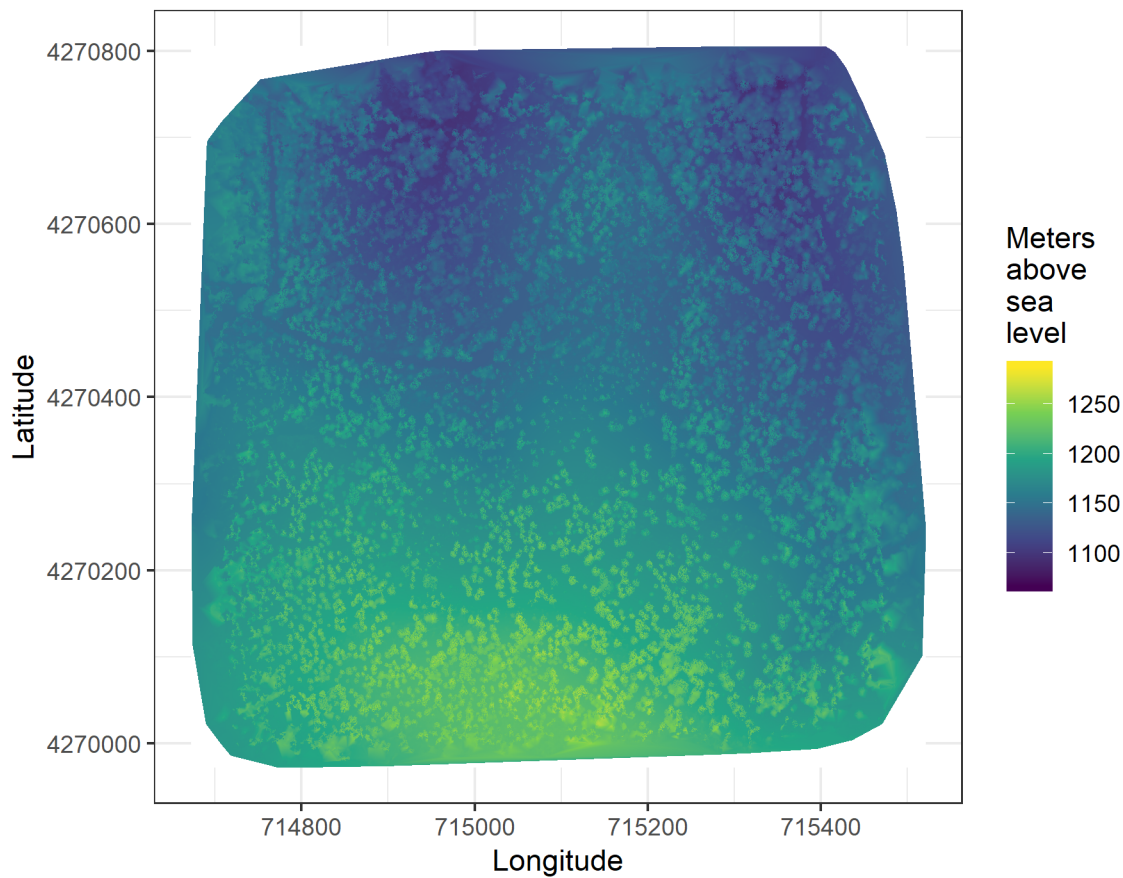


Figure 2.3: The digital surface model (DSM) is a 2-dimensional representation of the dense point cloud generated using structure from motion (SfM) processing. The DSM represents the ground elevation plus the vegetation height.

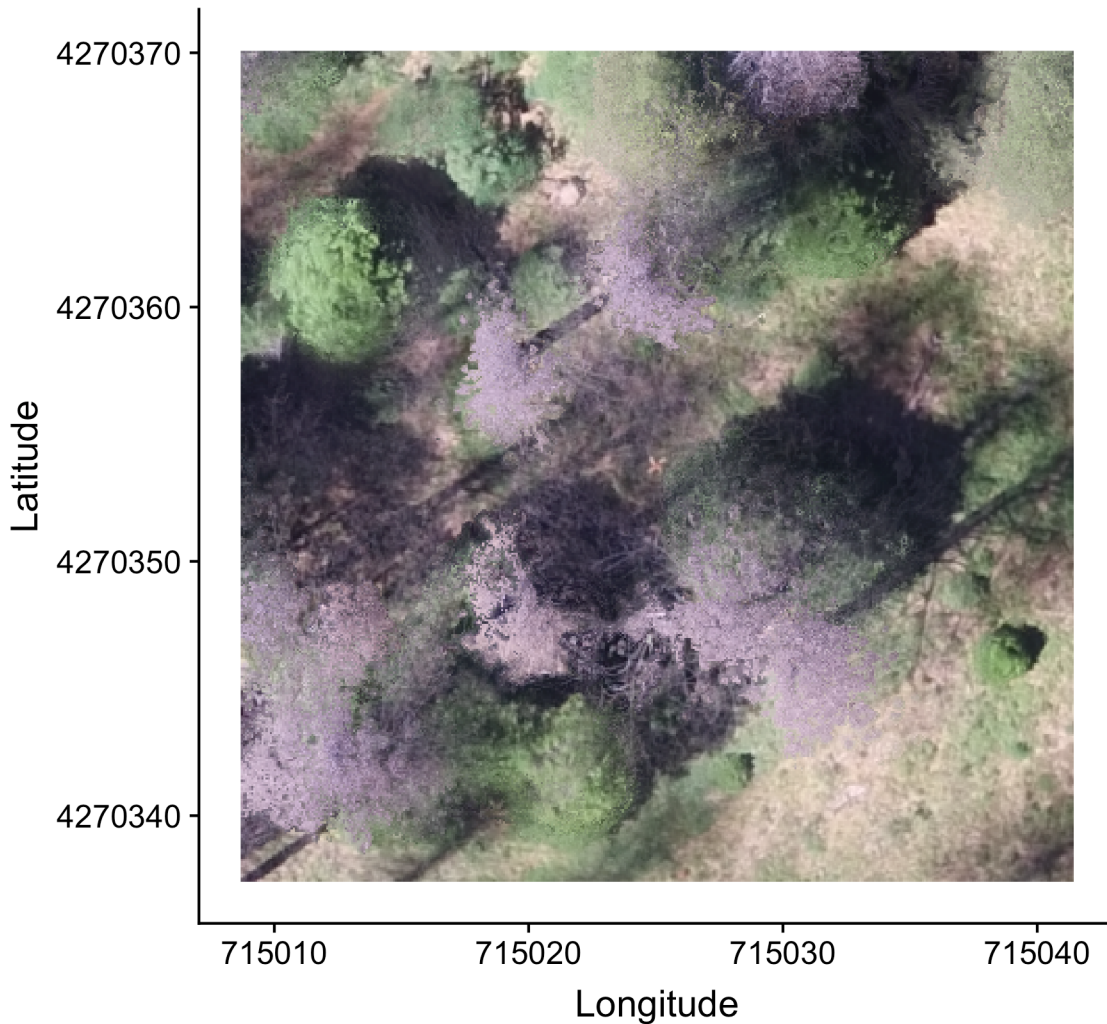


Figure 2.4: The orthomosaic for each of the 32 sites is generated with the Structure from Motion (SfM) processing, showing a top-down view of the whole survey area such that distances between objects in the scene are preserved and can be measured. Depicted is an example orthomosaic for one of the 32 sites cropped to the extent of a single ground plot (5 ground plots per site) showing the orange X placed at exactly the plot center prior to flight. The original orthomosaic for the whole site represents an area approximately 1000 times as large as the area depicted here.

## METHODS

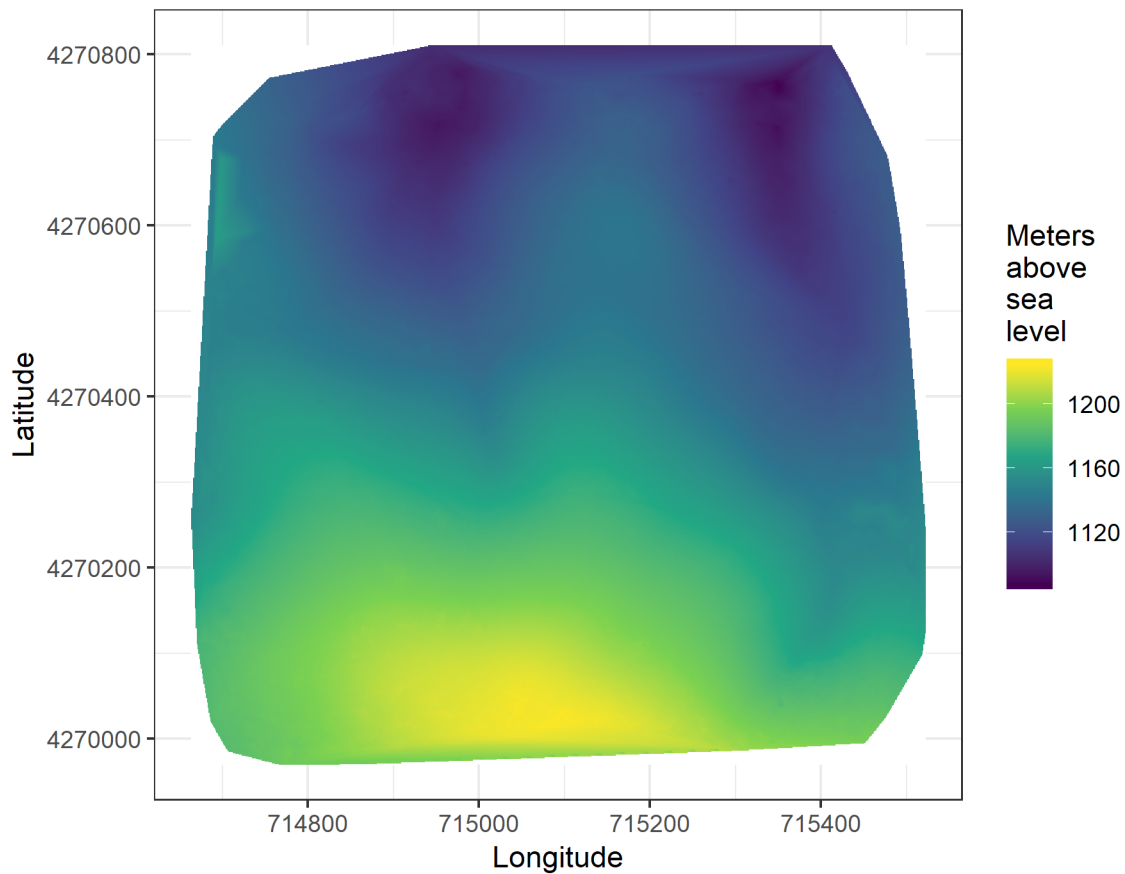


Figure 2.5: The digital terrain model (DTM) is generated by processing the dense point cloud using the cloth simulation filter algorithm (Zhang et al. 2016), which classifies points as ‘ground’ or ‘not-ground’ and then interpolates the ‘ground’ elevation using Delaunay triangulation for the rest of the dense point cloud footprint. The DTM represents the ground elevation without any vegetation.

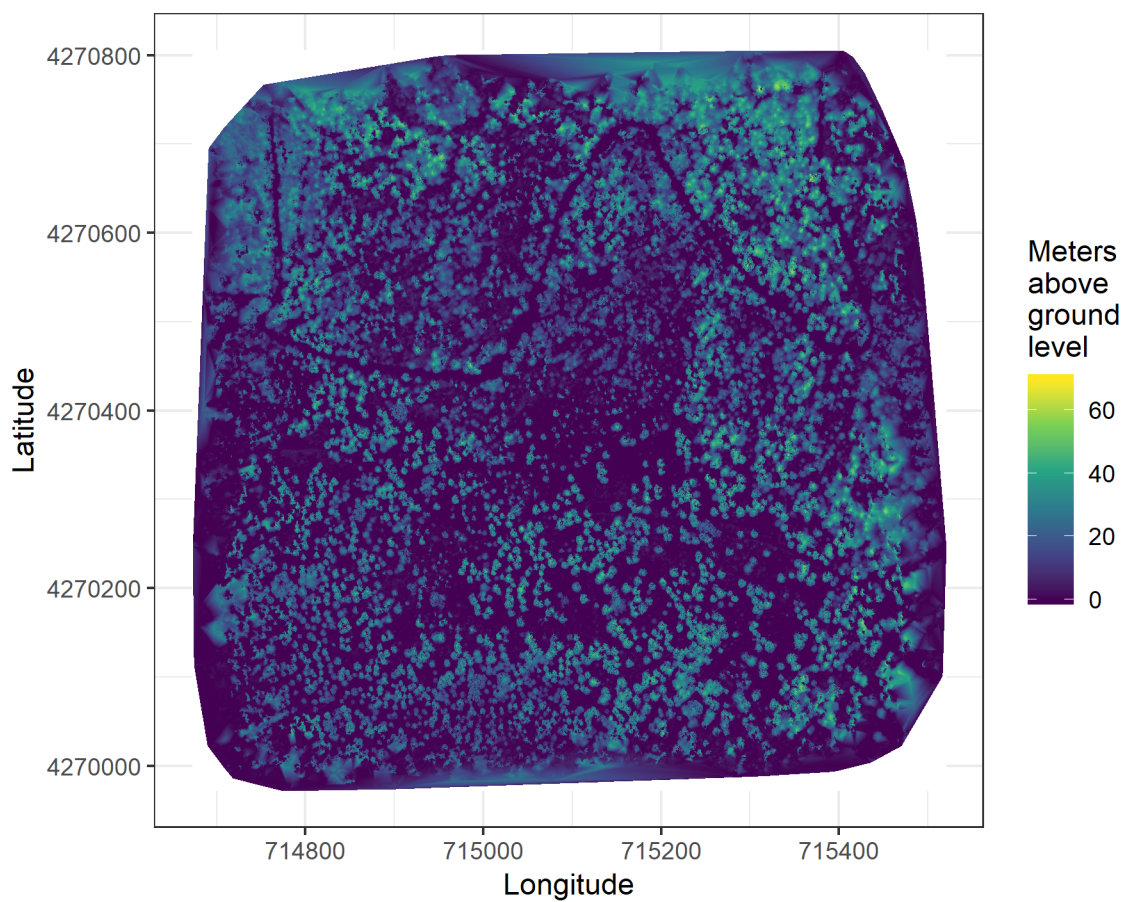


Figure 2.6: The canopy height model (CHM) is generated by subtracting the digital terrain model from the digital surface model. The CHM represents the height of all of the elevation above ground level.

## METHODS

site (Table 2.2). We used 3 parameter sets of a variable window filter using the `vwf()` function in the `ForestTools` (Plowright 2018) R package, including the default `winFun` parameter for the `vwf()` function as well as the “pines” and “combined” functions from Popescu and Wynne (2004) as the `winFun` parameter. We used 6 parameter sets of a local maximum filter implemented in `lidR`. We used 131 parameter sets of the algorithm from Li et al. (2012), which operates on the original point cloud. These parameter sets included those from Shin et al. (2018) and Jakubowski et al. (2013). We used 3 parameter sets of the `watershed` algorithm implemented in `lidR`, which is a wrapper for a function in the `EBImage` package (Pau et al. 2010). We used 3 parameter sets of `ptrees` (Vega et al. 2014) implemented in `lidR` (Roussel et al. 2019) and `lidRplugins` (Roussel 2019) and which operates on the raw point cloud, without first normalizing it to height above ground level (i.e.. subtracting the ground elevation from the dense point cloud). We used the default parameter set of the `multichm` (Eysn et al. 2015) algorithm implemented in `lidR` (Roussel et al. 2019) and `lidRplugins` (Roussel 2019). Finally, we used 30 parameter sets of the experimental algorithm `lmfx` (Roussel 2019).

Table 2.2: Algorithm name, number of parameter sets tested for each algorithm, and references.

---

Parameter sets		
Algorithm	tested	Reference(s)
li2012	131	Li et al. (2012); Jakubowski et al. (2013); Shin et al. (2018)
lmfx	30	Roussel (2019)
localMaxima	6	Roussel et al. (2019)
multichm	1	Eysn et al. (2015)

Parameter sets		
Algorithm	tested	Reference(s)
ptrees	3	Vega et al. (2014)
vwf	3	Plowright (2018)
watershed	3	Pau et al. (2010)

## Map ground data

Each orthorectified reflectance map was inspected to locate the 5 orange “X”s marking the center of the field plots (Figure 2.4), though some plot centers were obscured due to dense interlocking tree crowns or because a plot center was located directly under a single tree crown. We were able to locate 110 out of 180 field plots and were then able to use these plots for validation of automated tree detection algorithms. We used the `sf` package (Pebesma et al. 2019) to convert distance-from-center and azimuth measurements of each tree in the ground plots to an x-y position on the SfM-derived reflectance map using the x-y position of the orange X visible in the reflectance map as the center.

## Correspondence of automatic tree detection with ground data

We calculated 7 forest structure metrics for each field plot using the ground data collected by Fettig et al. (2019): total number of trees, number of trees greater than 15 meters, mean height of trees, 25<sup>th</sup> percentile tree height, 75<sup>th</sup> percentile tree height, mean distance to nearest tree neighbor, mean distance to 2<sup>nd</sup> nearest neighbor.

For each tree detection algorithm and parameter set described above, we calculated the same set of 7 structure metrics within the footprint of the validation field plots. We

## METHODS

calculated the Pearson’s correlation and root mean square error (RMSE) between the ground data and the aerial data for each of the 7 structure metrics for each of the 177 automatic tree detection algorithms/parameter sets.

For each algorithm and parameter set, we calculated its performance relative to other algorithms as whether its Pearson’s correlation was within 5% of the highest Pearson’s correlation as well as whether its RMSE was within 5% of the lowest RMSE. For each algorithm/parameter set, we summed the number of forest structure metrics for which it reached these 5% thresholds. For automatically detecting trees across the whole study, we selected the algorithm/parameter set that performed well across the most number of forest metrics (Figure 2.7).

## Segmentation of crowns

We delineated individual tree crowns with a marker controlled watershed segmentation algorithm (Meyer and Beucher 1990) using the detected treetops as markers implemented in the `ForestTools` package (Plowright 2018). If the automatic segmentation algorithm failed to generate a crown segment for a detected tree (e.g., often snags with a very small crown footprint), a circular crown was generated with a radius of 0.5 meters. If the segmentation generated multiple polygons for a single detected tree, only the polygon containing the detected tree was retained (Figure 2.8). Image overlap decreases near the edges of the overall flight path, which reduces the quality of the SfM processing in those areas. Thus, we excluded segmented crowns within 35 meters of the edge of the survey area. Given the narrower field of view of the RedEdge3 multispectral camera versus the X3 RGB camera whose optical parameters were used to define the ~40 hectare survey area around each site, as well as the 35 meter additional buffering, the survey area at each site was approximately 30 hectares (Table 2.3).

CHAPTER 2. LOCAL STRUCTURE; WESTERN PINE BEETLE SEVERITY

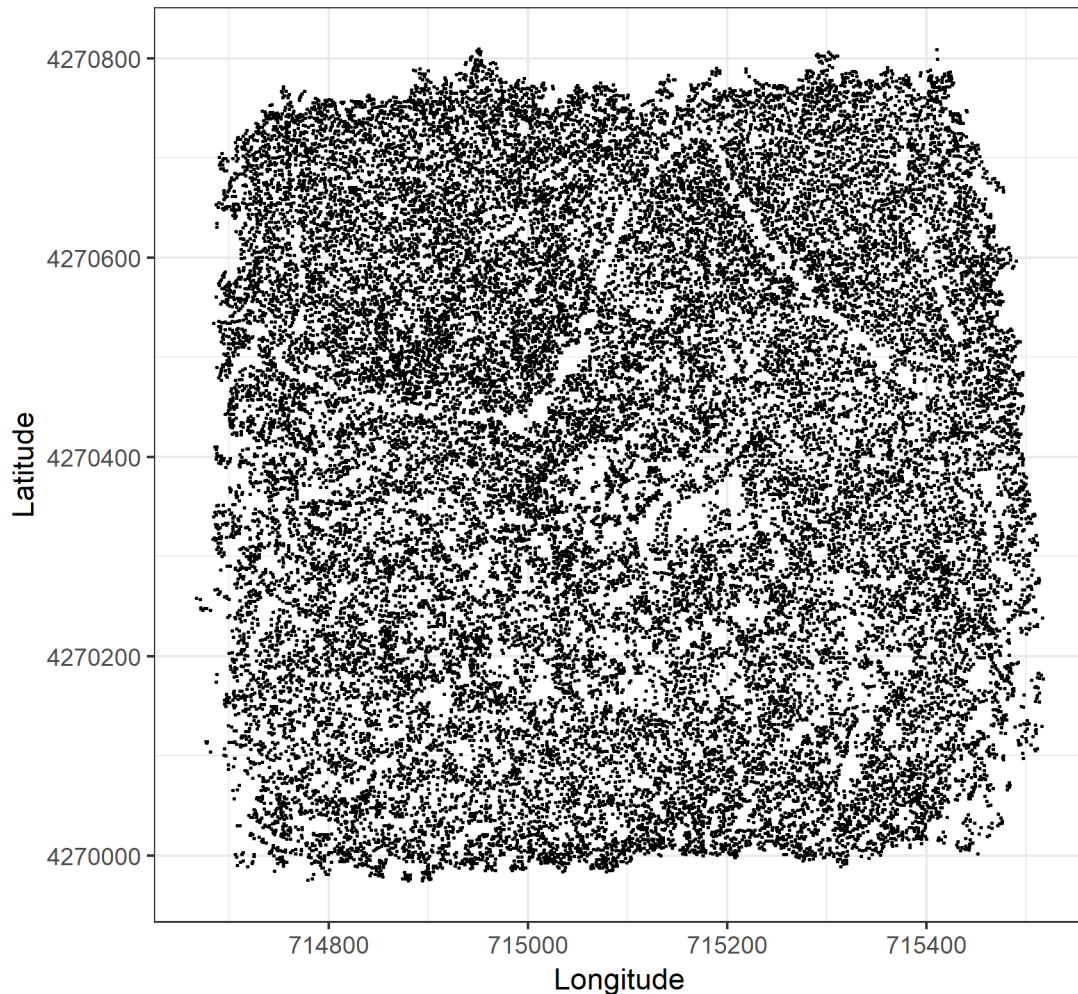


Figure 2.7: Tree locations are detected using the `lmfx` (Roussel et al. 2019) treetop detection algorithm on the dense point cloud.

## METHODS

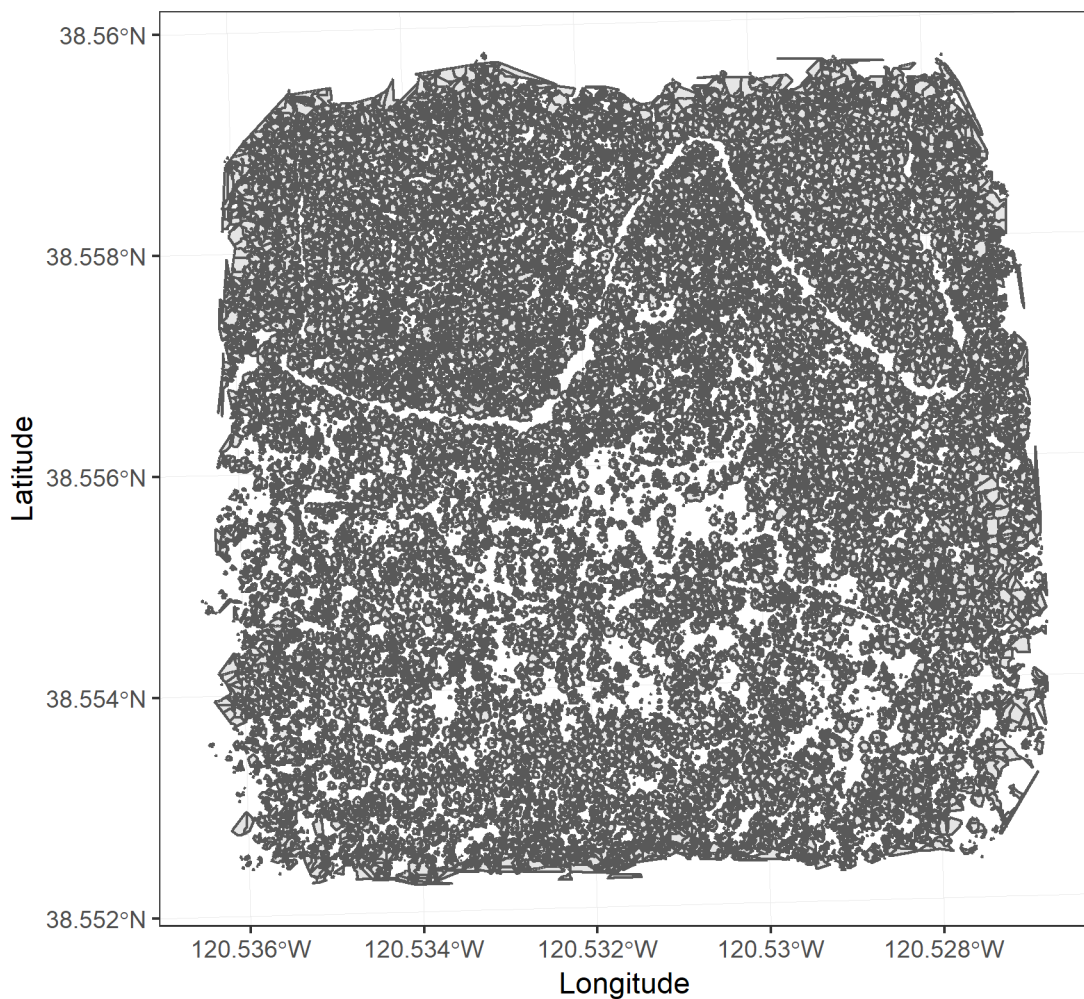


Figure 2.8: Individual crowns are delineated using a marker controlled watershed segmentation algorithm (Meyer and Beucher 1990, Plowright 2018) on the canopy height model (CHM) using the detected tree locations as a priority map. If the algorithm failed to delineate a crown for a tree that was identified in the tree detection step, a circular crown with a 0.5m buffer centered on point location of the detected tree was added as a crown.

## CHAPTER 2. LOCAL STRUCTURE; WESTERN PINE BEETLE SEVERITY

We used the `velox` package (Hunziker 2017) to extract all the pixel values from the orthorectified reflectance map for each of the 5 narrow bands within each segmented crown polygon. Per pixel, we additionally calculated the normalized difference vegetation index (NDVI; Rouse et al. (1973)), the normalized difference red edge (NDRE; Gitelson and Merzlyak (1994)), the red-green index (RGI; Coops et al. (2006)), the red edge chlorophyll index ( $CI_{red\ edge}$ ; Clevers and Gitelson (2013)), and the green chlorophyll index ( $CI_{green}$ ; Clevers and Gitelson (2013)). For each crown polygon, we calculated the mean value for each raw and derived reflectance band (5 raw; 5 derived).

## Classification of trees

We overlaid the segmented crowns on the reflectance maps from 20 sites spanning the latitudinal and elevation gradient in the study. Using QGIS, we hand classified 564 trees as live/dead (Figure 2.9) and as one of 5 dominant species in the study area (*Pinus ponderosa*, *Pinus lambertiana*, *Abies concolor*, *Calocedrus decurrens*, or *Quercus kelloggii*) using the mapped ground data as a guide. We treated all trees classified as ponderosa pine as a “host” tree and all other species as “non-host” trees (Figure 2.10).

We used all 10 mean values of the reflectance bands for each tree crown polygon to predict whether the hand classified trees were alive or dead using a boosted logistic regression model implemented in the `caret` package (accuracy of live/dead classification on a withheld test dataset: 97.3%) (Kuhn 2008). For just the living trees, we similarly used all 10 reflectance values to predict the tree species using regularized discriminant analysis implemented in the `caret` package (accuracy of species classification on a withheld testing dataset: 66.7%; accuracy of WPB host/non-WPB-host (i.e., ponderosa pine versus other tree species) on a withheld testing dataset: 74.4%).

Finally, we used these models to classify all tree crowns in the data set as alive or dead

## METHODS

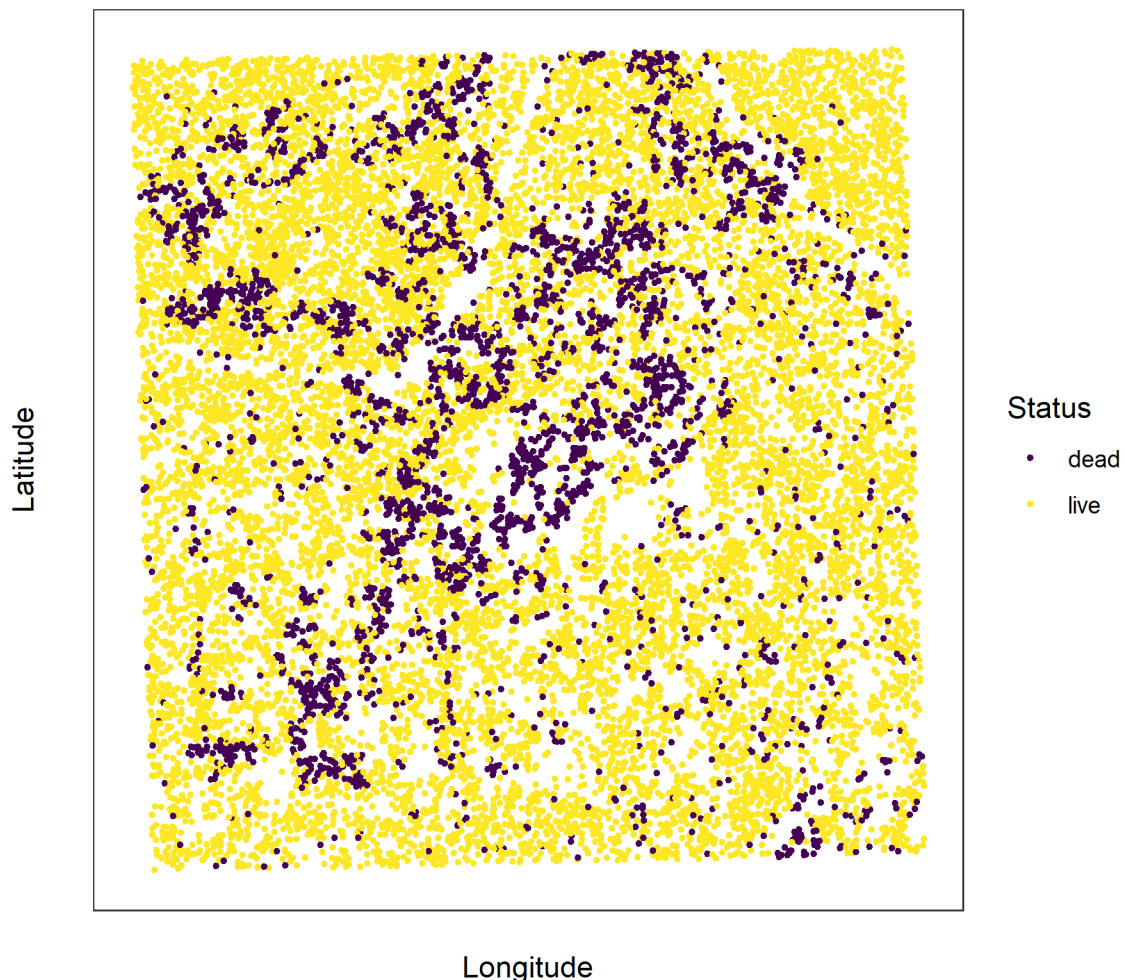


Figure 2.9: Each tree is classified as live or dead by extracting the pixel values from the 5 narrow bands of the Rededge3 camera (and 5 derived bands—see methods) in the orthomosaic within each segmented tree crown of the detected trees, taking their mean value, and using those means to predict live/dead status with a boosted logistic regression previously trained on a hand-classified set of segmented crowns from across the study area.

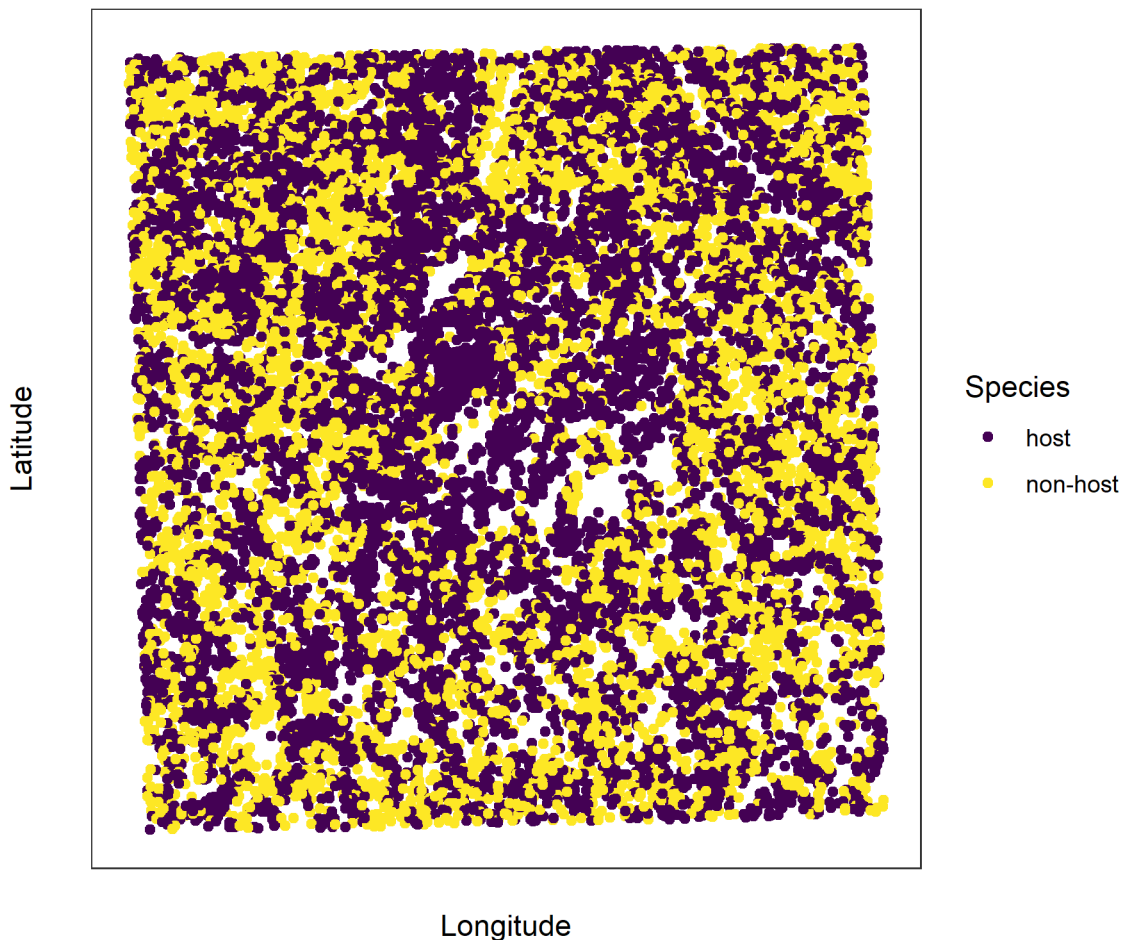


Figure 2.10: For each live tree, we classified its species using the same means of extracted pixel values across the 5 Rededge3 narrow bands (and 5 derived bands) as predictors in a regularized discriminant analysis previously trained on a hand-classified set of segmented crowns from across the study area.

## METHODS

as well as the species of living trees.

### Allometric scaling of height to quadratic mean diameter

We converted the height of each tree determined using the canopy height model to its diameter at breast height, 1.37m (DBH). Using the tree height and DBH ground data from Fettig et al. (2019), we fit a simple linear regression to predict DBH from height for each of the 5 dominant species. Using the model-classified tree species of each segmented tree, we used the corresponding linear relationship for that species to estimate the DBH given the tree's height. We then calculated the quadratic mean diameter for each 20m x 20m cell as the square root of the average squared diameter of trees within the cell.

### Note on assumptions about dead trees

For the purposes of this study, we assumed that all dead trees were ponderosa pine and were thus host trees for the western pine beetle. This is a reasonably good assumption for our study area, given that Fettig et al. (2019) found that 73.4% of the dead trees in the coincident ground plots were ponderosa pine. The species contributing to the next highest proportion of dead trees was incense cedar which represented 18.72% of the dead trees in the ground plots. Incense cedar is not a potential host of the western pine beetle, and different forest structure/environment conditions can dictate the dynamic between forest insects and their host tree species (Stephenson et al. 2019). While the detected mortality is most likely to be ponderosa pine, it is critical to interpret our results with this known limitation in mind.

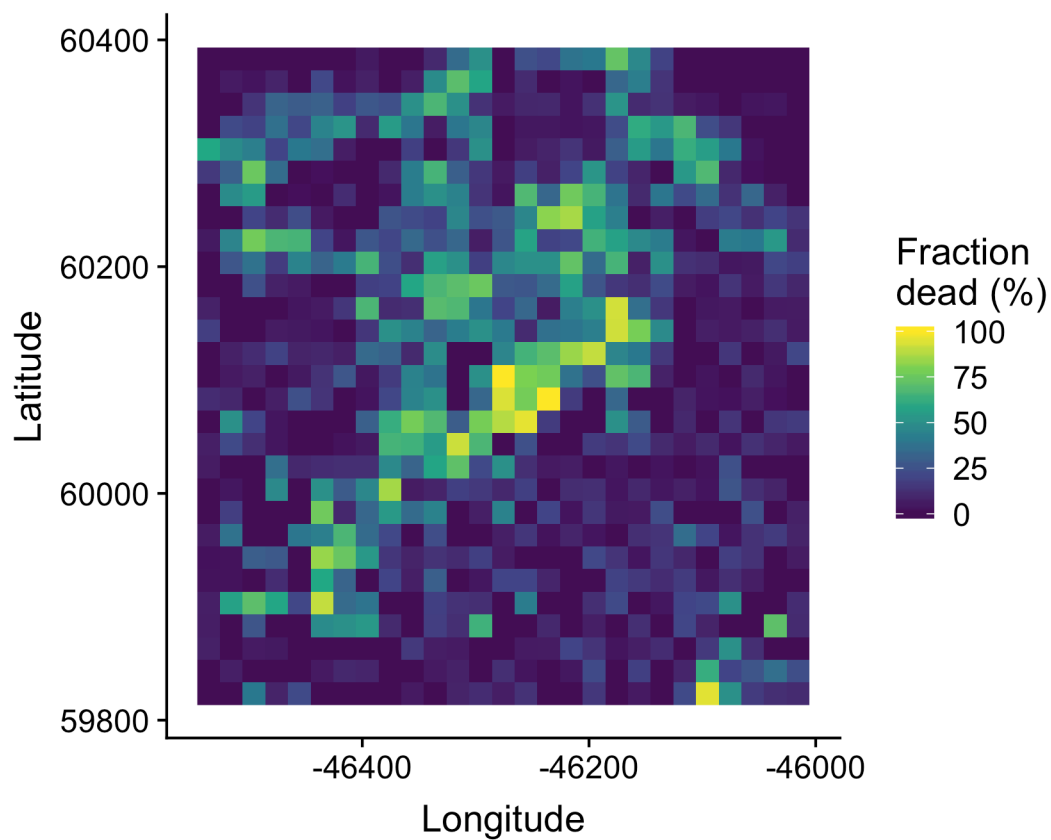


Figure 2.11: We rasterized the individual tree data by aggregating values to 20m x 20m cells. This example shows the proportion of dead trees per cell for the same example site as in the previous figures.

## METHODS

### Rasterizing individual tree data

Because the tree detection algorithms were validated against ground data at the plot level, we rasterized the classified trees at a spatial resolution similar to that of the ground plots (Figure 2.11). That is, we rasterized the individual tree data to 20m x 20m pixels equaling 400 m<sup>2</sup>, and the circular ground plots with 11.35m radius covered 404 m<sup>2</sup>. In each raster cell, we calculated the: number of live trees, number of dead trees, number of ponderosa pine trees, total number of trees (of all species, including ponderosa pine), quadratic mean diameter (QMD) of ponderosa pine trees, and QMD of all trees of any species (overall QMD). We converted the count of ponderosa pine trees and the total tree count to a density measurement of trees per hectare (tpha) by multiplying the counts in each 20m x 20m cell by 25 to create a “host density” and an “overall density” variable per cell.

### Environmental data

We used climatic water deficit (CWD) (Stephenson [1998](#)) from the 1981-2010 mean value of the basin characterization model (Flint et al. [2013](#)) as an integrated measure of temperature and moisture conditions for each of the 32 sites. Higher values of CWD correspond to hotter, drier conditions and lower values correspond to cooler, wetter conditions. CWD has been shown to correlate well with broad patterns of tree mortality in the Sierra Nevada (Young et al. [2017](#)) as well as bark beetle-induced tree mortality (Millar et al. [2012](#)). We converted the CWD value for each site into a z-score representing that site’s deviation from the mean CWD across the climatic range of Sierra Nevada ponderosa pine as determined from 179 herbarium records described in Baldwin et al. ([2017](#)). Thus, a CWD z-score of one would indicate that the CWD at that site is one

## CHAPTER 2. LOCAL STRUCTURE; WESTERN PINE BEETLE SEVERITY

standard deviation hotter/drier than the mean CWD across all geolocated herbarium records for ponderosa pine in the Sierra Nevada.

### Statistical model

We used a generalized linear model with a zero-inflated binomial response and a logit link to predict the probability of ponderosa pine mortality within each 20m x 20m cell as a function of the crossed effects of ponderosa pine quadratic mean diameter and density added to the crossed effect of quadratic mean diameter and density of trees of all species in each cell (hereafter “overall quadratic mean diameter” and “overall density”), as well as the interaction of each summand with climatic water deficit at each site.

To measure and account for spatial autocorrelation of the bark beetle behavioral processes underlying ponderosa pine mortality, we subsampled the data at each site to a random selection of 200, 20m x 20m cells representing approximately 27.5% of the surveyed area. With these subsampled data, we included a separate exact Gaussian process term per site of the interaction between the x- and y-position of each cell using the `gp()` function in the `brms` package (Bürkner 2017). The Gaussian process estimates the spatial covariance in the response variable (log-odds of ponderosa pine mortality) jointly with the effects of the other covariates.

## METHODS

$$y_{i,j} \sim \begin{cases} 0, & p \\ Binom(n_i, \pi_i), & 1 - p \end{cases}$$

$$\begin{aligned} logit(\pi_i) = & \beta_0 + \\ & \beta_1 X_{cwd,j} + \\ & \beta_1 X_{cwd,j} (\beta_2 X_{pipoQMD,i} + \beta_3 X_{pipoDensity,i} + \beta_4 X_{pipoQMD,i} X_{pipoDensity,i}) + \\ & \beta_1 X_{cwd,j} (\beta_5 X_{overallQMD,i} + \beta_6 X_{overallDensity,i} + \beta_7 X_{overallQMD,i} X_{overallDensity,i}) + \\ & \mathcal{GP}_j(x_i, y_i) \end{aligned}$$

Where  $y_i$  is the number of dead trees in cell  $i$ ,  $n_i$  is the sum of the dead trees (assumed to be ponderosa pine) and live ponderosa pine trees in cell  $i$ ,  $\pi_i$  is the probability of ponderosa pine tree mortality in cell  $i$ ,  $p$  is the probability of there being zero dead trees in a cell arising as a result of an unmodeled process,  $X_{cwd,j}$  is the z-score of climatic water deficit for site  $j$ ,  $X_{pipoQMD,i}$  is the scaled quadratic mean diameter of ponderosa pine in cell  $i$ ,  $X_{pipoDensity,i}$  is the scaled density of ponderosa pine trees in cell  $i$ ,  $X_{overallQMD,i}$  is the scaled quadratic mean diameter of all trees in cell  $i$ ,  $X_{overallDensity,i}$  is the scaled density of all trees in cell  $i$ ,  $x_i$  and  $y_i$  are the x- and y- coordinates of the centroid of the cell in an EPSG3310 coordinate reference system, and  $\mathcal{GP}_j$  represents the exact Gaussian process describing the spatial covariance between cells at site  $j$ .

We used 4 chains with 2000 iterations each (1000 warmup, 1000 samples), and confirmed chain convergence by ensuring all `Rhat` values were less than 1.1 (Brooks and Gelman 1998). We used posterior predictive checks to visually confirm model performance by overlaying the density curves of the predicted number of dead trees per cell over the observed number (Gabry et al. 2019). For the posterior predictive checks, we used 50

## CHAPTER 2. LOCAL STRUCTURE; WESTERN PINE BEETLE SEVERITY

random samples from the model fit to generate 50 density curves and ensured curves were centered on the observed distribution, paying special attention to model performance at capturing counts of zero.

### Software and data availability

All data are available via the Open Science Framework. Statistical analyses were performed using the `brms` packages. With the exception of the SfM software (Pix4Dmapper Cloud) and the GIS software QGIS, all data carpentry and analyses were performed using R (R Core Team 2018).

## Results

Table 2.3: Site characteristics for each of the 32 sites. The site name consists of the forest name, elevation band, and rep separated by an underscore. The Eldorado National Forest is ‘eldo’, the Stanislaus National Forest is ‘stan’, the Sierra National Forest is ‘sier’, and the Sequoia National Forest is ‘sequ’. The elevation band represents the lower bounds of the 305 meter (1000 foot) elevation bands in feet. Thus ‘3k’ implies that site was located between 3,000 and 4,000 feet (914-1219 meters). Aerially detected mortality and density of the whole site is presented along with the mortality and density calculated from the ground data (aerial / ground). The density is measured in trees per hectare (tpha).

Site	CWD (mm)	CWD (z-score)	Survey area (ha)	% tree	
				mortality (aerial/ground)	Density (tpha; aerial/ground)
eldo_3k_1	678	0.319	31.02	11/61	630/410
eldo_3k_2	706	0.501	30.61	12/36	444/647

## RESULTS

Site	(mm)	CWD	CWD	Survey	% tree	Density (tpha; aerial/ground)
		(z-score)	area (ha)	mortality (aerial/ground)		
eldo_3k_3	655	0.163	30.95	22/36	493/410	
eldo_4k_1	570	-0.383	28.04	9/39	633/588	
eldo_4k_2	642	0.0831	28.41	15/78	338/272	
eldo_5k_1	663	0.219	28.44	11/44	662/544	
eldo_5k_2	627	-0.0132	30.02	12/36	585/969	
eldo_5k_3	599	-0.2	29.73	7/32	489/623	
stan_3k_1	638	0.059	31.04	10/52	739/1038	
stan_3k_2	739	0.713	18.78	40/78	434/405	
stan_3k_3	762	0.859	30.1	22/41	558/326	
stan_4k_1	540	-0.58	29.62	29/63	508/712	
stan_4k_2	528	-0.658	30.54	18/56	482/257	
stan_5k_1	524	-0.688	30.94	19/54	389/336	
stan_5k_2	524	-0.685	29.94	21/44	399/623	
sier_3k_1	764	0.871	30.42	19/48	651/850	
sier_3k_2	768	0.898	30.05	20/77	439/153	
sier_3k_3	773	0.932	29.77	32/77	511/460	
sier_4k_1	841	1.38	30.43	54/51	576/539	
sier_4k_2	764	0.877	29.3	33/57	499/855	
sier_4k_3	688	0.383	26.39	48/59	454/499	
sier_5k_1	722	0.599	14.59	41/43	631/717	
sier_5k_2	710	0.523	27.53	53/74	477/455	
sier_5k_3	779	0.968	28.93	33/43	569/484	

Site	CWD (mm)	CWD (z-score)	Survey area (ha)	% tree	
				mortality (aerial/ground)	Density (tpha; aerial/ground)
sequ_4k_1	767	0.891	29.59	50/56	366/608
sequ_4k_3	816	1.21	29.69	35/71	433/306
sequ_5k_1	718	0.577	27.12	35/52	364/445
sequ_5k_2	587	-0.274	29.1	45/43	478/499
sequ_5k_3	611	-0.117	31.34	42/48	349/494
sequ_6k_1	731	0.657	27.78	30/70	433/361
sequ_6k_2	690	0.39	11.83	26/43	699/934
sequ_6k_3	603	-0.174	26.51	36/32	536/692

## Tree detection

We found that the experimental `lmpfx` algorithm with parameter values of `dist2d = 1` and `ws = 2.5` (Roussel et al. 2019) performed the best across 7 measures of forest structure as measured by Pearson's correlation with ground data (Table 2.4).

## RESULTS

Table 2.4: Correlation and differences between the best performing tree detection algorithm (lmfx with dist2d = 1 and ws = 2.5) and the ground data. An asterisk next to the correlation or RMSE indicates that this value was within 5% of the value of the best-performing algorithm/parameter set. Ground mean represents the mean value of the forest metric across the 110 ground plots that were visible from the sUAS-derived imagery. The median error is calculated as the median of the differences between the air and ground values for the 110 visible plots. Thus, a positive number indicates an overestimate by the sUAS workflow and a negative number indicates an underestimate.

Forest structure metric	Ground	Correlation with		Median
	mean	ground	RMSE	error
total tree count	19	0.67*	8.68*	2
count of trees > 15m	9.9	0.43	7.38	0
distance to 1st neighbor	2.8	0.55*	1.16*	0.26
(m)				
distance to 2nd neighbor (m)	4.3	0.61*	1.70*	0.12
height (m); 25th percentile	12	0.16	8.46	-1.2
height (m); mean	18	0.29	7.81*	-2.3
height (m); 75th percentile	25	0.35	10.33*	-4

## Effect of local structure and regional climate on western pine beetle severity

We detected a small, generally positive main effect of climatic water deficit on the probability of ponderosa pine mortality within each 20m x 20m cell (Figure 2.12).

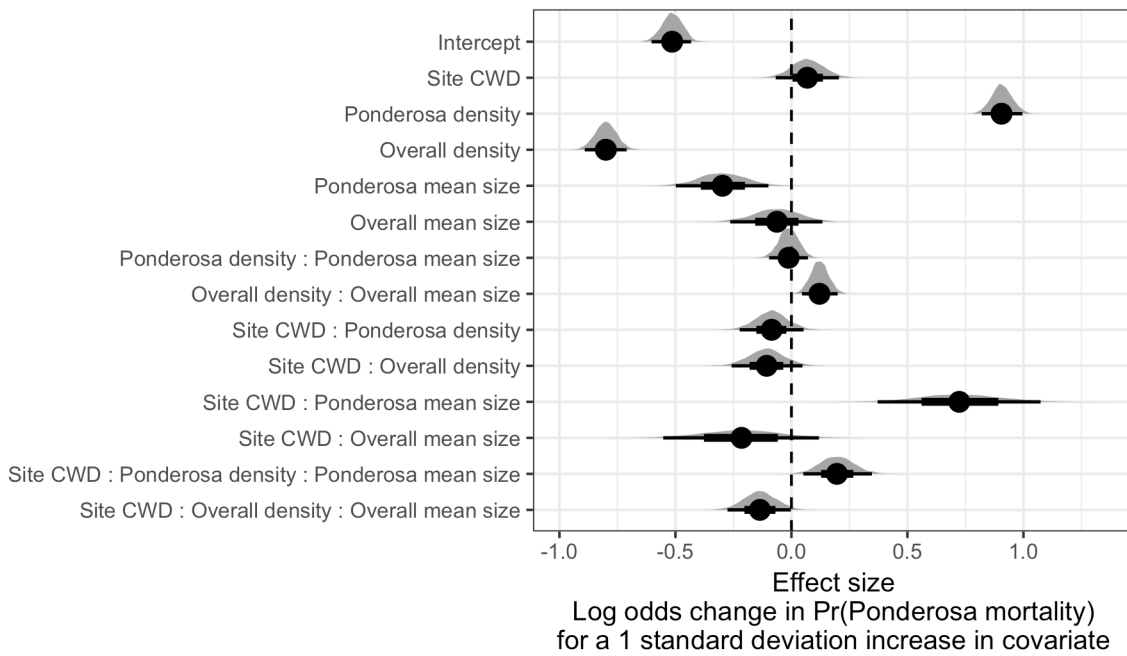


Figure 2.12: Posterior distributions of effect size from zero-inflated binomial model predicting the probability of ponderosa pine mortality in a 20m x 20m cell given forest structure characteristics of host trees and all trees within the cell, as well as a site-level climatic water deficit. The gray density distribution for each model covariate represents the density of the posterior distribution, the point underneath each density curve represents the median of the estimate, the bold interval surrounding the point estimate represents the 66% credible interval, and the thin interval surrounding the point estimate represents the 95% credible interval.

## **DISCUSSION**

We found a strongly positive main effect of ponderosa pine local density, with greater density increasing the probability of ponderosa pine mortality. Conversely, we found a strong negative effect of overall tree density (i.e., including both ponderosa pine and non-host species) such that additional non-host trees in a 20m x 20m cell (for the same number of host trees) would decrease the probability of ponderosa pine mortality (Figure 2.12).

We found a generally negative effect of quadratic mean diameter of ponderosa pine on the probability of ponderosa mortality, suggesting that the western pine beetle attacked smaller trees, on average. There was a strong positive interaction between the climatic water deficit and ponderosa pine quadratic mean diameter, such that larger trees were more likely to increase the probability of ponderosa mortality in hotter, drier sites (Figure 2.13).

There was a positive interaction between overall tree density and overall quadratic mean diameter, such that denser stands with larger trees did lead to greater ponderosa pine mortality, though the main effects of each of these variables were weakly negative (Figure 2.12).

## **Discussion**

We found that host tree density is a dominant driver of host mortality during elevated levels of bark beetle activity, likely due to energy costs associated with beetles navigating forests with many non-hosts available. We also found that, even within a single forest insect/tree species pairing, in the same extreme drought, and conditional upon high levels of western pine beetle activity, host tree size may still strongly affect insect-induced tree mortality in different ways depending on background environmental conditions of water

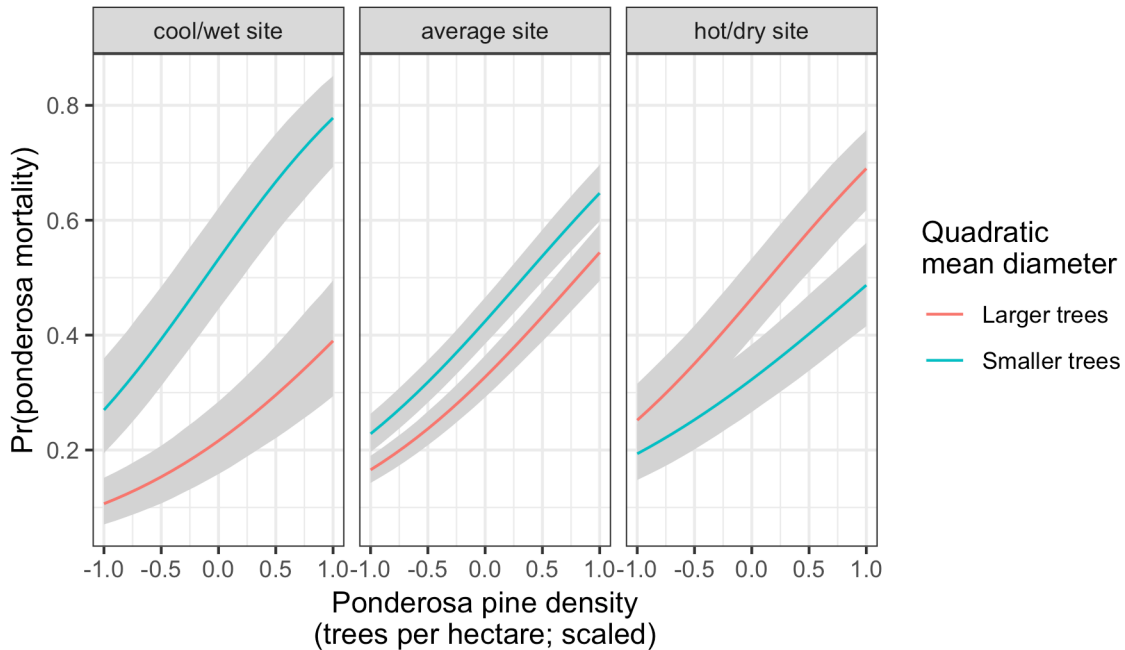


Figure 2.13: Line version of model results with 95% credible intervals showing primary influence of ponderosa pine structure on the probability of ponderosa pine mortality, and the interaction across climatic water deficit. The ‘larger trees’ line represents the quadratic mean diameter of ponderosa pine 0.7 standard deviations above the mean, and the ‘smaller trees’ line represents the quadratic mean diameter of ponderosa pine 0.7 standard deviations below the mean.

## **DISCUSSION**

stress. We suggest that this may indicate different stages of bark beetle disturbance throughout the Sierra yellow pine/mixed-conifer system, with “outbreak” thresholds surpassed at the hottest, driest sites where larger trees led to more likely host mortality, but not yet surpassed in cooler, wetter sites, where smaller trees led to more likely host mortality.

## **Broad-scale environmental condition**

We were surprised to only find a weakly positive main effect of climatic water deficit on the probability of ponderosa mortality, though an effect did materialize through its interaction with forest structure. We did not measure tree water stress at an individual tree level as in other recent work (Stephenson et al. 2019), and were instead treating climatic water deficit as a general indicator of tree stress following results of coarser-scale studies (Asner et al. 2016, Young et al. 2017) which may have contributed to our failure to detect a strong effect. Also, our entire study area experienced the same extreme hot drought between 2012 and 2015 and the variation of mortality explained by a main effect of climatic water deficit may be dampened when most trees are experiencing a high degree of water stress (Floyd et al. 2009, Fettig et al. 2019).

## **Strength of support for different “density increases mortality” hypotheses**

The strongest effect on the probability of host mortality was the local host density within each 20m x 20m cell. Host availability has been shown to have a strong influence on the prevalence of host mortality (Raffa and Berryman 1987). This can arise as beetles require shorter flights to disperse to new hosts and beetles are less likely to land on a

## CHAPTER 2. LOCAL STRUCTURE; WESTERN PINE BEETLE SEVERITY

non-host tree which imposes a “sunk cost” of energy expenditure in getting to that tree. Reduced dispersal distances to host trees likely favors successful bark beetle attacks, but we calibrated our aerial tree detection to  $\sim 400 \text{ m}^2$  areas rather than to individual tree locations so don’t have the data precision to address this hypothesis directly. Because we also found a strong negative effect of overall tree density (host plus non-host) within each cell while accounting for host density, we suspect that the positive association between host density and host mortality might be driven by increasing the frequency that western pine beetles land on their preferred host and avoid expending energy flying to non-hosts. The negative relationship that we detected between overall tree density and host mortality corroborates findings from Fettig et al. (2019) and perhaps the “sunk cost” of landing on non-hosts explains those findings, though Fettig et al. (2019) didn’t simultaneously model the effect of host density. In general, Hayes et al. (2009) and Fettig et al. (2019) found that measures of host availability explained less variation in mortality than measures of overall tree density, but those conclusions were based on a response variable of “total number of dead host trees,” rather than the number of dead host trees conditional on the total number of host trees as in our study (i.e., a binomial response).

Counter to our expectations, we found an overall negative effect of host tree mean size on the probability of host mortality. Generally, smaller trees are easier for western pine beetles to overwhelm in a mass attack and are prime targets under normal levels of tree water stress. However, larger trees are more nutritious and are therefore ideal targets if local bark beetle density is high enough to successfully initiate mass attack as can occur when many trees are under severe water stress (Bentz et al. 2010). In the recent hot drought, we expected that most trees would be under severe water stress, setting the stage for increasing beetle density, successful mass attacks, and targeting of larger trees. Larger average tree size in this case would therefore lead to greater ponderosa pine

## DISCUSSION

mortality, as was found in coincident ground plots (Fettig et al. 2019) and other studies (Stephenson et al. 2019, Pile et al. 2019). One possible explanation for our finding is that our observations represent the cumulative mortality of trees during a multi-year drought event and its aftermath. Lower host tree mean size led to a greater probability of host mortality earlier in the drought (Pile et al. 2019) and that signal might have persisted even as mortality continued to accumulate driven by other factors.

We did find a clear host tree size effect in its interaction with the climatic water deficit. In hot, dry sites, larger average host size increased the probability of host mortality while smaller host sizes increased the probability of host mortality in cool, wet sites. This suggests that the same bark beetle species was cueing into different aspects of forest structure across the environmental gradient. This represents an intraspecific version of the results of Stephenson et al. (2019), who found that insect-induced tree mortality in the same region during the same hot drought were driven by different factors for different tree species. For instance, Stephenson et al. (2019) found that ponderosa pine mortality was largely driven by host selection behavior of forest insects, where larger more nutritious trees were specifically targeted regardless of whether they exhibited signs of stress. In contrast, Stephenson et al. (2019) found that white fir mortality occurred predominantly in the slower growing, smaller, stressed trees. In our study, we found that, even within a single pairing of forest insect species and its host, the host tree size affected host mortality differently depending on the site-level climatic water deficit.

For aggressive bark beetles, massive tree mortality as observed from the 2012-2015 drought and its aftermath does not necessarily distinguish “endemic” from “outbreak” phases of bark beetle disturbance, which is instead distinguished by the underlying driver of bark beetle host selection behavior (Logan et al. 1998). “Endemic” phases are distinguished by environmental determinism, when beetles select hosts based on whether they

## CHAPTER 2. LOCAL STRUCTURE; WESTERN PINE BEETLE SEVERITY

are weakened in some way, often by environmental conditions. “Outbreak” phases are distinguished by dynamic determinism, when population dynamics reign—when local beetle density is high enough that intraspecific pheromone communication dominates host selection, successful mass attacks are likely, and even large healthy trees can be killed (White and Powell 1997, Logan et al. 1998). Despite high local levels of tree mortality across our study area (Fettig et al. 2019), our results from surveying the broader context surrounding coincident ground plots reveals different effects of host tree size depending on the climatic water deficit, and perhaps different stages of bark beetle disturbance across the environmental gradient. This may help explain the especially high host mortality in high host density, low host size cells that we observed in cool/wet sites (Figure 2.13). The smaller trees would presumably be nutritionally sub-optimal, and thus unexpected targets if the western pine beetle were indeed in an “outbreak” phase at these sites and able to attack even large, healthy trees. While trees were likely water stressed across the whole study due to the extreme drought, we expected generally less water stress in the cool/wet sites, and generally higher water stress in the hot/dry sites (Asner et al. 2016, Young et al. 2017). Thus, it is possible that the observed mortality patterns across the Sierra Nevada during the 2012-2015 hot drought arose as synergistic alignment of environmental conditions and complex forest structure enabled the western pine beetle to cross thresholds of “outbreak” behavior in the hottest, driest sites but such an alignment was not present in the cooler, wetter sites (Raffa et al. 2008).

## Limitations and future directions

We have demonstrated that drones can be effective means of collecting data at multiple, vastly different spatial scales to investigate a single, multi-scale phenomenon— from meters in between trees, to hundreds of meters of elevation, to hundreds of thousands of meters of

## DISCUSSION

latitude. However, some limitations remain but could perhaps be overcome with further refinements in the use of this tool for forest ecology. Most of these limitations arise from tree detection and classification uncertainty, and thus it was imperative to work with field data for calibration and uncertainty reporting.

The greatest limitation in our study arising from classification uncertainty is in the assumption that all dead trees were ponderosa pine. We estimate from coincident ground plots that this is true approximately 73.4% of the time. Because tree mortality response to forest insects is species-specific, even with sympatric tree species during the same hot drought (Stephenson et al. 2019), we cannot entirely rule out that some of the mortality responses to complex forest structure that we observed arose from these species-specific responses. The overall community composition across our study area was not very different (Fettig et al. 2019), so we remain confident that the patterns we observed were driven primarily by the dynamic between the western pine beetle and ponderosa pine.

Our ability to detect trees using the geometry of the dense point clouds derived with the SfM was also limited. The horizontal accuracy of the tree detection was better than the vertical accuracy, which may result from a more significant error contribution by the ground-based calculations of tree height compared to tree position relative to plot center (Table 2.4). Both the horizontal and vertical accuracy would likely improve with better SfM point clouds, which requires imagery with more overlap. Frey et al. (2018) recently found that 95% overlap was preferable for generating dense point clouds, and we only achieved 91.6% overlap with the X3 RGB camera and 83.9% overlap with the multispectral camera. While our live/dead classification was fairly accurate (97.3% on a withheld dataset), our species classifier would likely benefit from better crown segmentation because the pixel-level reflectance values within each crown are averaged to characterize the

## CHAPTER 2. LOCAL STRUCTURE; WESTERN PINE BEETLE SEVERITY

“spectral signature” of each tree. With better delineation of each tree crown, the mean value of pixels within each tree crown will likely be more representative of that tree’s spectral signature. Better crown segmentation would most readily be achieved through greater overlap in imagery. Finally, we anticipate that computer vision and deep learning will prove helpful in overcoming some of these detection and classification challenges (Gray et al. 2019).

## Conclusions

Climate change adaptation strategies emphasize reducing tree densities to restore forest resilience (North et al. 2015, Young et al. 2017), but understanding the optimal complex forest structure that can enable dry western U.S. forests to persist through disturbances such as insect attack will be vital for predicting how California forests may respond to these interventions. We’ve shown that drones can be a valuable tool for investigating how this complexity in forest structure combines with environmental conditions to shape forest insect disturbance.

Our results support conclusions of other researchers that management interventions to reduce the severity of bark beetle disturbance will benefit from generally reducing tree density (Young et al. 2017). However, in addition, our study suggests that outcomes will depend on whether the disturbance dynamic has crossed endemic to outbreak feedback thresholds (Raffa et al. 2008), which may be predicted by recent advances in disturbance forecasting (Preisler et al. 2017).

## *ACKNOWLEDGEMENTS*

### **Acknowledgements**

We gratefully acknowledge funding from the US Forest Service Western Wildlands Environmental Threat Assessment Center (WWETAC) as well as Connie Millar for comments and guidance during the development of this project.

# Appendix: Supplemental Information for ‘Chapter 1: Remote sensing resistance’

## Supplemental methods

Normalized difference vegetation index (NDVI; Supplemental Equation 4.1) correlates with vegetation density, canopy cover, and leaf area index (Rouse et al. 1973). Normalized difference moisture index (NDMI; Supplemental Equation 4.2) correlates with similar vegetation characteristics as NDVI, but doesn’t saturate at high levels of foliar biomass (Gao 1996, Huesca et al. (2016)). Normalized burn ratio (NBR; Supplemental Equation 4.3) and normalized burn ratio version 2 (NBR2; Supplemental Equation 4.4) respond strongly to fire effects on vegetation (García and Caselles 1991, Key and Benson 2006, USGS 2017a, 2017b, Hawbaker et al. 2017).

Supplemental Equation 4.1:  $ndvi = (nir - red)/(nir + red)$

Supplemental Equation 4.2:  $ndmi = (nir - swir1)/(nir + swir1)$

Supplemental Equation 4.3:  $nbr = (nir - swir2)/(nir + swir2)$

## SUPPLEMENTAL METHODS

Supplemental Equation 4.4:  $nbr2 = (swir1 - swir2)/(swir1 + swir2)$

Where *nir* is the near infrared band (band 4 on Landsat 4, 5, and 7; band 5 on Landsat 8) and *red* is the red band (band 3 on Landsat 4, 5, and 7; band 4 on Landsat 8), *swir1* is the first short wave infrared band (band 5 on Landsat 4, 5, and 7; band 4 on Landsat 8), *swir2* is the second short wave infrared band (band 7 on Landsat 4, 5, 7, and 8)

We calculated the delta severity indices (dNBR, dNBR2, dNDVI) by subtracting the respective postfire indices from the prefire indices (NBR, NBR2, and NDVI) without multiplying by a rescaling constant (e.g., we did not multiply the result by 1000 as in Miller and Thode (2007); Supplemental Equation 4.5). Following Reilly et al. (2017), we chose not to correct the delta indices using a phenological offset value (typically calculated as the delta index in homogeneous forest patch outside of the fire perimeter), as our approach implicitly accounts for phenology by incorporating multiple cloud-free images across the same time window both before the fire and one year later.

Supplemental Equation 4.5:  $dI = I_{\text{prefire}} - I_{\text{postfire}}$

We calculated the relative delta severity indices, RdNBR and RdNDVI, by scaling the respective delta indices (dNBR and dNDVI) from Supplemental Equation 4.6 by a square root transformation of the absolute value of the prefire index.

Supplemental Equation 4.6:  $RdI = \frac{dI}{\sqrt{\text{abs}(I_{\text{prefire}})}}$

We calculated the relative burn ratio (RBR) following Parks et al. (2014) using Supplemental Equation 4.7.

Supplemental Equation 4.7:  $RBR = \frac{dNBR}{NBR_{\text{prefire}} + 1.001}$

We used the digital elevation model to calculate the potential annual heat load (Supplemental Equation 4.8 at each pixel, which is an integrated measure of latitude, slope, and a folding transformation of aspect about the northeast-southwest line, such that north-

## CHAPTER 2. SUPPLEMENTARY INFORMATION FOR CHAPTER 1

east becomes 0 radians and southwest becomes  $\pi$  radians (McCune and Keon 2002, with correction in McCune 2007).

Supplemental Equation 4.8:

$$\begin{aligned} aspect_{folded} &= \text{abs}(\pi - \text{abs}(aspect - \frac{5\pi}{4})) \\ &- 1.467 + \\ &1.582 * \cos(latitude) \cos(slope) - \\ log(pahl) &= 1.5 * \cos(aspect_{folded}) \sin(slope) \sin(latitude) - \\ &0.262 * \sin(lat) \sin(slope) + \\ &0.607 * \sin(aspect_{folded}) \sin(slope) \end{aligned}$$

Where  $pahl$  is the potential annual heat load,  $aspect_{folded}$  is a transformation of aspect in radians, and both  $latitude$  and  $slope$  are extracted from a digital elevation model with units of radians.

## Supplemental figures and tables

## SUPPLEMENTAL FIGURES AND TABLES

Table 2.5: Comparison of models used to validate and calibrate remotely sensed wildfire severity with ground-based composite burn index (CBI) severity sorted in descending order by the  $R^2$  value from a 5-fold cross validation. A total of 56 models were tested representing all possible combinations of 7 different measures of wildfire severity (RBR, dNBR, dNBR2, RdNBR, RdNBR2, dNDVI, and RdNDVI), 4 different time windows in which Landsat imagery was acquired and summarized with a median reducer on a pixel-by-pixel basis (16 days, 32 days, 48 days, and 64 days), and two different interpolation methods (bilinear and bicubic). The three parameters ( $\beta_0$ ,  $\beta_1$ , and  $\beta_2$ ) from the nonlinear model fit described in Eq. 1 are reported. For each model, the value of the remotely sensed wildfire severity measurement corresponding to the lower bounds of 3 commonly used categories of severity are reported ('low' corresponds to a CBI value of 0.1, 'mod' corresponds to a CBI value of 1.25, and 'high' corresponds to a CBI value of 2.25)

Rank	Severity measure	Interp-		Time window	$R^2$	$\beta_0$	$\beta_1$	$\beta_2$	k-fold		
		olation	lation						low	mod	high
1	RBR	bicubic	48	48	0.82	0.014	0.028	1.001	0.045	0.113	0.282
2	RdNBR	bilinear	32	32	0.813	-0.483	3.061	0.857	2.852	8.45	20.56
3	RdNDVI	bilinear	48	48	0.809	-2.144	3.273	0.609	1.335	4.867	10.75
4	RBR	bilinear	32	32	0.807	0.014	0.029	0.985	0.046	0.113	0.28
5	RdNDVI	bicubic	64	64	0.805	-2.524	3.57	0.59	1.263	4.936	10.93
6	RBR	bicubic	64	64	0.805	0.016	0.027	1.01	0.046	0.113	0.283
7	RdNDVI	bicubic	32	32	0.803	-2.737	3.308	0.619	0.782	4.436	10.59
8	RBR	bilinear	64	64	0.802	0.017	0.027	1.003	0.047	0.113	0.279
9	RdNDVI	bilinear	32	32	0.801	-2.531	3.176	0.624	0.849	4.393	10.39
10	RdNDVI	bicubic	48	48	0.797	-2.623	3.624	0.587	1.22	4.922	10.94
11	RdNDVI	bilinear	64	64	0.796	-2.14	3.287	0.607	1.353	4.876	10.73
12	RdNBR	bilinear	64	64	0.792	-0.42	3.031	0.862	2.884	8.483	20.66
13	RBR	bilinear	48	48	0.791	0.017	0.027	1.006	0.047	0.112	0.277

**CHAPTER 2. SUPPLEMENTARY INFORMATION FOR CHAPTER 1**

---

Rank	Severity	Interp-									
		Time		k-fold							
		olation	window	R <sup>2</sup>	β <sub>0</sub>	β <sub>1</sub>	β <sub>2</sub>	low	mod	high	
14	RBR	bicubic	32	0.79	0.013	0.029	0.994	0.045	0.114	0.284	
15	RdNBR	bicubic	48	0.785	-0.858	3.219	0.852	2.647	8.476	21.02	
16	RBR	bilinear	16	0.781	0.021	0.026	1.016	0.05	0.114	0.278	
17	RdNBR	bicubic	32	0.776	-0.954	3.34	0.841	2.679	8.602	21.2	
18	dNDVI	bicubic	32	0.776	-0.058	0.073	0.65	0.02	0.106	0.257	
19	dNBR	bicubic	48	0.775	0.03	0.035	1.069	0.068	0.161	0.413	
20	RdNBR	bilinear	16	0.774	0.279	2.518	0.909	3.037	8.119	19.73	
21	dNDVI	bilinear	32	0.772	-0.053	0.07	0.656	0.022	0.105	0.252	
22	dNDVI	bicubic	48	0.772	-0.055	0.081	0.613	0.031	0.119	0.267	
23	dNBR	bilinear	32	0.77	0.029	0.036	1.048	0.069	0.163	0.41	
24	RdNBR2	bicubic	64	0.766	2.102	0.416	1.24	2.572	4.059	8.861	
25	dNBR	bicubic	32	0.764	0.028	0.036	1.057	0.068	0.163	0.417	
26	dNDVI	bilinear	48	0.762	-0.044	0.073	0.637	0.034	0.118	0.262	
27	RBR	bicubic	16	0.761	0.021	0.026	1.028	0.049	0.114	0.281	
28	dNBR	bilinear	16	0.76	0.033	0.036	1.048	0.073	0.167	0.417	
29	RdNBR2	bilinear	32	0.759	1.435	0.625	1.1	2.132	3.906	8.861	
30	RdNBR	bicubic	16	0.758	0.37	2.446	0.926	3.053	8.149	20	
31	RdNBR2	bicubic	32	0.754	1.426	0.601	1.125	2.098	3.876	8.975	
32	dNBR	bicubic	64	0.753	0.033	0.033	1.086	0.07	0.161	0.413	
33	dNBR	bilinear	64	0.751	0.035	0.033	1.08	0.071	0.161	0.406	
34	RdNBR2	bicubic	48	0.751	1.835	0.46	1.209	2.354	3.919	8.818	
35	dNBR	bilinear	48	0.748	0.035	0.033	1.076	0.071	0.161	0.405	

*SUPPLEMENTAL FIGURES AND TABLES*

---

Rank	Severity	Interp-								
		Time		k-fold						
		olation	window	R <sup>2</sup>	β <sub>0</sub>	β <sub>1</sub>	β <sub>2</sub>	low	mod	high
36	RdNDVI	bilinear	16	0.747	-0.983	2.503	0.678	1.695	4.856	10.52
37	dNDVI	bicubic	64	0.746	-0.055	0.082	0.609	0.032	0.12	0.266
38	dNDVI	bilinear	64	0.741	-0.046	0.075	0.627	0.034	0.118	0.261
39	RdNBR2	bilinear	48	0.737	1.802	0.497	1.174	2.361	3.956	8.766
40	RdNBR	bicubic	64	0.737	-1.448	3.651	0.819	2.515	8.717	21.61
41	RdNBR2	bilinear	64	0.735	2.027	0.451	1.204	2.536	4.06	8.801
42	dNBR	bicubic	16	0.729	0.032	0.036	1.058	0.072	0.168	0.423
43	dNBR2	bilinear	32	0.727	0.026	0.009	1.149	0.035	0.062	0.14
44	dNDVI	bicubic	16	0.726	-0.03	0.065	0.674	0.04	0.121	0.267
45	RdNDVI	bicubic	16	0.725	-1.248	2.681	0.665	1.618	4.908	10.72
46	dNBR2	bicubic	32	0.715	0.025	0.008	1.177	0.035	0.061	0.142
47	dNBR2	bilinear	64	0.714	0.036	0.006	1.283	0.043	0.064	0.137
48	dNDVI	bilinear	16	0.707	-0.023	0.06	0.689	0.042	0.12	0.261
49	dNBR2	bilinear	48	0.686	0.033	0.006	1.248	0.04	0.063	0.137
50	RdNBR2	bilinear	16	0.682	1.928	0.465	1.189	2.452	3.983	8.676
51	dNBR2	bilinear	16	0.662	0.03	0.009	1.138	0.04	0.066	0.143
52	RdNBR2	bicubic	16	0.654	1.871	0.467	1.198	2.398	3.96	8.792
53	dNBR2	bicubic	16	0.635	0.029	0.009	1.156	0.039	0.066	0.145
54	RdNBR	bilinear	48	0.63	-3.445	5.132	0.724	2.072	9.235	22.7
55	dNBR2	bicubic	48	0	0.033	0.006	1.284	0.04	0.062	0.138
56	dNBR2	bicubic	64	0	0.037	0.005	1.313	0.043	0.064	0.139

---

CHAPTER 2. SUPPLEMENTARY INFORMATION FOR CHAPTER 1

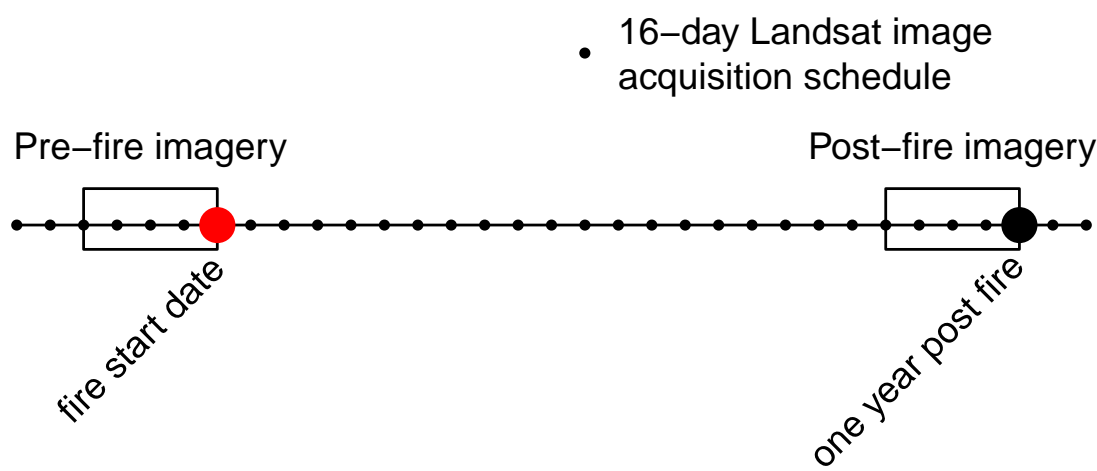


Figure 2.14: Schematic for how Landsat imagery was assembled in order to make comparisons between pre- and post-fire conditions. This schematic depicts a 64-day window of image collation prior to the fire which comprise the pre-fire image collection. A similar, 64-day window collection of imagery is assembled one year after the pre-fire image collection.

*SUPPLEMENTAL FIGURES AND TABLES*

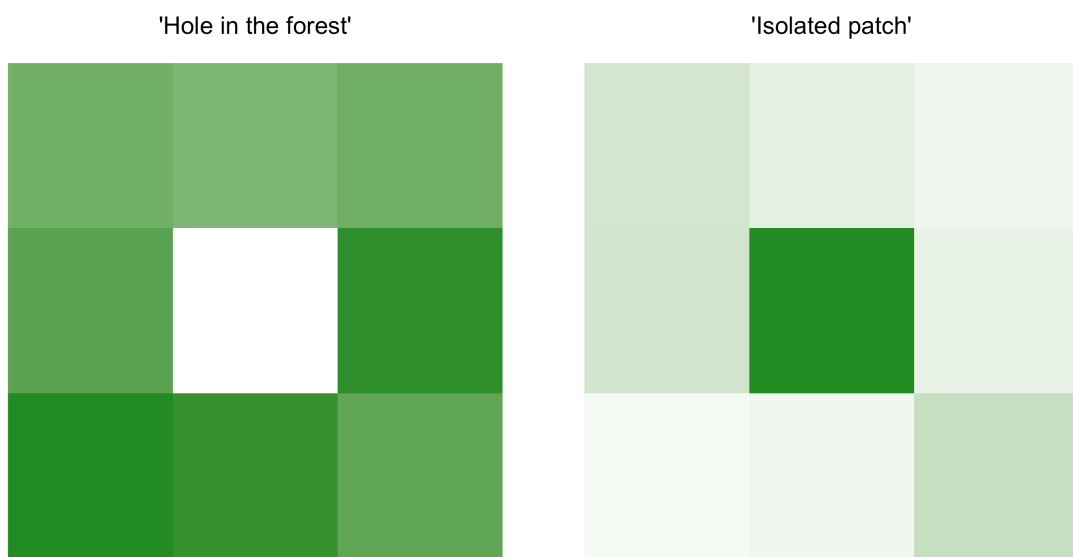


Figure 2.15: Conceptual diagram of ‘decoupling’ that sometimes occurs between the central pixel NDVI and the neighborhood mean NDVI. In each of these scenarios, our model results suggest that the probability that the central pixel burns at high severity is higher than expected given the additive effect of the covariates. The left panel depicts the “hole in the forest” decoupling, which occurs more frequently, and the right panel depicts the “isolated patch” decoupling.

# References

- Abatzoglou, J. T. 2013. Development of gridded surface meteorological data for ecological applications and modelling. *International Journal of Climatology* 33:121–131.
- Ackerly, D. D., S. R. Loarie, W. K. Cornwell, S. B. Weiss, H. Hamilton, R. Branciforte, and N. J. B. Kraft. 2010. The geography of climate change: Implications for conservation biogeography: Geography of climate change. *Diversity and Distributions* 16:476–487.
- Agashe, D. 2009. The Stabilizing Effect of Intraspecific Genetic Variation on Population Dynamics in Novel and Ancestral Habitats. *The American Naturalist* 174:255–267.
- Agee, J. K., and C. N. Skinner. 2005. Basic principles of forest fuel reduction treatments. *Forest Ecology and Management* 211:83–96.
- Agee, J., and C. ForestResourcesU. 1996. The influence of forest structure on fire behavior. 17th Forest Vegetation Management Conference:17.
- Anderegg, W. R. L., J. A. Hicke, R. A. Fisher, C. D. Allen, J. Aukema, B. Bentz, S. Hood, J. W. Lichstein, A. K. Macalady, N. McDowell, Y. Pan, K. Raffa, A. Sala, J. D. Shaw, N. L. Stephenson, C. Tague, and M. Zeppel. 2015. Tree mortality from drought,

## References

- insects, and their interactions in a changing climate. *New Phytologist* 208:674–683.
- Asner, G. P., P. G. Brodrick, C. B. Anderson, N. Vaughn, D. E. Knapp, and R. E. Martin. 2016. Progressive forest canopy water loss during the 20122015 California drought. *Proceedings of the National Academy of Sciences* 113:E249–E255.
- Baldwin, B. G., A. H. Thornhill, W. A. Freyman, D. D. Ackerly, M. M. Kling, N. Morueta-Holme, and B. D. Mishler. 2017. Species richness and endemism in the native flora of California. *American Journal of Botany* 104:487–501.
- Baskett, M. L., S. D. Gaines, and R. M. Nisbet. 2009. Symbiont diversity may help coral reefs survive moderate climate change. *Ecological Applications* 19:3–17.
- Bastarrika, A., E. Chuvieco, and M. P. Martín. 2011. Mapping burned areas from Landsat TM/ETM+ data with a two-phase algorithm: Balancing omission and commission errors. *Remote Sensing of Environment* 115:1003–1012.
- Beck, J., L. Ballesteros-Mejia, C. M. Buchmann, J. Dengler, S. A. Fritz, B. Gruber, C. Hof, F. Jansen, S. Knapp, H. Kreft, A.-K. Schneider, M. Winter, and C. F. Dormann. 2012. What's on the horizon for macroecology? *Ecography* 35:673–683.
- Bentz, B. J., J. Régnière, C. J. Fettig, E. M. Hansen, J. L. Hayes, J. A. Hicke, R. G. Kelsey, J. F. Negrón, and S. J. Seybold. 2010. Climate Change and Bark Beetles of the Western United States and Canada: Direct and Indirect Effects. *BioScience* 60:602–613.
- Berryman, A. A. 1982. Population dynamics of bark beetles. Pages 264–314 in *Bark Beetles in North American Conifers: A System for the Study of Evolutionary Biology*.
- Boschetti, L., D. P. Roy, C. O. Justice, and M. L. Humber. 2015. MODISLandsat fusion

## References

- for large area 30m burned area mapping. *Remote Sensing of Environment* 161:27–42.
- Brooks, S. P., and A. Gelman. 1998. General Methods for Monitoring Convergence of Iterative Simulations. *Journal of Computational and Graphical Statistics* 7:434.
- Bürkner, P.-C. 2017. **Brms** : An *R* Package for Bayesian Multilevel Models Using *Stan*. *Journal of Statistical Software* 80.
- Cadotte, M., C. H. Albert, and S. C. Walker. 2013. The ecology of differences: Assessing community assembly with trait and evolutionary distances. *Ecology Letters* 16:1234–1244.
- Calkin, D. E., K. M. Gebert, J. G. Jones, and R. P. Neilson. 2005. Forest Service Large Fire Area Burned and Suppression Expenditure Trends, 19702002. *Journal of Forestry* 103:179–183.
- Cansler, C. A., and D. McKenzie. 2012. How Robust Are Burn Severity Indices When Applied in a New Region? Evaluation of Alternate Field-Based and Remote-Sensing Methods. *Remote Sensing* 4:456–483.
- Chesson, P. 2000. Mechanisms of Maintenance of Species Diversity. *Annual Review of Ecology and Systematics* 31:343–366.
- Chubaty, A. M., B. D. Roitberg, and C. Li. 2009. A dynamic host selection model for mountain pine beetle, *Dendroctonus ponderosae* Hopkins. *Ecological Modelling* 220:1241–1250.
- Clark, J. S., L. Iverson, C. W. Woodall, C. D. Allen, D. M. Bell, D. C. Bragg, A. W. D'Amato, F. W. Davis, M. H. Hersh, I. Ibanez, S. T. Jackson, S. Matthews, N. Pederson, M. Peters, M. W. Schwartz, K. M. Waring, and N. E. Zimmermann. 2016. The impacts of increasing drought on forest dynamics, structure, and biodiversity in

## References

- the United States. *Global Change Biology* 22:2329–2352.
- Clevers, J., and A. Gitelson. 2013. Remote estimation of crop and grass chlorophyll and nitrogen content using red-edge bands on Sentinel-2 and -3. *International Journal of Applied Earth Observation and Geoinformation* 23:344–351.
- Collins, B. M., J. M. Lydersen, D. L. Fry, K. Wilkin, T. Moody, and S. L. Stephens. 2016. Variability in vegetation and surface fuels across mixed-conifer-dominated landscapes with over 40 years of natural fire. *Forest Ecology and Management* 381:74–83.
- Coops, N. C., M. Johnson, M. A. Wulder, and J. C. White. 2006. Assessment of QuickBird high spatial resolution imagery to detect red attack damage due to mountain pine beetle infestation. *Remote Sensing of Environment* 103:67–80.
- Coppoletta, M., K. E. Merriam, and B. M. Collins. 2016. Post-fire vegetation and fuel development influences fire severity patterns in reburns. *Ecological Applications* 26:686–699.
- Crowther, T. W., H. B. Glick, K. R. Covey, C. Bettigole, D. S. Maynard, S. M. Thomas, J. R. Smith, G. Hintler, M. C. Duguid, G. Amatulli, M.-N. Tuanmu, W. Jetz, C. Salas, C. Stam, D. Piotto, R. Tavani, S. Green, G. Bruce, S. J. Williams, S. K. Wiser, M. O. Huber, G. M. Hengeveld, G.-J. Nabuurs, E. Tikhonova, P. Borchardt, C.-F. Li, L. W. Powrie, M. Fischer, A. Hemp, J. Homeier, P. Cho, A. C. Vibrans, P. M. Umunay, S. L. Piao, C. W. Rowe, M. S. Ashton, P. R. Crane, and M. A. Bradford. 2015. Mapping tree density at a global scale. *Nature* 525:201–205.
- De Santis, A., G. P. Asner, P. J. Vaughan, and D. E. Knapp. 2010. Mapping burn severity and burning efficiency in California using simulation models and Landsat

## References

- imagery. *Remote Sensing of Environment* 114:1535–1545.
- Dillon, G. K., Z. A. Holden, P. Morgan, M. A. Crimmins, E. K. Heyerdahl, and C. H. Luce. 2011. Both topography and climate affected forest and woodland burn severity in two regions of the western US, 1984 to 2006. *Ecosphere* 2:art130.
- DJI. 2015a. Zenmuse X3 - Creativity Unleashed. <https://www.dji.com/zenmuse-x3/info>.
- DJI. 2015b. DJI - The World Leader in Camera Drones/Quadcopters for Aerial Photography. <https://www.dji.com/matrice100/info>.
- DronesMadeEasy. 2018. Map Pilot for DJI on iOS. <https://itunes.apple.com/us/app/map-pilot-for-dji/id1014765000?mt=8>.
- Edwards, A. C., J. Russell-Smith, and S. W. Maier. 2018. A comparison and validation of satellite-derived fire severity mapping techniques in fire prone north Australian savannas: Extreme fires and tree stem mortality. *Remote Sensing of Environment* 206:287–299.
- Eidenshink, J., B. Schwind, K. Brewer, Z.-L. Zhu, B. Quayle, and S. Howard. 2007. A Project for Monitoring Trends in Burn Severity. *Fire Ecology* 3:3–21.
- Evenden, M. L., C. M. Whitehouse, and J. Sykes. 2014. Factors Influencing Flight Capacity of the Mountain Pine Beetle (Coleoptera: Curculionidae: Scolytinae). *Environmental Entomology* 43:187–196.
- Eysn, L., M. Hollaus, E. Lindberg, F. Berger, J.-M. Monnet, M. Dalponte, M. Kobal, M. Pellegrini, E. Lingua, D. Mongus, and N. Pfeifer. 2015. A Benchmark of Lidar-Based Single Tree Detection Methods Using Heterogeneous Forest Data from the Alpine

## References

- Space. Forests 6:1721–1747.
- Farr, T. G., P. A. Rosen, E. Caro, R. Crippen, R. Duren, S. Hensley, M. Kobrick, M. Paller, E. Rodriguez, L. Roth, D. Seal, S. Shaffer, J. Shimada, J. Umland, M. Werner, M. Oskin, D. Burbank, and D. Alsdorf. 2007. The Shuttle Radar Topography Mission. *Reviews of Geophysics* 45.
- Fernández-García, V., M. Santamaría, A. Fernández-Manso, C. Quintano, E. Marcos, and L. Calvo. 2018. Burn severity metrics in fire-prone pine ecosystems along a climatic gradient using Landsat imagery. *Remote Sensing of Environment* 206:205–217.
- Fettig, C. J. 2012. Chapter 2: Forest health and bark beetles. *in* Managing Sierra Nevada Forests. PSW-GTR-237. USDA Forest Service.
- Fettig, C. J., K. D. Klepzig, R. F. Billings, A. S. Munson, T. E. Nebeker, J. F. Negrón, and J. T. Nowak. 2007. The effectiveness of vegetation management practices for prevention and control of bark beetle infestations in coniferous forests of the western and southern United States. *Forest Ecology and Management* 238:24–53.
- Fettig, C. J., L. A. Mortenson, B. M. Bulaon, and P. B. Foulk. 2019. Tree mortality following drought in the central and southern Sierra Nevada, California, U.S. *Forest Ecology and Management* 432:164–178.
- Flint, L. E., A. L. Flint, J. H. Thorne, and R. Boynton. 2013. Fine-scale hydrologic modeling for regional landscape applications: The California Basin Characterization Model development and performance. *Ecological Processes* 2:25.
- Floyd, M. L., M. Clifford, N. S. Cobb, D. Hanna, R. Delph, P. Ford, and D. Turner. 2009. Relationship of stand characteristics to drought-induced mortality in three

## References

- Southwestern piñonJuniper woodlands. *Ecological Applications* 19:1223–1230.
- Foga, S., P. L. Scaramuzza, S. Guo, Z. Zhu, R. D. Dilley, T. Beckmann, G. L. Schmidt, J. L. Dwyer, M. Joseph Hughes, and B. Laue. 2017. Cloud detection algorithm comparison and validation for operational Landsat data products. *Remote Sensing of Environment* 194:379–390.
- Franklin, J., T. Logan, C. Woodcock, and A. Strahler. 1986. Coniferous Forest Classification and Inventory Using Landsat and Digital Terrain Data. *IEEE Transactions on Geoscience and Remote Sensing* GE-24:139–149.
- Frey, J., K. Kovach, S. Stemmler, and B. Koch. 2018. UAV Photogrammetry of Forests as a Vulnerable Process. A Sensitivity Analysis for a Structure from Motion RGB-Image Pipeline. *Remote Sensing* 10:912.
- Gabry, J., D. Simpson, A. Vehtari, M. Betancourt, and A. Gelman. 2019. Visualization in Bayesian workflow. *Journal of the Royal Statistical Society: Series A (Statistics in Society)* 182:389–402.
- Gao, B.-c. 1996. NDWIA normalized difference water index for remote sensing of vegetation liquid water from space. *Remote Sensing of Environment* 58:257–266.
- García, M. L., and V. Caselles. 1991. Mapping burns and natural reforestation using thematic Mapper data. *Geocarto International* 6:31–37.
- Gazol, A., and J. J. Camarero. 2016. Functional diversity enhances silver fir growth resilience to an extreme drought. *Journal of Ecology* 104:1063–1075.
- Gelman, A., B. Goodrich, J. Gabry, and A. Vehtari. 2018. R-squared for Bayesian regression models. *The American Statistician*:1–6.
- Gitelson, A., and M. N. Merzlyak. 1994. Spectral Reflectance Changes Associated with

## References

- Autumn Senescence of *Aesculus hippocastanum* L. and *Acer platanoides* L. Leaves. Spectral Features and Relation to Chlorophyll Estimation. *Journal of Plant Physiology* 143:286–292.
- Goodwin, N. R., and L. J. Collett. 2014. Development of an automated method for mapping fire history captured in Landsat TM and ETM+ time series across Queensland, Australia. *Remote Sensing of Environment* 148:206–221.
- Gorelick, N., M. Hancher, M. Dixon, S. Ilyushchenko, D. Thau, and R. Moore. 2017. Google Earth Engine: Planetary-scale geospatial analysis for everyone. *Remote Sensing of Environment* 202:18–27.
- Graf, M., M. Reid, B. Aukema, and B. Lindgren. 2012. Association of tree diameter with body size and lipid content of mountain pine beetles. *The Canadian Entomologist* 144:467–477.
- Graham, R. T., S. McCaffrey, and T. B. Jain. 2004. Science basis for changing forest structure to modify wildfire behavior and severity. U.S. Department of Agriculture, Forest Service, Rocky Mountain Research Station, Ft. Collins, CO.
- Gray, P. C., A. B. Fleishman, D. J. Klein, M. W. McKown, V. S. Bézy, K. J. Lohmann, and D. W. Johnston. 2019. A convolutional neural network for detecting sea turtles in drone imagery. *Methods in Ecology and Evolution* 10:345–355.
- Griffin, D., and K. J. Anchukaitis. 2014. How unusual is the 20122014 California drought? *Geophysical Research Letters* 41:9017–9023.
- Hansen, M. C., P. V. Potapov, R. Moore, M. Hancher, S. A. Turubanova, A. Tyukavina, D. Thau, S. V. Stehman, S. J. Goetz, T. R. Loveland, A. Kommareddy, A. Egorov, L. Chini, C. O. Justice, and J. R. G. Townshend. 2013. High-Resolution Global Maps

## References

- of 21st-Century Forest Cover Change. *Science* 342:850–853.
- Haralick, R. M., K. Shanmugam, and I. Dinstein. 1973. Textural Features for Image Classification. *IEEE Transactions on Systems, Man, and Cybernetics SMC-3*:610–621.
- Hawbaker, T. J., M. K. Vanderhoof, Y.-J. Beal, J. D. Takacs, G. L. Schmidt, J. T. Falgout, B. Williams, N. M. Fairaux, M. K. Caldwell, J. J. Picotte, S. M. Howard, S. Stitt, and J. L. Dwyer. 2017. Mapping burned areas using dense time-series of Landsat data. *Remote Sensing of Environment* 198:504–522.
- Hayes, C. J., C. J. Fettig, and L. D. Merrill. 2009. Evaluation of Multiple Funnel Traps and Stand Characteristics for Estimating Western Pine Beetle-Caused Tree Mortality. *Journal of Economic Entomology* 102:2170–2182.
- Heffernan, J. B., P. A. Soranno, M. J. Angilletta, L. B. Buckley, D. S. Gruner, T. H. Keitt, J. R. Kellner, J. S. Kominoski, A. V. Rocha, J. Xiao, T. K. Harms, S. J. Goring, L. E. Koenig, W. H. McDowell, H. Powell, A. D. Richardson, C. A. Stow, R. Vargas, and K. C. Weathers. 2014. Macrosystems ecology: Understanding ecological patterns and processes at continental scales. *Frontiers in Ecology and the Environment* 12:5–14.
- Henry, L., and H. Wickham. 2019. Purrr: Functional Programming Tools.
- Hijmans, R. J., J. van Etten, M. Sumner, J. Cheng, A. Bevan, R. Bivand, L. Busetto, M. Canty, D. Forrest, A. Ghosh, D. Golicher, J. Gray, J. A. Greenberg, P. Hiemstra, I. for M. A. Geosciences, C. Karney, M. Mattiuzzi, S. Mosher, J. Nowosad, E. Pebesma, O. P. Lamigueiro, E. B. Racine, B. Rowlingson, A. Shortridge, B. Venables, and R. Wueest. 2019. Raster: Geographic Data Analysis and Modeling.
- Hoffman, M. D., and A. Gelman. 2014. The No-U-Turn Sampler: Adaptively Setting

## References

- Path Lengths in Hamiltonian Monte Carlo. *Journal of Machine Learning Research* 15:31.
- Holden, Z. A., P. Morgan, and J. S. Evans. 2009. A predictive model of burn severity based on 20-year satellite-inferred burn severity data in a large southwestern US wilderness area. *Forest Ecology and Management* 258:2399–2406.
- Holling, C. S. 1973. Resilience and Stability of Ecological Systems. *Annual Review of Ecology and Systematics*:1–23.
- Huang, Q., A. Swatantran, R. Dubayah, and S. J. Goetz. 2014. The Influence of Vegetation Height Heterogeneity on Forest and Woodland Bird Species Richness across the United States. *PLoS ONE* 9:e103236.
- Huesca, M., M. García, K. L. Roth, A. Casas, and S. L. Ustin. 2016. Canopy structural attributes derived from AVIRIS imaging spectroscopy data in a mixed broadleaf/conifer forest. *Remote Sensing of Environment* 182:208–226.
- Hunziker, P. 2017. Velox: Fast Raster Manipulation and Extraction.
- Jakubowski, M. K., W. Li, Q. Guo, and M. Kelly. 2013. Delineating Individual Trees from Lidar Data: A Comparison of Vector- and Raster-based Segmentation Approaches. *Remote Sensing* 5:4163–4186.
- JepsonFloraProject, editor. 2016. Jepson eFlora.
- Kane, V. R., M. P. North, J. A. Lutz, D. J. Churchill, S. L. Roberts, D. F. Smith, R. J. McGaughey, J. T. Kane, and M. L. Brooks. 2014. Assessing fire effects on forest spatial structure using a fusion of Landsat and airborne LiDAR data in Yosemite National Park. *Remote Sensing of Environment* 151:89–101.
- Keith, D. A., J. P. Rodríguez, K. M. Rodríguez-Clark, E. Nicholson, K. Aapala, A.

## References

- Alonso, M. Asmussen, S. Bachman, A. Bassett, E. G. Barrow, J. S. Benson, M. J. Bishop, R. Bonifacio, T. M. Brooks, M. A. Burgman, P. Comer, F. A. Comín, F. Essl, D. Faber-Langendoen, P. G. Fairweather, R. J. Holdaway, M. Jennings, R. T. Kingsford, R. E. Lester, R. M. Nally, M. A. McCarthy, J. Moat, M. A. Oliveira-Miranda, P. Pisanu, B. Poulin, T. J. Regan, U. Riecken, M. D. Spalding, and S. Zambrano-Martínez. 2013. Scientific Foundations for an IUCN Red List of Ecosystems. *PLoS ONE* 8:e62111.
- Key, C. H., and N. C. Benson. 2006. Landscape Assessment (LA):55.
- Kéfi, S., V. Guttal, W. A. Brock, S. R. Carpenter, A. M. Ellison, V. N. Livina, D. A. Seekell, M. Scheffer, E. H. van Nes, and V. Dakos. 2014. Early Warning Signals of Ecological Transitions: Methods for Spatial Patterns. *PLoS ONE* 9:e92097.
- Kolb, T. E., C. J. Fettig, M. P. Ayres, B. J. Bentz, J. A. Hicke, R. Mathiasen, J. E. Stewart, and A. S. Weed. 2016. Observed and anticipated impacts of drought on forest insects and diseases in the United States. *Forest Ecology and Management* 380:321–334.
- Kolden, C. A., A. M. S. Smith, and J. T. Abatzoglou. 2015. Limitations and utilisation of Monitoring Trends in Burn Severity products for assessing wildfire severity in the USA. *International Journal of Wildland Fire* 24:1023.
- Kotliar, N. B., and J. A. Wiens. 1990. Multiple Scales of Patchiness and Patch Structure: A Hierarchical Framework for the Study of Heterogeneity. *Oikos* 59:253.
- Kuhn, M. 2008. Building Predictive Models in R Using the caret Package. *Journal of Statistical Software* 28:1–26.
- Larson, A. J., and D. Churchill. 2012. Tree spatial patterns in fire-frequent forests of

## References

- western North America, including mechanisms of pattern formation and implications for designing fuel reduction and restoration treatments. *Forest Ecology and Management* 267:74–92.
- Lenoir, J., B. J. Graae, P. A. Aarrestad, I. G. Alsos, W. S. Armbruster, G. Austrheim, C. Bergendorff, H. J. B. Birks, K. A. Bråthen, J. Brunet, H. H. Bruun, C. J. Dahlberg, G. Decocq, M. Diekmann, M. Dynesius, R. Ejrnaes, J.-A. Grytnes, K. Hylander, K. Klannderud, M. Luoto, A. Milbau, M. Moora, B. Nygaard, A. Odland, V. T. Ravolainen, S. Reinhardt, S. M. Sandvik, F. H. Schei, J. D. M. Speed, L. U. Tveraabak, V. Vandvik, L. G. Velle, R. Virtanen, M. Zobel, and J.-C. Svenning. 2013. Local temperatures inferred from plant communities suggest strong spatial buffering of climate warming across Northern Europe. *Global Change Biology* 19:1470–1481.
- Li, W., Q. Guo, M. K. Jakubowski, and M. Kelly. 2012. A New Method for Segmenting Individual Trees from the Lidar Point Cloud. *Photogrammetric Engineering & Remote Sensing* 78:75–84.
- Logan, J. A., P. White, B. J. Bentz, and J. A. Powell. 1998. Model Analysis of Spatial Patterns in Mountain Pine Beetle Outbreaks. *Theoretical Population Biology* 53:236–255.
- Lydersen, J. M., B. M. Collins, E. E. Knapp, G. B. Roller, and S. Stephens. 2015. Relating fuel loads to overstorey structure and composition in a fire-excluded Sierra Nevada mixed conifer forest. *International Journal of Wildland Fire* 24:484.
- Lydersen, J. M., M. P. North, and B. M. Collins. 2014. Severity of an uncharacteristically large wildfire, the Rim Fire, in forests with relatively restored frequent fire regimes. *Forest Ecology and Management* 328:326–334.
- Malone, S., P. Fornwalt, M. Battaglia, M. Chambers, J. Iniguez, and C. Sieg. 2018.

## References

- Mixed-Severity Fire Fosters Heterogeneous Spatial Patterns of Conifer Regeneration in a Dry Conifer Forest. *Forests* 9:45.
- Masek, J., E. Vermote, N. Saleous, R. Wolfe, F. Hall, K. Huemmrich, F. Gao, J. Kutler, and T.-K. Lim. 2006. A Landsat Surface Reflectance Dataset for North America, 1990–2000. *IEEE Geoscience and Remote Sensing Letters* 3:68–72.
- McCune, B. 2007. Improved estimates of incident radiation and heat load using non-parametric regression against topographic variables. *Journal of Vegetation Science* 18:751–754.
- McCune, B., and D. Keon. 2002. Equations for potential annual direct incident radiation and heat load. *Journal of Vegetation Science* 13:603–606.
- Meyer, F., and S. Beucher. 1990. Morphological segmentation. *Journal of Visual Communication and Image Representation* 1:21–46.
- Micasense. 2015. MicaSense. <https://support.micasense.com/hc/en-us/articles/215261448-RedEdge-User-Manual-PDF-Download->.
- Millar, C. I., and N. L. Stephenson. 2015. Temperate forest health in an era of emerging megadisturbance. *Science* 349:823–826.
- Millar, C. I., N. L. Stephenson, and S. L. Stephens. 2007. CLIMATE CHANGE AND FORESTS OF THE FUTURE: MANAGING IN THE FACE OF UNCERTAINTY. *Ecological Applications* 17:2145–2151.
- Millar, C. I., R. D. Westfall, D. L. Delany, M. J. Bokach, A. L. Flint, and L. E. Flint. 2012. Forest mortality in high-elevation whitebark pine (*Pinus Albicaulis*) forests of eastern California, USA; influence of environmental context, bark beetles, climatic

## References

- water deficit, and warming. Canadian Journal of Forest Research 42:749–765.
- Miller, J. D., and H. Safford. 2012. TRENDS IN WILDFIRE SEVERITY: 1984 TO2010 IN THE SIERRA NEVADA, MODOC PLATEAU, AND SOUTHERN CASCADES, CALIFORNIA, USA. Fire Ecology 8:41–57.
- Miller, J. D., and H. D. Safford. 2017. Corroborating Evidence of a Pre-Euro-American Low- to Moderate-Severity Fire Regime in Yellow PineMixed Conifer Forests of the Sierra Nevada, California, USA. Fire Ecology 13:58–90.
- Miller, J. D., and A. E. Thode. 2007. Quantifying burn severity in a heterogeneous landscape with a relative version of the delta Normalized Burn Ratio (dNBR). Remote Sensing of Environment 109:66–80.
- Miller, J. D., E. E. Knapp, C. H. Key, C. N. Skinner, C. J. Isbell, R. M. Creasy, and J. W. Sherlock. 2009. Calibration and validation of the relative differenced Normalized Burn Ratio (RdNBR) to three measures of fire severity in the Sierra Nevada and Klamath Mountains, California, USA. Remote Sensing of Environment 113:645–656.
- Miller, J. D., C. N. Skinner, H. D. Safford, E. E. Knapp, and C. M. Ramirez. 2012. Trends and causes of severity, size, and number of fires in northwestern California, USA. Ecological Applications 22:184–203.
- Miller, J. M., and F. P. Keen. 1960. Biology and control of the western pine beetle: A summary of the first fifty years of research. US Department of Agriculture.
- Moeck, H. A., D. L. Wood, and K. Q. Lindahl. 1981. Host selection behavior of bark beetles (Coleoptera: Scolytidae) attackingPinus ponderosa, with special emphasis on the western pine beetle,Dendroctonus brevicomis. Journal of Chemical Ecology 7:49–

## References

- 83.
- Moritz, M. A., M. E. Morais, L. A. Summerell, J. M. Carlson, and J. Doyle. 2005. Wildfires, complexity, and highly optimized tolerance. *Proceedings of the National Academy of Sciences* 102:17912–17917.
- Morris, J. L., S. Cottrell, C. J. Fettig, W. D. Hansen, R. L. Sherriff, V. A. Carter, J. L. Clear, J. Clement, R. J. DeRose, J. A. Hicke, P. E. Higuera, K. M. Mattor, A. W. R. Seddon, H. T. Seppä, J. D. Stednick, and S. J. Seybold. 2017. Managing bark beetle impacts on ecosystems and society: Priority questions to motivate future research. *Journal of Applied Ecology* 54:750–760.
- North, M. P., S. L. Stephens, B. M. Collins, J. K. Agee, G. Aplet, J. F. Franklin, and P. Z. Fule. 2015. Reform forest fire management. *Science* 349:1280–1281.
- North, M., P. Stine, K. O'Hara, W. Zielinski, and S. Stephens. 2009. An ecosystem management strategy for Sierran mixed-conifer forests. U.S. Department of Agriculture, Forest Service, Pacific Southwest Research Station, Albany, CA.
- Parks, S. A., L. M. Holsinger, M. H. Panunto, W. M. Jolly, S. Z. Dobrowski, and G. K. Dillon. 2018. High-severity fire: Evaluating its key drivers and mapping its probability across western US forests. *Environmental Research Letters* 13:044037.
- Parks, S., G. Dillon, and C. Miller. 2014. A New Metric for Quantifying Burn Severity: The Relativized Burn Ratio. *Remote Sensing* 6:1827–1844.
- Pau, G., F. Fuchs, O. Sklyar, M. Boutros, and W. Huber. 2010. EBImage R package for image processing with applications to cellular phenotypes. *Bioinformatics* 26:979–981.
- Pebesma, E., R. Bivand, E. Racine, M. Sumner, I. Cook, T. Keitt, R. Lovelace, H.

## References

- Wickham, J. Ooms, K. Müller, and T. L. Pedersen. 2019. Sf: Simple Features for R.
- Peters, D. P. C., R. A. Pielke, B. T. Bestelmeyer, C. D. Allen, S. Munson-McGee, and K. M. Havstad. 2004. Cross-scale interactions, nonlinearities, and forecasting catastrophic events. *Proceedings of the National Academy of Sciences* 101:15130–15135.
- Pile, L. S., M. D. Meyer, R. Rojas, O. Roe, and M. T. Smith. 2019. Drought Impacts and Compounding Mortality on Forest Trees in the Southern Sierra Nevada. *Forests* 10:237.
- Plowright, A. 2018. ForestTools: Analyzing Remotely Sensed Forest Data.
- Popescu, S. C., and R. H. Wynne. 2004. Seeing the Trees in the Forest: Using Lidar and Multispectral Data Fusion with Local Filtering and Variable Window Size for Estimating Tree Height. *PHOTOGRAMMETRIC ENGINEERING*:16.
- Preisler, H. K., N. E. Grulke, Z. Heath, and S. L. Smith. 2017. Analysis and out-year forecast of beetle, borer, and drought-induced tree mortality in California. *Forest Ecology and Management*. 399: 166–178 399:166–178.
- Prichard, S. J., and M. C. Kennedy. 2014. Fuel treatments and landform modify landscape patterns of burn severity in an extreme fire event. *Ecological Applications* 24:571–590.
- Questad, E. J., and B. L. Foster. 2008. Coexistence through spatio-temporal heterogeneity and species sorting in grassland plant communities. *Ecology Letters* 11:717–726.
- R Core Team. 2018. R: A Language and Environment for Statistical Computing. R Foundation for Statistical Computing, Vienna, Austria.
- Raffa, K. F., and A. A. Berryman. 1983. The Role of Host Plant Resistance in the Col-

## References

- onization Behavior and Ecology of Bark Beetles (Coleoptera: Scolytidae). Ecological Monographs 53:27–49.
- Raffa, K. F., and A. A. Berryman. 1987. Interacting Selective Pressures in Conifer-Bark Beetle Systems: A Basis for Reciprocal Adaptations? *The American Naturalist* 129:234–262.
- Raffa, K. F., B. H. Aukema, B. J. Bentz, A. L. Carroll, J. A. Hicke, M. G. Turner, and W. H. Romme. 2008. Cross-scale Drivers of Natural Disturbances Prone to Anthropogenic Amplification: The Dynamics of Bark Beetle Eruptions. *BioScience* 58:501–517.
- Raffa, K. F., J.-C. Grégoire, and B. Staffan Lindgren. 2015. Natural History and Ecology of Bark Beetles. Pages 1–40 in Bark Beetles. Elsevier.
- Reilly, M. J., C. J. Dunn, G. W. Meigs, T. A. Spies, R. E. Kennedy, J. D. Bailey, and K. Briggs. 2017. Contemporary patterns of fire extent and severity in forests of the Pacific Northwest, USA (1985–2010). *Ecosphere* 8:e01695.
- Reusch, T. B. H., A. Ehlers, A. Hammerli, and B. Worm. 2005. Ecosystem recovery after climatic extremes enhanced by genotypic diversity. *Proceedings of the National Academy of Sciences* 102:2826–2831.
- Rouse, W., R. H. Haas, W. Deering, and J. A. Schell. 1973. MONITORING THE VERNAL ADVANCEMENT AND RETROGRADATION (GREEN WAVE EFFECT) OF NATURAL VEGETATION. Type II Report, Goddard Space Flight Center, Greenbelt, MD, USA.
- Roussel, J.-R. 2019. lidRplugins: Extra functions and algorithms for lidR package.
- Roussel, J.-R., D. A. (the documentation), F. D. B. (bugs and improved catalog

## References

- features), and A. S. M. (. lassnags). 2019. lidR: Airborne LiDAR Data Manipulation and Visualization for Forestry Applications.
- Safford, H. D., and J. T. Stevens. 2017. Natural Range of Variation for Yellow Pine and Mixed-Conifer Forests in the Sierra Nevada, Southern Cascades, and Modoc and Inyo National Forests, California, USA. Page 241.
- Safford, H., J. Stevens, K. Merriam, M. Meyer, and A. Latimer. 2012. Fuel treatment effectiveness in California yellow pine and mixed conifer forests. *Forest Ecology and Management* 274:17–28.
- Scholl, A. E., and A. H. Taylor. 2010. Fire regimes, forest change, and self-organization in an old-growth mixed-conifer forest, Yosemite National Park, USA. *Ecological Applications* 20:362–380.
- Seidl, R., J. Müller, T. Hothorn, C. Bässler, M. Heurich, and M. Kautz. 2016. Small beetle, large-scale drivers: How regional and landscape factors affect outbreaks of the European spruce bark beetle. *The Journal of applied ecology* 53:530–540.
- Shiklomanov, A. N., B. A. Bradley, K. M. Dahlin, A. M. Fox, C. M. Gough, F. M. Hoffman, E. M. Middleton, S. P. Serbin, L. Smallman, and W. K. Smith. 2019. Enhancing global change experiments through integration of remote-sensing techniques. *Frontiers in Ecology and the Environment* 0.
- Shin, P., T. Sankey, M. Moore, and A. Thode. 2018. Evaluating Unmanned Aerial Vehicle Images for Estimating Forest Canopy Fuels in a Ponderosa Pine Stand. *Remote Sensing* 10:1266.
- Sikkink, P. G., G. K. Dillon, R. E. Keane, P. Morgan, E. C. Karau, Z. A. Holden, and R. P. Silverstein. 2013. Composite Burn Index (CBI) data and field photos collected

## References

- for the FIRESEV project, western United States.
- Steel, Z. L., M. J. Koontz, and H. D. Safford. 2018. The changing landscape of wildfire: Burn pattern trends and implications for California's yellow pine and mixed conifer forests. *Landscape Ecology* 33:1159–1176.
- Stein, A., K. Gerstner, and H. Kreft. 2014. Environmental heterogeneity as a universal driver of species richness across taxa, biomes and spatial scales. *Ecology Letters* 17:866–880.
- Stephens, S. L., D. L. Fry, and E. Franco-Vizcaíno. 2008. Wildfire and Spatial Patterns in Forests in Northwestern Mexico: The United States Wishes It Had Similar Fire Problems. *Ecology and Society* 13.
- Stephens, S. L., J. D. McIver, R. E. J. Boerner, C. J. Fettig, J. B. Fontaine, B. R. Hartsough, P. L. Kennedy, and D. W. Schwilk. 2012. The Effects of Forest Fuel-Reduction Treatments in the United States. *BioScience* 62:549–560.
- Stephens, S. L., J. J. Moghaddas, C. Edminster, C. E. Fiedler, S. Haase, M. Harrington, J. E. Keeley, E. E. Knapp, J. D. McIver, K. Metlen, C. N. Skinner, and A. Youngblood. 2009. Fire treatment effects on vegetation structure, fuels, and potential fire severity in western U.S. forests. *Ecological Applications* 19:305–320.
- Stephenson, N. 1998. Actual evapotranspiration and deficit: Biologically meaningful correlates of vegetation distribution across spatial scales. *Journal of Biogeography* 25:855–870.
- Stephenson, N. L., A. J. Das, N. J. Ampersee, and B. M. Bulaon. 2019. Which trees die during drought? The key role of insect host-tree selection. *Journal of Ecology*:75.
- Stevens, J. T., B. M. Collins, J. D. Miller, M. P. North, and S. L. Stephens. 2017.

## References

- Changing spatial patterns of stand-replacing fire in California conifer forests. *Forest Ecology and Management* 406:28–36.
- Sugihara, N. G., J. W. V. Wagtendonk, J. Fites-Kaufman, K. E. Shaffer, and A. E. Thode. 2006. *Fire in California's ecosystems*. University of California Press.
- Thistle, H. W., H. Peterson, G. Allwine, B. Lamb, T. Strand, E. H. Holsten, and P. J. Shea. 2004. Surrogate Pheromone Plumes in Three Forest Trunk Spaces: Composite Statistics and Case Studies. *Forest Science* 50.
- Tilman, D. 1994. Competition and Biodiversity in Spatially Structured Habitats. *Ecology* 75:2–16.
- Trumbore, S., P. Brando, and H. Hartmann. 2015. Forest health and global change. *Science* 349:814–818.
- Tuanmu, M.-N., and W. Jetz. 2015. A global, remote sensing-based characterization of terrestrial habitat heterogeneity for biodiversity and ecosystem modelling: Global habitat heterogeneity. *Global Ecology and Biogeography* 24:1329–1339.
- USDAFS. 2019, February 11. Press Release: Survey finds 18 million trees died in California in 2018. [https://www.fs.usda.gov/Internet/FSE\\_DOCUMENTS/FSEPRD609321.pdf](https://www.fs.usda.gov/Internet/FSE_DOCUMENTS/FSEPRD609321.pdf).
- USGS. 2017a. Landsat 8 Surface Reflectance Code (LASRC) Product Guide:40.
- USGS. 2017b. Landsat 4-7 Surface Reflectance (LEDAPS) Product Guide:41.
- Vega, C., A. Hamrouni, S. El Mokhtari, J. Morel, J. Bock, J. P. Renaud, M. Bouvier, and S. Durrieu. 2014. PTrees: A point-based approach to forest tree extraction from lidar data. *International Journal of Applied Earth Observation and Geoinformation*

## References

- 33:98–108.
- Vehtari, A., A. Gelman, and J. Gabry. 2017. Practical Bayesian model evaluation using leave-one-out cross-validation and WAIC. *Statistics and Computing* 27:1413–1432.
- Veraverbeke, S., and S. J. Hook. 2013. Evaluating spectral indices and spectral mixture analysis for assessing fire severity, combustion completeness and carbon emissions. *International Journal of Wildland Fire* 22:707.
- Vermote, E., C. Justice, M. Claverie, and B. Franch. 2016. Preliminary analysis of the performance of the Landsat 8/OLI land surface reflectance product. *Remote Sensing of Environment* 185:46–56.
- Virah-Sawmy, M., L. Gillson, and K. J. Willis. 2009. How does spatial heterogeneity influence resilience to climatic changes? Ecological dynamics in southeast Madagascar. *Ecological Monographs* 79:557–574.
- Wagner, C. E. V. 1977. Conditions for the start and spread of crown fire. *Canadian Journal of Forest Research* 7:23–34.
- Wagtendonk, J. W. V. 2006. Fire as a Physical Process. University of California Press.
- Walker, B., C. S. Holling, S. R. Carpenter, and A. P. Kinzig. 2004. Resilience, Adaptability and Transformability in Social-ecological Systems. *Ecology and Society* 9.
- Walker, R. B., J. D. Coop, S. A. Parks, and L. Trader. 2018. Fire regimes approaching historic norms reduce wildfire-facilitated conversion from forest to non-forest. *Eco-sphere* 9:e02182.
- White, P., and J. Powell. 1997. Phase transition from environmental to dynamic deter-

- minism in mountain pine beetle attack. *Bulletin of Mathematical Biology* 59:609–643.
- Wickham, H. 2019. Modelr: Modelling Functions that Work with the Pipe.
- Williams, A. P., C. D. Allen, A. K. Macalady, D. Griffin, C. A. Woodhouse, D. M. Meko, T. W. Swetnam, S. A. Rauscher, R. Seager, H. D. Grissino-Mayer, J. S. Dean, E. R. Cook, C. Gangodagamage, M. Cai, and N. G. McDowell. 2013. Temperature as a potent driver of regional forest drought stress and tree mortality. *Nature Climate Change* 3:292–297.
- Wood, E. M., A. M. Pidgeon, V. C. Radeloff, and N. S. Keuler. 2012. Image texture as a remotely sensed measure of vegetation structure. *Remote Sensing of Environment* 121:516–526.
- Young, D. J. N., J. T. Stevens, J. M. Earles, J. Moore, A. Ellis, A. L. Jirka, and A. M. Latimer. 2017. Long-term climate and competition explain forest mortality patterns under extreme drought. *Ecology Letters* 20:78–86.
- Zhang, W., J. Qi, P. Wan, H. Wang, D. Xie, X. Wang, and G. Yan. 2016. An Easy-to-Use Airborne LiDAR Data Filtering Method Based on Cloth Simulation. *Remote Sensing* 8:501.
- Zhu, Z., C. Key, D. Ohlen, and N. Benson. 2006. Evaluate Sensitivities of Burn-Severity Mapping Algorithms for Different Ecosystems and Fire Histories in the United States. Page 35. Final Report to the Joint Fire Science Program.